Direct numerical simulation of interfacial mass transfer and pollutant transport in turbulent open channel flow

Zur Erlangung des akademischen Grades eines

Doktor-Ingenieurs

von der KIT-Fakultät für
Bauingenieur-, Geo- und Umweltwissenschaften
des Karlsruher Instituts für Technologie (KIT)

genehmigte

Dissertation

von

M.Sc. Michele Pinelli

geb. in Brescia

Abstract

The present thesis focuses on the study of interfacial mass transfer across the air-water interface of a turbulent open channel flow through direct numerical simulation. Despite its high scientific relevance, the detailed mechanisms of this phenomenon are far from being completely understood today. Atmospheric gases usually have very low diffusivities in water and tend to create thin, elongated structures in which very steep gradients can be found. The necessity of cutting edge technologies required to analyze this phenomenon experimentally and the extremely high computational costs required by solving the fine grid resolutions needed in direct numerical simulations hindered the development of a unified model for gas transfer.

This thesis presents the results of direct numerical simulations (DNSs) of low to high diffusivity ($4 \leq Sc \leq 200$, where $Sc = \nu/D$ is the Schmidt number, ν is the kinematic viscosity and D the molecular diffusivity) mass transfer across a clean surface driven by low to moderate turbulent intensity open channel flow ($2875 \leq Re_b \leq 12000$, where $Re_b = U_b H/\nu$ is the bulk Reynolds number, U_b the bulk velocity and H the height of the open channel). The simulations were performed using the KCFlo in-house code developed by Kubrak et al. [2013]. The technical limit of previous numerical studies is overcome with the employment of a fifth-order weighted essentially non-oscillatory (WENO) scheme for the scalar convection and a dual mesh approach. In order to properly resolve the velocity field, up to 5.1×10^8 grid points were employed, while, to fully resolve the highest Schmidt and Reynolds number mass transport 1.2×10^{10} grid points were needed. The results reported here support the validity of existing experimental and numerical data obtained for moderate Reynolds numbers and different types of flow. Small eddy [Banerjee et al., 1968] and surface divergence [McCready et al., 1986] models were found to be applicable for all the Reynolds and Schmidt numbers considered. Moreover, the employment of different domain sizes, from $3H \times H \times 3H$ to $24H \times H \times 6H$, allowed for the analysis of the effects of coherent structures on interfacial mass transfer. The use of conditional average underlined the correlation between high streamwise velocity areas and low mass transfer velocity/convergence regions. The observation of 3D snapshots were used to define the role of different scales of motion in interfacial mass transfer. Both large and small structures seems to cooperate to increase the mass transfer at the surface, the former moving the latter from the wall to the surface, where they can actively enhance the process, in agreement with the "chain saw model" theorized by Moog and Jirka [1999].

In addition to the interfacial mass transfer simulations, DNSs of pollutant transport in open channel flow were also performed. In these simulations two scalars are present, one modelling the bacteria and one modelling the oxygen entering the flow from the surface of the channel. In reality, different reaction terms link these two species and define the self-purification capabilities of the system. Here, a parameter sensitivity analysis of UV-inactivation, natural decay and bacterial oxygen consumption rates was performed to assess the effect of these reaction terms on oxygen and bacterial decays. The only mechanisms that showed to have an impact on pollutant transport were maintained active to study the effects that spatial heterogeneities, typical of turbulent flows, have on the phenomenon. The small vortical motions were found to create filament structures with high concentration of bacteria which locally might pose serious

Abstract

danger to living organisms, e.g. fish, and cannot be detected when only the average bacterial concentration is considered.

Zusammenfassung

Das zentrale Thema der vorliegenden Arbeit ist die Untersuchung des Massenaustauschs entlang der Grenzfläche zwischen Wasser und Luft in einer turbulenten offenen Kanalströmung mittels direkter numerischer Simulation (DNS). Trotz der hohen wissenschaftlichen Relevanz dieses Phänomens sind die genauen Mechanismen bis heute nicht vollkommen geklärt. Atmosphärische Gase haben in Wasser für gewöhnlich ein sehr geringes Diffusionsvermögen, sodass sich dünne, langgezogene Strukturen mit ausgeprägten Gradienten bilden. Sowohl die Notwendigkeit von innovativen Technologien für die experimentelle Untersuchung dieses Phänomens als auch der sehr hohe Rechenaufwand in direkten numerischen Simulationen aufgrund der extrem feinen Gitterauflösung haben bis heute die Entwicklung eines einheitlichen Models für den Gastransfer verhindert.

Die vorliegend Arbeit zeigt Ergebnisse direkter numerischer Simulationen von schwach bis stark diffusivem Massenaustausch entlang einer sauberen Oberfläche ($4 \leq Sc \leq 200$, wobei $Sc = \nu/D$ die Schmidtzahl, ν die kinematische Viskosität und D das molekulare Diffusionsvermögen darstellen) in offenen Kanalströmungen bei geringer bis mittlerer Turbulenzintensität ($2875 \leq Re_b \leq 12000$, wobei $Re_b = u_b H/\nu$ die *bulk* Reynoldszahl, u_b die *bulk* Geschwindigkeit und H die Höhe des offenen Kanals bezeichnet). Die direkten numerischen Simulationen wurden mit dem hauseigenen, von Kubrak et al. [2013] entwickelten Simulationscode KCFlo durchgeführt. Um die technischen Einschränkungen früherer numerischer Untersuchungen zu überwinden, wird dabei ein weighted essentially non-oscillatory (WENO) Schema fünfter Ordnung zur numerischen Lösung der skalaren Konvektion in Kombination mit einem Zwei-Gitter-Verfahren angewendet. Zur Auflösung aller relevanten Skalen des turbulenten Geschwindigkeitsfeldes wurden bis zu 5.1×10^8 Gitterpunkte verwendet, wohingegen für eine volle Auflösung des skalaren Massentransports für die höchste Werte der Schmidt- und Reynoldszahl eine Gesamtzahl von 1.2×10^{10} Gitterpunkten benötigt wurden.

Die hier präsentierten Ergebnisse bestätigen Beobachtungen aus früheren experimentellen und numerischen Untersuchungen für moderate Reynoldszahlen und verschiedene Strömungssituationen. Wie sich zeigt, sind sowohl Small-Eddy-Modelle [Banerjee et al., 1968] als auch Surface-Divergence-Modelle [McCready et al., 1986] für die hier untersuchten Reynolds- and Schmidtzahlen anwendbar. Eine Variation der Größe des Rechengebiets von $3H \times H \times 3H$ bis zu $24H \times H \times 6H$ ermöglichte es ferner, den Einfluss kohärenter Strukturen auf den Massenaustausch entlang der Grenzfläche genauer zu analysieren. Mit Hilfe eines conditional averaging-Ansatzes konnte gezeigt werden, dass eine Korrelation zwischen Regionen hoher Geschwindigkeit in der Hauptströmungsrichtung und solchen, in denen eine verringerte Geschwindigkeit des Massenaustausches vorherrscht, besteht. Dreidimensionale Darstellungen der Strömung und des Skalartransports wurden darüber hinaus herangezogen, um die Rolle von Strukturen verschiedener Skalen auf den Massenaustausch zu untersuchen. Dabei wurde beobachtet, dass große und kleine Strukturen scheinbar gemeinsam für eine Verstärkung des Massenaustauschs an der Oberfläche sorgen, indem Erstere die Letzteren von der unteren Wand zur Oberfläche bewegen, wo diese die Prozesse aktiv verstärken können. Der beschriebene Prozess zeigt eine gute Übereinstimmung mit dem von Moog and Jirka [1999] entwickelten "chain saw model".

Zusätzlich zu den Simulationen des Massenaustauschs entlang der Grenzfläche wurden weitere direkte numerische Simulationen des Schadstofftransports in offenen Kanalströmungen durchgeführt. In diesen Simulationen wurden zwei Skalarfelder betrachtet, von denen eines eine Bakterienverteilung darstellt, während das andere den Sauerstoffeintrag über die Kanaloberfläche modelliert. Tatsächlich sind beide Felder über verschiedene Reaktionsterme gekoppelt, die die Fähigkeit zur Selbstreinigung des Systems widerspiegeln. In der vorliegenden Arbeit wurde dazu eine Sensitivitätsanalyse bzgl. der Deaktivierung durch UV-Strahlung, des natürlichen Abbaus sowie der Rate der Sauerstoffabnahme durchgeführt, um den Einfluss dieser Reaktionsraten auf die Abnahme an Sauerstoff und Bakterienkonzentration zu bewerten. Diejenigen Mechanismen, die einen Einfluss auf den Schadstofftransport aufwiesen, wurden aktiviert um den Einfluss der räumlichen Heterogenität turbulenter Strömungen auf den Schadstofftransport zu bewerten. Insbesondere für kleinskalige Wirbelbewegungen wurde beobachtet, dass sich filamentartige Strukturen mit hoher Bakterienkonzentration ausbilden. Diese lokal stark erhöhten Bakterienkonzentrationen können eine ernsthafte Gefahr für lebende Organismen wie Fische darstellen, sie lassen sich jedoch nicht durch Modelle abbilden, die sich ausschließlich auf gemittelte Bakterienkonzentrationen stützen.

Acknowledgements

I would like to thank my advisors, Dr.-Ing. Herlina and Prof. Markus Uhlmann, for their patience and their valuable critiques that made me grow as researcher. Thanks to them, I understood the necessity to be precise in every part of the work, from the emails to the writing of a manuscript. Moreover, their vast combined knowledge of fluid dynamics and mass transfer allowed me to understand how deep and wide the turbulent world is and how much work and time is necessary to produce quality research.

I would like to thank Prof. Bernd Jähne for accepting the role of external reviewer for my thesis. I would like to express my appreciation to Prof. Harald Horn, Prof. Olivier Eiff, Prof. Stefan Hinz and Prof. Josef Winter for their interest in my work and their availability as members of my Ph.D. committee.

I would like to thank my wife Giulia for her countless support and patience in these years and, particularly, in this last period. Without her, I am sure I would have not been able to finalize my Ph.D.. She allowed me to grow as a human being and understand that sometimes in life you have to make some decisions that maybe were against your previous beliefs. She helped me empathizing with other people's choices and made me see that the world is not black or white. Thank you my love, I am sure you will be a great mum for Emma.

I thank my mother Augusta and my father Mauro for letting me always choose my way and make sacrifices to allow me to follow what I thought it was my path. They taught me that, in life, you should pursue what makes you happy, without caring about other people's comments. I hope I will be a parent as good as you were for me. I would like to thank my brother Luca for teaching me to think out of my mental schemes. You are always ready to discuss with me to expand my horizons. Thank you also for keeping my library always full of good books!

I would like to thank Dario, Gio and Luca for the countless funny nights spent together in Karlsruhe and their support during lockdown times. I would like to thank all my friends and coworkers Manu, Antoine, Yulia, Michele, Michael and Markus for sharing anxiety, experience and fun all together. I would also like to extend my thanks to Angelika, Conny, Heidi, Helmut at IfH for their technical and administrative support.

I would like to thank my wife Giulia for her countless support and patience in these years

This work is dedicated to my daughter, Emma.

Contents

Contents

Acronyms and symbols

Acronyms

DNS	direct numerical simulation
FH2	supercomputer forHLR2 at SCC (KIT)
FIB	fecal indicator bacteria
IFH	Institute for Hydromechanics
KIT	Karlsruher Institute of Technology
LES	large eddy simulation
LIF	laser induced fluorescence
LSM	large scale motions
PIV	particle image velocimetry
SCC	Steinbuch Centre for Computing
SPVS	surface parallel vortical structures
UC1	supercomputer bwUnicluster 1 at SCC (KIT)
UC2	supercomputer bwUnicluster 2 at SCC (KIT)
VLSM	very large scale motions
WENO	weighted essentially non-oscillatory

Latin symbols and variables

A	time-varying part of the streamwise velocity
A_{gs}	area of the gas-liquid interface
$\mathbf{b}$	anisotropy tensor
B	log law constant
c_0	initial concentration of the solution
c	concentration
c_b	concentration in the bulk of the channel
c_B	bacterial concentration
c_β	expansion coefficient of f_b
c_e	concentration of the solution corresponding to partial pressure of solute

Acronyms and symbols

c_g	concentration for mass transfer simulations
$c_{g,s}$	solute concentration in the atmosphere
c_{O_2}	concentration of oxygen in pollutant transport simulations
c_l	concentration of gas in the liquid phase
$c_{l,s}$	solute concentration in the liquid phase
$c_{O_2,b}$	concentration of oxygen in the bulk of the channel
$c_{O_2,s}$	concentration of oxygen at the surface of the channel
c_s	concentration at the surface
Sc	Schmidt number
D	molecular diffusivity
E	energy spectrum function
$\mathbf{f}$	dynamically adjusted forcing term added to the momentum equation to ensure a constant flow rate
f_b	standard Boussinesq buoyancy term due to thermal expansion of the fluid
f_R	refinement factor
f_x	streamwise component of $\mathbf{f}$
H	open channel height
I	measure of Reynolds stress anisotropy
I_0	average surface UV irradiance
I_y	UV irradiance
$\mathbf{j}$	mass flux vector
j_y	mass flux in vertical direction
j_d	diffusive mass flux in vertical direction
j_t	turbulent mass flux in vertical direction
j_s	mass flux at the surface
k	turbulent kinetic energy
$\mathbf{k}$	wavenumber
k_{att}	UV attenuation factor
K_E	mass transfer velocity due to eddy diffusion
k_l	mass transfer velocity at the surface
K_L	averaged mass transfer velocity at the surface

x

$(K_L)_g$	mass transfer velocity in the atmosphere
$(K_L)_l$	mass transfer velocity in the liquid
$(K_L)_g^t$	mass transfer velocity seen from the atmosphere
$(K_L)_l^t$	mass transfer velocity seen from the liquid
k_T	thermal diffusivity
$L_{\Phi\Phi}^r$	integral length scale of Φ in direction r
l_0	lengthscale of the large scales
L_B	Batchelor scale
l_{DI}	lengthscale dividing dissipation and inertial sub-ranges
l_{EI}	lengthscale dividing inertial and energy-containing sub-ranges
l_v	viscous scale
L_x	streamwise extension of the numerical domain size
L_y	vertical extension of the numerical domain size
L_z	spanwise extension of the numerical domain size
n_x	number of grid points in streamwise direction
n_y	number of grid points in vertical direction
n_z	number of grid points in spanwise direction
p	hydrodynamic pressure
P	production of turbulent kinetic energy
Pr	Prandtl number
Q	second invariant of the velocity gradient tensor
R	mass transfer resistance
$\mathcal{R}$	pollutant transport reaction rate
$\mathcal{R}_B$	total bacterial decay rate
$\mathcal{R}_G$	bacterial decay rate due to the presence of oxygen
$R_{\Omega_i\Omega_j}^r$	averaged two-point, one-time auto-covariance of a random field Ω in $\boldsymbol{r}$ direction
$R_{\Omega_1\Omega_2}$	time cross-correlation between variables Ω_1 and Ω_2
$\mathcal{R}_{nat}$	bacterial natural decay rate
$\mathcal{R}_{O_2}$	reaction rate of oxygen in pollutant transport simulations
$\mathcal{R}_{UV}$	bacterial inactivation rate due to UV-light

Re	Reynolds number
Re_b	bulk Reynolds number
Re_τ	friction Reynolds number
Re_T	turbulent Reynolds number
s	mean rate of production of fresh surface
$\mathbf{S}$	rate-of-strain tensor
Sh	Sherwood number
t	time
t_d	time constant for the transport across the diffusive boundary layer
T	temperature
t_b	bulk time units
t_e	time of exposure
T_{EI}	rate of transfer between inertial and energy-containing sub-ranges
T_x	Lagrangian integral time scale
$\mathbf{u}$	fluid velocity vector
u	streamwise component of the fluid velocity vector
u^+	velocity in viscous units
U_{10}	wind speed $10\,m$ above the water surface
$\mathbf{U}(\mathbf{x}, t)$	time-dependent velocity field
U_b	bulk velocity
U_p	velocity of points inside pollutant cloud
u_η	Kolmogorov velocity scale
u_τ	friction velocity
v	vertical component of the fluid velocity vector
w	spanwise component of the fluid velocity vector
W_β	spectral function for surface divergence
x	streamwise direction
X_p	mean size of pollutant cloud
y	vertical direction
y^+	wall units
z	spanwise direction

Greek symbols and variables

α solubility

α_{UV} UV sensitivity coefficient

β time-varying part of the vertical velocity gradient: surface divergence

γ time-varying part of the spanwise velocity gradient

δ diffusive boundary layer thickness

δ_{SI} surface-influenced layer thickness

δ_ν viscous scale

ϵ turbulent dissipation rate

ϵ_x streamwise pollutant diffusion coefficient

ϵ_y vertical pollutant diffusion coefficient

ϵ_z spanwise pollutant diffusion coefficient

η Kolmogorov lengthscale

η_b, ξ_b non-trivial anisotropy tensor invariants

ω velocity fluctuation frequency

$\boldsymbol{\Omega}$ vorticity tensor

κ von Kármán constant

Λ lengthscale of large eddies

λ wavelength

ν kinematic viscosity

ρ_f fluid density

$\rho(*, \cdot)$ correlation coefficient between $*$ and $\cdot$

τ total shear stress

τ_η Kolmogorov timescale

τ_w shear stress at the wall

$\boldsymbol{\Phi}$ spectrum tensor or Fourier space representation of the two-point correlation

ϕ constant of the surface divergence model

φ phase shift

Operators and math symbols

$*$	instantaneous value of the quantity $*$
$*_{rms}$	root mean square of the quantity $*$
$\langle * \rangle$	average in homogeneous x, z directions of the quantity $*$
$\langle * \rangle_r$	average of the quantity $*$ in r direction
$\overline{*}$	time average of the quantity $*$

List of Figures

List of Figures

List of Tables

1 Introduction

Interfacial gas transfer depends upon a complex interplay between different factors. Physical, chemical, biological mechanisms are only few of the vast number of phenomena playing a role in gas transfer. These factors are far from being completely understood today and are usually approximated by simplified models that, most of the time, are flow dependent. In the present thesis, massively parallel computer simulations of a mathematical model which resolves all scales of hydrodynamics and concentration fields of dissolved scalars (e.g. pollutant and gas) are performed. The analysis presented here focuses on interfacial mass transfer and, in addition, on the fate of freely-suspended fecal indicator bacteria (FIB) in turbulent open channel flow. The present large scale simulations revealed the relative importance of the various mechanisms through which the spatio-temporal heterogeneities of the flow affect scalar transport.

1.1 Motivation

Transfer of gases across a gas-liquid interface is a fundamental process in several research fields, from civil engineering to biology. The quantity of gases exchanged between water and atmosphere is a key factor for marine life and the balance of green-house gases present on Earth. The quantity of oxygen present in water basin strongly affects the aquatic environment and it must be constantly replaced in order for the life cycle to continue. This natural mechanism is called reaeration and is fundamental for each species living in water. Moreover, DeVries et al. [2017] demonstrated that the ocean is the largest sink of carbon dioxide, taking up to 40% of the CO_2 produced by human activities. Gas transfer is also a process often employed in man-made facilities in order to e.g. remove taste and odor from drinking water or treat wastewater. These few examples show how important and ubiquitous this phenomenon is and underlines how its study can improve water quality assessment and management.

Flow conditions strongly affect interfacial mass transfer. In fact, generally, a turbulent environment tends to spread scalars much faster. The small vortices will enhance the mixing, which will be much higher than the one produced by molecular diffusion only. Since in nature turbulence is ubiquitous, a study of the mass transfer without considering turbulence would be much less complex, but rarely applicable to reality. The main sources of turbulence in nature are surface-shear-induced turbulence, buoyant-convective turbulence and bottom-shear-induced turbulence. Surface-shear-induced turbulence is caused by e.g. wind shear on the water basin surface. In this case, turbulence is generated at the surface and then spread over the whole channel. Wind shear is usually the driving mechanism in gas transfer and it was widely studied in previous research (see section 2.2.4.5). Buoyant-convective turbulence is generated, for example, in the case colder/warmer fluid (e.g. pollutant) is discharged into a river. The temperature gradients locally modify the flow density, causing movements that would be absent if buoyancy was neglected. Bottom-shear-induced turbulence is usually caused by the presence of a wall at the bottom of the channel, in the nearby of which the production of turbulent kinetic energy reaches its maximum. The present study focuses on interfacial mass transfer in rivers in windless conditions. Buoyancy is not considered and turbulence is caused uniquely by the shear stress induced by the presence of the wall at the bottom of the channel.

In the last decades, the inadequacy of technologies underlined the inability of experimental apparatus to assess the main factors playing a role in interfacial mass transfer, hindering the development of a unified model, even in simplified experimental set-ups. In contrast, direct numerical simulation did not allow to reach Schmidt ($Sc = \nu/D$, where ν is the kinematic viscosity and D the molecular diffusivity) and friction Reynolds numbers ($Re_\tau = u_\tau H/\nu$, u_τ the friction velocity and H the height of the open channel) found in real rivers, because atmospheric gases usually have very low diffusivities (high Schmidt numbers) in water. Consequently, they will tend to create thin, elongated structures in which very steep gradients can be found, requiring extremely fine grid resolutions that made the simulations unfeasible. The most significant experimental and numerical works of past studies are summarized in chapter 2.

Another important problem that will be tackled in the thesis is pollutant transport. The fate of pollutants in surface water, which, in turn, affects the water quality, is usually approximated by oversimplified models that employs empirically-fitted coefficients. Consequently, water quality predictions based upon state-of-the-art mathematical models still suffer large uncertainties. Moreover, the temperature of the sewage discharge is usually different from the one of the water basin and consequently a combination of bottom-shear and buoyancy-induced turbulence is considered for the pollutant transport simulations, making the simulations more complex.

1.2 Methodology

Interfacial mass transfer over a flat surface and pollutant transport in turbulent open channel flow were investigated numerically. All the direct numerical simulations were performed employing the existing in-house KCFlo code described in Kubrak et al. [2013] (see chapter 3).

While in direct numerical simulation the equations are solved for a time-dependent velocity field $\boldsymbol{U}(\boldsymbol{x}, t)$ for each realization of the turbulent flow, in a turbulent model, equations are solved for some mean quantities, e.g. $\langle \boldsymbol{U} \rangle$, $\langle \boldsymbol{uu} \rangle$ or ϵ. Since all the length-scales and time scales of the turbulent flow are resolved for each time step, direct numerical simulation is computationally very expensive. The computational costs of DNS grows as Re^3 and, when scalars with low diffusivities are present, as $(f_R^3 Re^3)$ (see section 3.3), where f_R defines how many times the scalar grid is finer than the velocity grid. In a large eddy simulation (LES), equations are solved for a filtered velocity field $\tilde{\boldsymbol{U}}(\boldsymbol{x}, t)$ and only the large-scale motions are fully resolved. The computational costs are then much smaller since the small scales of motion are modelled. Unfortunately, mass transfer and pollutant transport for high Reynolds and Schmidt numbers are driven by small scales motions (cf. section 2.2.4.3.2). Using LES would translate in approximations that hinder the validity of the research. The flow and scalar field close to the surface, where interfacial mass transfer needs to be studied, and at the wall, where pollutants usually sink, would not be resolved, giving uncertainties in the most important regions. This is why DNS was employed, even though the computational costs are much higher.

As underlined above, thin boundary layers and steep scalar gradients are the main reasons why previous direct numerical simulation studies were limited to moderate Reynolds and very low Schmidt numbers. Moreover, the amount of computational hours needed to resolve the smallest scales of both scalars and velocity fields hindered the possibility to employ large domain sizes, which are needed to capture very large scale motions. Kubrak et al. [2013] developed the KCFlo code specifically to overcome these limits and it was used, in the past, to simulate mass transfer at the gas-water interface of flow driven by isotropic turbulence diffusing from below [Herlina and Wissink, 2014, 2019, Wissink et al., 2017] and buoyancy-induced convection

[Wissink and Herlina, 2016]. The KCFlo solver employs a central finite-difference approach with a fourth-order accurate discretization of the diffusion and a fourth-order-accurate kinetic energy conserving discretization for the convection to resolve the flow field. The Poisson equation for pressure, obtained imposing the incompressibility restraint to the divergence of the momentum equation, is solved using a conjugate gradient solver, with simple diagonal preconditioning. A fifth-order weighted essentially non-oscillatory (WENO) scheme for the scalar convection combined with a fourth-order accurate central method for scalar diffusion are employed. The time integration for velocity and scalar fields is performed with a second-order Adams-Bashforth scheme. The code allows to resolve up to five advection-diffusion equations for every time step, providing a direct comparison of the behavior of scalars with different diffusivities developed in the exact same turbulent flow field.

1.3 Objectives

Chapter 2 shows that most of previous research was focused on quantifying interfacial mass transfer velocity by trying to relate it to easily measurable parameters. Even if this approach seems to work in some situations, unfortunately it is far from being universally applicable. The reason is that the mechanisms causing changes in mass transfer are still not completely understood. Previous experimental studies showed disagreement in the definition of the coefficients to apply for mass transfer models, which were found to depend on the flow characteristics. On the other hand, previous direct numerical simulations of mass transfer in open channel flow were limited to small Schmidt numbers, but, most importantly, the domains considered were very small, not allowing the simulations to capture very large scale motions (VLSM). In order to make a step forward toward a better comprehension of low diffusivity scalar transport phenomena, it is necessary to elucidate the role of all the structures present in turbulent open channel flow. Therefore, several direct numerical simulations spanning from low to moderate Reynolds numbers and Schmidt numbers ranging from 4 to 200 were performed in different domain sizes, from $3H \times H \times 3H$ to $24H \times H \times 6H$. The literature review summarized in chapter 2 underlines the key knowledge gaps in the study of mass transfer and pollutant transport in open channel flow. The specific goals of the present thesis are the following:

- clarify the dependency of mass transfer parameters on Reynolds number, Schmidt number and domain size,

- show the limits and the advantages of mass transfer models applied to open channel flow,

- define the effects of the different scales of motion on mass transfer,

- define which are the non-negligible decay and reaction rates of oxygen and bacteria, after a sewage discharge in a river. In particular, scalars initial boundary conditions, differences in temperature between FIB and ambient fluid, natural inactivation, UV-inactivation and depletion of bacteria due to the presence of oxygen were considered,

- determine the effect of spatial heterogeneities in pollutant transport.

.

1.4 Organization of the thesis

The present chapter contains a description of the problem under consideration, a small summary of the reasons why we employed direct numerical simulation to study it and the objectives

of this thesis. The rest of the thesis is structured as follows. Chapter 2 introduces the mathematical formulation for each component of the problem and summarizes the theories developed until today for mass transfer and pollutant transport. A literature review including the most important and recent experimental and numerical works closes the chapter. Chapter 3 describes the numerical method employed. The description of the domain opens the chapter, while an analysis of the code performance closes it. It was chose not to describe the code in detail, since no modifications to it were applied by the author of the thesis. In the present work, the simulations performed can be split into three large groups. The first group contains the flow simulations needed to achieve a statistically stationary turbulence, before imposing the presence of the scalars. The statistics of these simulations are shown in chapter 4. The grid resolutions and the domain sizes employed are tested, confirming that, while the grid resolutions were fine enough to capture the smallest scales in all the simulations, only the largest domain employed qualified to capture the very large scale motions. The second group of simulations were performed employing the first group simulations velocity fields. After the statistical stationarity was achieved, a scalar is introduced at the top of the channel through a Dirichlet boundary condition that imposes constant feeding from the top of the channel. This boundary condition was imposed to mimic the interfacial mass transfer due to the contact between the basin of water with the atmosphere at the top of the channel. The statistics pertaining to this group of simulations are shown in chapter 5. The chapter starts with the analysis of the adequacy of the refinement factors chosen, followed by the scalar statistics that confirms the adequacy of the time windows chosen for the average. A comparison with the models described in chapter 2 follows. The study of the interaction between coherent structures and mass transfer closes the chapter. Chapter 6 illustrates the results of the pollutant simulations. In this case, a Neumann boundary condition imposing zero flux at the surface of the channel was imposed. The effect of the initial shape of the pollutant cloud was considered using two different initial conditions. A parameter sensitivity analysis was performed, in order to assess what are the most important variables for the self-purification mechanism. The role of spatial heterogeneities in pollutant accumulation was studied, in order to define the risks that the employment of over-simplified models based on averaged quantities could introduce. The last chapter contains a summary of the thesis and suggestions for future works.

2 State of the art

The present chapter introduces some fundamental concepts relevant to this work. The chapter is divided in four main sections, the first one describing the flow field, the second one focusing on mass transfer, the third one on pollutant transport and the last one summarizing previous literature on the subject. The first three sections start with the governing equations, followed by the most important theories elaborated in the past. In the end, the experimental and numerical studies performed in the last decades are summarized in the last section. Note that in the following chapter the spatio-temporal dependency of flow and scalar variables will be omitted ($\phi(\boldsymbol{x}, t) = \phi$), unless otherwise specified. Each quantity can be split in a mean and a fluctuating component. Since, in the present thesis, the statistical average is approximated by time $\bar{\cdot}$ and plane-averaging $\langle \cdot \rangle$, the mean part of $\cdot$ will be written as $\overline{\langle \cdot \rangle}$, while $\cdot'$ represents its fluctuating component. Therefore, each quantity can be written as follows:

$$\cdot = \overline{\langle \cdot \rangle} + \cdot'. \tag{2.1}$$

2.1 Fundamentals of open channel flow

This section is devoted to introduce mathematical and statistical concepts of open channel flows. At first, the governing equations for this flow typology will be presented. The second subsection depicts the theory behind the multi-scale nature of turbulent flows, while the last part is a summary of the fundamentals of open channel flow.

2.1.1 Governing equations

The governing equations for an open channel flow are the incompressible Navier-Stokes equations that in vector notation read:

$$\frac{\partial \mathbf{u}}{\partial t} + (\mathbf{u} \cdot \boldsymbol{\nabla})\mathbf{u} + \frac{1}{\rho_f}\boldsymbol{\nabla} p = \nu\nabla^2\mathbf{u} + \boldsymbol{f_b} + \boldsymbol{f}, \tag{2.2}$$

$$\boldsymbol{\nabla} \cdot \mathbf{u} = 0. \tag{2.3}$$

In equations 2.2 and 2.3, $\mathbf{u}$ is the Eulerian fluid velocity vector and its components in each direction are (u, v, w), ρ_f the fluid density, p the hydrodynamic pressure, ν the kinematic viscosity, $\boldsymbol{f_b} = (0, c_\beta\, g(T_{b,0} - T), 0)$ the standard Boussinesq buoyancy term (due to thermal expansion of the fluid with an expansion coefficient c_β, gravitational acceleration g and initial temperature of the fluid $T_{b,0}$) and $\boldsymbol{f} = (f_x, 0, 0)$ is the dynamically adjusted forcing term added to the momentum equation to ensure a constant flow rate.

The chaotic nature of the turbulent flow arises from the non-linearity of the Navier-Stokes equations. Even though the equations are deterministic, the velocity field can be random, since the flow is highly sensitive to small variations in the initial conditions. Therefore, turbulent flows need to be described statistically.

2.1.2 Scales of turbulent motions

The fundamental aspect of turbulent flows is the simultaneous presence of large and small scale energy-containing eddies. The anisotropic large vortices are unstable in nature and their breakdown creates smaller vortices. In the same way, the new formed vortices break down into smaller ones. This breakdown process is called forward energy cascade and it usually ends with the smallest vortices being dissipated by the viscous dissipation process into heat (Richardson [1922]). The opposite happens in the inverse energy cascade, when the smaller vortices coalesce into larger structures. This last phenomenon is much less frequent compared to the forward cascade, but it can be observed in real-world turbulence (e.g. rivers).

The length and time scale of these vortices were defined for the first time in a theory proposed by Kolmogorov [1941]. This theory stands on three hypotheses. The hypothesis of local isotropy is based on the fact that the anisotropy of the large scales is gradually lost in the forward energy cascade. This hypothesis states that "at sufficiently high Reynolds numbers, the small scale turbulent motions ($l \ll l_0$) are statistically isotropic" (Pope [2000]). l_0 is considered to be the dimension of the largest scales of the flow. Since the directional information is lost as the energy passes down the cascade, Kolmogorov [1941] argued that all the directional information about the geometry of the large eddies, determined by the flow boundary conditions, is also lost. As a consequence, he proposed that the statistics of the small scales are somehow universal. It is useful here to define a length scale below which the small scales can be considered isotropic $l_{EI} = \frac{1}{6} l_0$. The dominant processes, when $l < l_{EI}$, are the transfer of energy towards smaller scales that depends on a rate of transfer T_{EI} and the viscous dissipation ν. The transfer rate can be approximated by the dissipation ϵ, such that the first Kolmogorov hypothesis can be stated as "in every turbulent flow at sufficiently high Reynolds number, the statistics of the small scale motions ($l < l_{EI}$) have a universal form that is uniquely determined by ν and ϵ" (Pope [2000]). As a consequence, the size range $l < l_{EI}$ is referred to as the universal equilibrium range. Given the two parameters that completely determine the flow field in this range, ν and ϵ, the Kolmogorov scales can be defined:

$$\eta \equiv \left(\frac{\nu^3}{\epsilon} \right)^{1/4}, \tag{2.4}$$

$$u_\eta \equiv (\epsilon \nu)^{1/4}, \tag{2.5}$$

$$\tau_\eta \equiv \left(\frac{\nu}{\epsilon} \right)^{1/2}. \tag{2.6}$$

The definition of a Reynolds number based on these quantities $Re_\eta = \frac{\eta u_\eta}{\nu} = 1$ shows that these scales characterize the smallest, dissipative eddies. Being the Reynolds number the ratio between inertial and viscous forces, $Re_\eta = 1$ means that viscous forces are effective. When the turbulent velocity fields are scaled by the Kolmogorov scales, they are statistically similar. The above statement is valid only for high Reynolds numbers flow and considering only the universal range (small scales).

Figure 2.1: Extent in outer scales of the different regions in turbulent wall-bounded flow as a function of the Reynolds number. Image taken from Pope [2000]

The ratios between largest and smallest scales can be determined considering that $\epsilon \sim u_0/l_0$. Applying this approximation to the Kolmogorov scales, the ratios read:

$$\frac{\eta}{l_0} \sim Re^{-3/4}, \tag{2.7}$$

$$\frac{u_\eta}{u_0} \sim Re^{-1/4}, \tag{2.8}$$

$$\frac{\tau_\eta}{\tau_0} \sim Re^{-1/2}. \tag{2.9}$$

When higher Reynolds numbers are considered, the difference between large and small scales becomes much larger. At sufficiently high Reynolds numbers, there is an intermediate range of scales, lying between l_0 and η, in which the spatial Reynolds number becomes $Re \gg 1$ and, consequently, the eddies motion is little affected by viscosity. Starting from this statement and the first similarity hypothesis, Kolmogorov [1941] proposed his second similarity hypothesis, which states that "in every turbulent flow at sufficiently high Reynolds number, the statistics of the motions of scale l in the range $l_0 \gg l \gg \eta$ have a universal form that is uniquely determined by ϵ, independent of ν" (Pope [2000]). This hypothesis is applicable in the range $l_{EI} > l > l_{DI}$, where $l_{DI} = 60\eta$ is the length scale that splits the universal equilibrium range ($l < l_{EI}$) into inertial sub-range $l_{EI} > l > l_{DI}$ and dissipation range $l < l_{DI}$. While only inertial effects are important in the inertial range, the dissipation range experiences significant viscous effects, which are responsible for all the dissipation of the channel.

2.1.3 Fundamentals of wall-bounded flows

If H is the vertical height of the open channel, the bulk velocity can be defined as follows:

$$U_b = \frac{1}{H} \int_0^H \overline{\langle u \rangle} \, dy, \tag{2.10}$$

from which the bulk Reynolds number follows:

$$Re_b = \frac{U_b H}{\nu}. \tag{2.11}$$

The total shear-stress $\tau(y)$ can be obtained from the balance of the mean forces and it reads:

$$\tau = \rho\nu\frac{\partial\overline{\langle u \rangle}}{\partial y} - \rho\overline{\langle u'v' \rangle}. \tag{2.12}$$

At the wall, the boundary condition $\boldsymbol{u} = 0$ dictates that the Reynolds stresses $\overline{\langle u'v' \rangle} = 0$ and the shear stress is due entirely to the viscous contribution:

$$\tau_w = \tau(0) = \rho\nu\frac{\partial\overline{\langle u \rangle}}{\partial y}\bigg|_0. \tag{2.13}$$

The important variable in the near-wall region are viscosity ν, dissipation ϵ and the shear-stress τ_w, from which the viscous scales can be defined:

$$u_\tau = \sqrt{\frac{\tau_w}{\rho}}, \tag{2.14}$$

$$\delta_\nu = \nu\sqrt{\frac{\rho}{\tau_w}} = \frac{\nu}{u_\tau}, \tag{2.15}$$

where u_τ is the friction velocity and δ_ν is the viscous length scale. The friction Reynolds number can be defined from these quantities :

$$Re_\tau = \frac{u_\tau H}{\nu}. \tag{2.16}$$

The mean streamwise velocity in viscous units is:

$$u^+ = \frac{\overline{\langle u \rangle}}{u_\tau}. \tag{2.17}$$

The distance from the wall measured in viscous lengths is called wall units and it is denoted by:

$$y^+ \equiv \frac{y}{\delta_\nu} = \frac{u_\tau y}{\nu}. \tag{2.18}$$

It represents a local Reynolds number, since its magnitude determines the relative importance of viscous and turbulent processes.

Wall units define different regions in the flow field, which are depicted in figure 2.1. Two macro regions are defined, the inner region for $y/H < 0.1$ and the outer region for $y^+ \geq 50$. In general, the global quantities u_0 and H characterize the statistics in the outer region, while the viscous scales characterize the variables in the inner region. The inner region is usually divided into smaller regions. The region containing the smallest scales of motion is the viscous sub-layer and it satisfies $u^+ = y^+$. This linear relation holds for $y^+ < 5$, but the deviation from the linear behavior becomes quite large (greater than 25%) as soon as $y^+ > 12$. Moving toward the bulk of the channel, for $y^+ \geq 30$ and $y/H \leq 0.3$ the streamwise velocity in wall units is well approximated by the logarithmic law of the wall:

$$u^+ = \frac{1}{\kappa}log(y^+) + B, \tag{2.19}$$

which defines the logarithmic region. In literature, the values of the constants κ and B are topics of discussion, but usually accepted values are $\kappa \simeq 0.41$ and $B \simeq 5.2$ (Pope [2000]). Figure 2.1 shows the regions usually identified in wall-bounded turbulence. As can be seen, the

viscous sublayer and the log law regions are connected through a buffer layer ($5 \geq y^+ \geq 30$), in which the velocity adapts from the linear to the logarithmic dependency on the wall units.

2.2 Mass transfer in turbulent environment

This section presents a summary of the mass transfer phenomenon and literature. Starting from the presentation of the governing equation, the section analyzes the basic mechanisms of mass transfer and the most important models developed until today.

2.2.1 Governing equation for mass transfer

The Fick's law defines the mass flux of a solute penetrating a liquid in a laminar flow. The law states that the mass flux $\boldsymbol{j}$ is proportional to the concentration c gradient of the solute, with the molecular diffusivity D as proportionality coefficient:

$$\boldsymbol{j} = -D\boldsymbol{\nabla} c. \tag{2.20}$$

The negative sign defines the direction of the diffusion from high to low concentrations.

Since turbulent flows are ubiquitous in reality, the hypothesis of laminar flow strongly limits the direct application of this model. In fact, further terms, like mass conservation and advection, must be added, in order to take into account the turbulent motion of the flow and the consequent different dispersion of the scalar. Therefore, the governing equation can be defined to be the three dimensional advection-diffusion equation:

$$\frac{\partial c}{\partial t} + (\mathbf{u} \cdot \boldsymbol{\nabla})c = D\nabla^2 c. \tag{2.21}$$

Since mass transfer across an air-water interface acts mostly in the vertical direction, it is possible to apply some simplifications to the general equation 2.21, in order to find the spatially and temporally averaged equation. Velocity and concentration must be split in their mean and fluctuating components and introduced in equation 2.21. Applying the average, the result is:

$$\frac{\partial \overline{\langle c \rangle}}{\partial t} + (\overline{\langle \mathbf{u} \rangle} \cdot \boldsymbol{\nabla})\overline{\langle c \rangle} + \overline{\langle (\mathbf{u}' \cdot \boldsymbol{\nabla})c' \rangle} = D\nabla^2 \overline{\langle c \rangle}. \tag{2.22}$$

Applying the properties of divergence and gradient and considering the continuity equation, some simplifications can be performed:

$$\frac{\partial \overline{\langle c \rangle}}{\partial t} + (\overline{\langle \mathbf{u} \rangle} \cdot \boldsymbol{\nabla})\overline{\langle c \rangle} + \boldsymbol{\nabla} \cdot (\overline{\langle \mathbf{u}' \, c' \rangle}) = D\nabla^2 \overline{\langle c \rangle}, \tag{2.23}$$

which, for every component, becomes:

$$\frac{\partial \overline{\langle c \rangle}}{\partial t} + \overline{\langle u \rangle}\frac{\partial \overline{\langle c \rangle}}{\partial x} + \overline{\langle v \rangle}\frac{\partial \overline{\langle c \rangle}}{\partial y} + \overline{\langle w \rangle}\frac{\partial \overline{\langle c \rangle}}{\partial z} + \tag{2.24}$$

$$+ \frac{\partial}{\partial x}\overline{\langle c'u' \rangle} + \frac{\partial}{\partial y}\overline{\langle c'v' \rangle} + \frac{\partial}{\partial z}\overline{\langle c'w' \rangle} = \tag{2.25}$$

$$= D\left(\frac{\partial^2 \overline{\langle c \rangle}}{\partial x^2} + \frac{\partial^2 \overline{\langle c \rangle}}{\partial y^2} + \frac{\partial^2 \overline{\langle c \rangle}}{\partial z^2}\right). \tag{2.26}$$

Considering a fluid flowing in the x direction, at the interface between the fluid and the atmosphere the averaged vertical velocity $\overline{\langle v \rangle}$ is zero and the streamwise $\overline{\langle u \rangle}$ and spanwise $(\overline{\langle w \rangle})$ velocities depend only on y. Thus, the transport of the mean quantities mainly acts in the vertical direction, which means that $\partial/\partial x = 0$ and $\partial/\partial z = 0$. Therefore, the following simplifications can be applied:

$$\frac{\partial \overline{\langle c \rangle}}{\partial t} + \overline{\langle u \rangle}\frac{\partial \overline{\langle \cancel{c} \rangle}}{\partial \cancel{x}} + \overline{\langle \cancel{v} \rangle}\frac{\partial \overline{\langle c \rangle}}{\partial y} + \overline{\langle w \rangle}\frac{\partial \overline{\langle \cancel{c} \rangle}}{\partial \cancel{z}} + \tag{2.27}$$

$$+ \frac{\partial}{\partial \cancel{x}}\overline{\langle c'u' \rangle} + \frac{\partial}{\partial y}\overline{\langle c'v' \rangle} + \frac{\partial}{\partial \cancel{z}}\overline{\langle c'w' \rangle} = \tag{2.28}$$

$$= D\left(\frac{\partial^2 \overline{\langle \cancel{c} \rangle}}{\partial \cancel{x}^2} + \frac{\partial^2 \overline{\langle c \rangle}}{\partial y^2} + \frac{\partial^2 \overline{\langle \cancel{c} \rangle}}{\partial \cancel{z}^2}\right), \tag{2.29}$$

giving the averaged governing equation:

$$\frac{\partial \overline{\langle c \rangle}}{\partial t} = \frac{\partial}{\partial y}\left(-\overline{\langle c'v' \rangle} + D\frac{\partial \overline{\langle c \rangle}}{\partial y}\right) = -\frac{\partial}{\partial y}\overline{\langle j_y \rangle}, \tag{2.30}$$

where $\overline{\langle j_y \rangle}$ is the average vertical mass flux:

$$\overline{\langle j_y \rangle} = -\overline{\langle c'v' \rangle} + D\frac{\partial \overline{\langle c \rangle}}{\partial y}. \tag{2.31}$$

2.2.2 Parameters in mass transfer

The present sub-section is based on the findings of Jähne and Haußecker [1998]. Equation 2.31 introduces the definition of the average vertical mass flux $\overline{\langle j_y \rangle}$, which is composed by a turbulent $\overline{\langle j_t \rangle} = \overline{\langle c'v' \rangle}$ and a diffusive $\overline{\langle j_d \rangle} = -D\,\partial\overline{\langle c \rangle}/\partial y$ component. From this definition, it is possible to define the average mass transfer velocity as the velocity at which an imaginary piston pushes the gas across the interface [Jähne and Haußecker, 1998]:

$$K_L = \frac{\left|\overline{\langle j_s \rangle}\right|}{c_s - \overline{\langle c_b \rangle}}, \tag{2.32}$$

where the indices s and b denote the surface of the flow and its bulk. The instantaneous and pointwise value of the mass transfer will be denoted as:

$$k_l(x, z, t) = \left|\frac{-D\left(\partial c(x, z, t)/\partial y\right)_s}{c_s - \overline{\langle c_b \rangle}}\right|. \tag{2.33}$$

The reciprocal of the average mass transfer velocity is the mean mass transfer resistance and it measures the resistance that the gas must overcome in order to penetrate the liquid:

$$R = \frac{1}{K_L}, \; r = \frac{1}{k_l}. \tag{2.34}$$

The boundary layer thickness can be then defined as follows:

$$\delta = \frac{D}{K_L}, \tag{2.35}$$

and it represents the thickness of a layer in which the flux is maintained only by the molecular transport. From the ratio of this quantities it is possible to define a time constant for the transport across the boundary layer:

$$t_d = \frac{\delta}{K_L} = \frac{D}{K_L^2}. \tag{2.36}$$

These three quantities (2.32, 2.35 and 2.36) completely define the scalar boundary layer and are coupled through the molecular diffusion coefficient. Therefore, only one of these parameters should be known in order to deduce the other two. It is customary to define the mass transfer velocity and then to compute all the other quantities.

2.2.3 Basic mechanisms of mass transfer

Turbulence, solubility and surface roughness are the mechanisms found to enhance the interfacial mass transfer. An increase in the turbulence intensity translates in a thinning of the boundary layer and, as a consequence, an increase of the mass transfer velocity. Solubility α is another important parameter, since it determines which boundary layer is dominant in the mass transfer process [Jähne and Haußecker, 1998]. In fact, at the surface:

$$c_{l,s} = \alpha c_{g,s}, \tag{2.37}$$

where $c_{l,s}$ is the solute concentration in the liquid and $c_{g,s}$ is the solute concentration in the atmosphere at the interface. Equation 2.37 states that if $\alpha \neq 1$, there is a concentration jump at the surface and the flux densities differ by a factor of α. Considering that mass transfer resistances can be modelled as electrical resistances in series and that $R = 1/K_L$, it follows [Liss, 1973]:

$$\frac{1}{(K_L)_g^t} = \frac{1}{(K_L)_g} + \frac{1}{\alpha(K_L)_l} \quad \text{or} \quad \frac{1}{(K_L)_l^t} = \frac{\alpha}{(K_L)_g} + \frac{1}{(K_L)_l}. \tag{2.38}$$

where $(K_L)_g^t$ and $(K_L)_l^t$ are the transfer velocities seen from the atmosphere and from the liquid, respectively. The ratio $\alpha(K_L)_l/(K_L)_g$ determines which boundary layer controls the transfer process. Since most of atmospheric gases have usually low to very low solubility in water, but high solubility in gases, the higher resistance will be in the water part and the mass transfer will be controlled by the water boundary layer.

Waves are another fundamental mechanism that plays a huge role in mass transfer. It has been seen that in the presence of waves the mass transfer velocity is three to five times larger than the one registered for a flat surface [Jähne and Haußecker, 1998]. This difference cannot be explained by the increased surface, since the surface that Tschiersch and Jähne [1980] measured, also for high wind speed, was only 20% larger than a flat surface. The understanding of this phenomenon is really limited and the few models proposed until today cannot be proved to be valid through experiments or numerical simulations. Breaking waves are more complex and the only knowledge grasped is that they significantly enhance the mass transfer velocity, but the details of this mechanisms are still to be found.

2.2.4 Mass transfer models

Mass transfer velocity is one of the most important parameters considered in interfacial mass transfer research. Once this quantity is known, all the other parameters describing the process
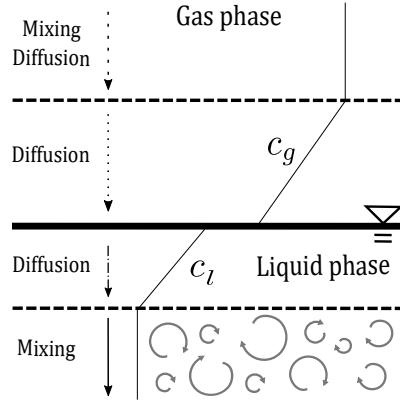
Figure 2.2: Sketch of the film model.

can be estimated from it, as mentioned above. This is the reason why, the main focus of previous research was to link the mass transfer velocity at the surface with easily measurable flow quantities. In the following, the most important models developed in the past years are summarized.

2.2.4.1 Film model

Lewis and Whitman [1924], considering the inadequacy of previous theories on gas transfer, proposed a new model based on the fact that "a liquid-gas system which is not in equilibrium tends to approach equilibrium conditions" (Lewis and Whitman [1924]). In the case of a dissolved gas in a liquid, they observed, from previous experimental data, that the leading phenomenon (the slowest one) is molecular diffusion. All the other events are so rapid compared to diffusion that they have no appreciable effect on the absorption rate. Moreover, the same experimental results showed that when gas transfer begins, two layers form at the interface, one at the gas phase and the other one at the water phase, as depicted in Figure 2.2. Inside the layers mixing is only due to molecular diffusion, while in the bulk turbulent mixing is predominant. The diffusion proceed at a rate proportional to the difference between the concentrations inside and outside the boundary layers, but, being the two layers very thin, the two films can be modelled as two resistances in series.

As underlined before, in the case of an air-water interface (low solubility gases in water), the water boundary layer has a much higher resistance, being, consequently, the leading obstacle to mass transfer. In this case, the absorption equation reads [Lewis and Whitman, 1924]:

$$\frac{\partial c}{\partial t} = K_L(c_g - c_l), \tag{2.39}$$

where c_g and c_l are the concentration of gas in the gas and liquid phase, respectively. The constant of proportionality K_L was found to be directly proportional to the diffusion coefficients of the gas in air and in water.

2.2.4.2 Penetration model

The film model was rapidly discarded, since not supported by experiments and the dependence of K_L from D was replaced by a more accurate model built by Higbie [1935]. Higbie [1935] argued that "since the surface films are very thin, the actual amount of solute in them at any one time is usually negligible compared to the amount diffusing through them". At the initial time
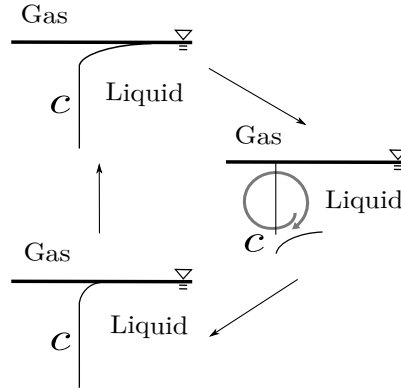
Figure 2.3: Sketch of the surface renewal theory.

(before the penetration of the gas inside the liquid), the liquid film has the same concentration of the liquid bulk. Therefore, the first stage of gas absorption will be the penetration of the gas in the liquid, from which this model takes its name. Afterward, Higbie [1935] theorized that the concentration profile will evolve, until it reaches the film behavior. Before that, the film model, proposed by Lewis and Whitman [1924], is not valid and it cannot predict the effect of diffusivity.

Starting from the Fick's second law:

$$\frac{\partial c}{\partial t} = D\nabla^2 c, \tag{2.40}$$

Higbie [1935] developed the penetration model, with the following hypotheses: heat, surface and dilation effects are negligible, the diffusivity is assumed constant and the depth infinite. With these approximations the solution of equation 2.40 is:

$$c = c_0 + \frac{c_e - c_0}{\sqrt{\pi D t}} \int_y^\infty \frac{-y^2}{e^{4Dt}} \, dy, \tag{2.41}$$

where c_e is the concentration of the solution corresponding to partial pressure of solute, c_0 is the initial concentration of the solution, y is the distance from the surface and t is the time after beginning of exposure. The mass transfer velocity is then found to be:

$$K_L = 2\sqrt{\frac{D}{\pi t_e}}, \tag{2.42}$$

where t_e is the time of exposure. The dependence of the mass transfer velocity from the time of exposure has been validated in several experiments, confirming the common experience that agitation and stirring (shortening the exposure period) increase the transfer velocity.

2.2.4.3 Surface renewal models

The first doubts on the fact that a laminar boundary layer was constantly present at the surface of a turbulent flow were raised by Danckwerts [1951]. Considering the case in which the surface of the liquid is at all times saturated by the gas, there are no chemical reactions between solute and solvent and there is no external mixing in the flow, Danckwerts [1951] pointed out how equation 2.42 largely underestimated the mass transfer velocity. In reality, he observed that after few seconds, the difference in the concentration of CO_2 in the fluid regions creates

convection currents that enhance mass transfer, since a solution with carbon dioxide is heavier than water. The liquid phase absorbed a volume of gas much larger than the quantity that molecular diffusion would have allowed. The penetration model is then a good approximation for mass transfer only if the exposure time is so short that the depth of the liquid is thicker than the depth of penetration (e.g. liquid layers of restricted depth) or if the depth of penetration is less than the depth at which the velocity is appreciably different from that at the surface (e.g. liquid moving parallel to the surface with a velocity that varies with depth). Assuming that the scale of turbulence is much greater than the depth of penetration of the solute diffusing at the surface, Danckwerts [1951] created the surface renewal model. The assumptions of this model are that the turbulent flow is a mass of eddies that are incessantly changing their conformations and positions, the part of flow exposed to the surface will receive the solute with the quantity defined by $(\langle c \rangle - \langle c_b \rangle)\sqrt{\frac{D}{\pi t}}$, mean and bulk concentrations are constant in time, the bulk of the liquid contains a uniform concentration of solute and no chemical reactions occur. While previous models only considered molecular diffusion as the main driving mechanism, surface renewal model introduced the role of advection in gas transfer. Considering a liquid which is steadily stirred, such that the mean concentration is constant in time, Danckwerts [1951] stated that once the eddies at the surface are exposed for a definite amount of time to the atmospheric gas, they are replaced by eddies from the bulk of the fluid, with a poorer gas concentration. The mean rate of production of fresh surface is constant and defined as s, which depends on the hydrodynamics and geometry of the system. Starting from surface aging hypotheses (see appendix A.1), Danckwerts [1951] related the mass transfer velocity to the square root of the molecular diffusion multiplied by the mean rate of production of fresh surface (see appendix A.2), as follows:

$$K_L = \sqrt{D\,s}. \tag{2.43}$$

In equation 2.43 the most complicate parameter to define is the renewal time $\tau = 1/s$. Around the same year Fortescue and Pearson [1967] and Banerjee et al. [1968], Lamont and Scott [1970] proposed two different answers to this problem, the former considering the large turbulent structures, while the latter the viscous dissipation scales eddies as the main driving mechanism for mass transfer. Even though, these two equations were validated with experimental results, they link the mass transfer to very different scales of motion. Theofanous et al. [1976] justified this discrepancy, explaining that the data considered for the two studies were representative of small and large Reynolds numbers, respectively, limiting the applicability of the large eddy model by Fortescue and Pearson [1967] to small Reynolds numbers and the small eddy model by Banerjee et al. [1968], Lamont and Scott [1970] to large Reynolds numbers. In subsequent years different attempts were made to directly measure or estimate the renewal time, but it was difficult to unambiguously determine the renewal events[1].

2.2.4.3.1 Large-eddy renewal model Fortescue and Pearson [1967] considered the scenario depicted in Figure 2.4a, where large eddies close to the surface bring the solute rich fluid in the bulk and the fresh liquid from the bulk to the surface (renewal model). No normal velocity is allowed at the flat surface and eddies at the surface are 2D structures ($v = 0$). Mean transfer properties of the eddies can be "modelled by means of a regular sequence of steady square roll

---

[1] "For example, upwellings in open-channel flows could be considered renewal events, but not all appeared to qualify."Tourney and Banerjee [2013].

(a) Sketch of the large eddy surface renewal model.

(b) Sketch of the small eddy surface renewal model.
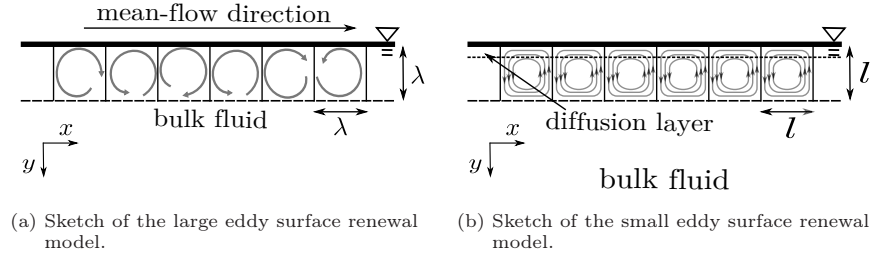
Figure 2.4: Schematic of large and small eddy renewal models. Λ is the length scale of large eddies, while l is the length scale of small eddies.

cells touching the surface, moving as a whole with the local mean surface velocity" [Fortescue and Pearson, 1967]. The authors considered velocity structures to obey only mass conservation equations, but not momentum, since they were not concerned with the dynamic aspects of the flow. The paper considers the large eddies to be prominent at the surface, because the fixed position of the surface, due to gravity, might damp out small eddies, while the lack of turbulent dissipation mechanisms should leave the general eddy pattern similar to the bulk one. In the paper, few experiments are cited where this behavior was found to be coherent with reality, but they also underlined the lack of direct experiments on the topic at the time.

Fortescue and Pearson [1967] considered the integral length scale of the turbulent flow Λ as size of the eddies at the surface (Figure 2.4a):

$$\Lambda = \int_0^\infty \frac{1}{\langle u_r^2(\mathbf{x}) \rangle} \overline{\langle u_r(\mathbf{x}) u_r(\mathbf{x} + \mathbf{r}) \rangle} dr, \qquad (2.44)$$

where u_r is the velocity in the r-direction. The eddies at the surface were considered to be square with a length of Λ. The velocity of the cell is[2]:

$$u = A \, \sin(\frac{\pi x}{\Lambda}) \cos(\frac{\pi y}{\Lambda}), \qquad (2.45)$$

$$v = -A \, \cos(\frac{\pi x}{\Lambda}) \sin(\frac{\pi y}{\Lambda}), \qquad (2.46)$$

where A is a constant that can be found (see appendix A.3) to be:

$$A = 2\sqrt{\frac{1}{2} u^2 + \frac{1}{2} v^2}. \qquad (2.47)$$

The mean mass transfer coefficient is:

$$K_L = -\frac{D}{\Lambda} \int_0^\Lambda \left. \frac{\partial c}{\partial y} \right|_{y=0} dx, \qquad (2.48)$$

obtained resolving the steady mass transfer equation:

$$(\mathbf{u} \cdot \boldsymbol{\nabla}) c = D \nabla^2 c \qquad (2.49)$$

---

[2]   The velocity is considered to be 2D, since the complications added by considering the third component of the velocity would not lead to any improvement to the model in Fortescue and Pearson [1967]' opinion.

with the following boundary conditions:

$$
\begin{aligned}
c(y = 0) &= c_s, \\
\left.\frac{\partial c}{\partial x}\right|_{x=N\Lambda} &= 0 \quad \wedge \quad N \in \mathbb{N}, \\
c(y = \Lambda) &= c_b.
\end{aligned}
\tag{2.50}
$$

Solving numerically equation 2.49 with the imposed boundary conditions (equations 2.50) applied to a 'known' turbulent velocity field[3], Fortescue and Pearson [1967] found:

$$
K_L = 1.46 \sqrt{\frac{D}{\frac{u_{rms}}{\Lambda}}},
\tag{2.51}
$$

where u_{rms} is the root mean square of the streamwise velocity component. Comparing this equation with equation 2.43 and considering that $\tau = 1/s$, in this model:

$$
\tau = \frac{\Lambda}{u_{rms}}.
\tag{2.52}
$$

2.2.4.3.2 Small-eddy renewal model Banerjee et al. [1968]'s objective was to quantify the mass transfer in a falling wavy liquid film in a turbulent flow. The use of an empirical/semi-empirical expression requires a considerable number of experiments with similar set-ups, in order to define the empirical coefficient. The authors discarded this method, because not enough experimental work was performed at that time. Banerjee et al. [1968] decided then to develop a model that attempts to relate the mass transfer rate at some hydrodynamic parameters. The authors considered that, since the small eddies time scale is much shorter than the large eddies one, the mass transfer must be influenced only by small eddies at the surface. These small eddies, swept near the surface by the larger eddies, resides there for a time that is longer than the small eddies time scale. In order for the distance the solute diffuses in the smallest eddy time-scale to be small compared to the length scale of the eddy, the authors considered gases with very low diffusivities (high Schmidt numbers)[4]. Therefore, the thickness of the diffusive layer is much smaller than the length scales of the small eddies at the surface l (see Figure 2.4b). Moreover, the turbulence near the interface is considered to be two-dimensional. The concentration field is described by equation 2.49 and as boundary conditions equations 2.50. Therefore, the mass transfer velocity was found to be:

$$
K_L = 2 \sqrt{\frac{D\,u_1}{\pi\,l}},
\tag{2.53}
$$

providing a renewal rate of:

$$
s = \frac{1}{\tau} = \frac{u_1}{l},
\tag{2.54}
$$

where u_1 is a characteristic velocity scale. Equation 2.53 is expected to hold for a distance $\tilde{H}$ from the interface, such that $\tilde{H}/\sqrt{D\tau} < 0.5$. Considering that, approaching the interface, small eddies kinetic energy is transformed into the configurational energy of the surface, Banerjee

---

[3] The velocity field was generated by inserting square grids made from cylindrical rods at right angles in their experimental set-up.

[4] If τ_η is the small eddy time scale, then the distance the solute diffuses in that time will be $4\sqrt{D\tau}$. The length scale of the smallest eddies in this case is $\sqrt{u_\eta \tau}$. Therefore, the assumption is justified if $1/4\sqrt{u_\eta/D}$ is large, so if the Schmidt number is large enough (≥ 1000).

et al. [1968] computed the distance from the interface, d, over which the small eddies are expected to occur. This is an overestimation of the real value, since the viscous dissipation has been neglected in this computation. They found that, in the wavy liquid film case under analysis, $\tilde{H} > d$ and then equation 2.49 is applicable. Considering that, for Kolmogorov's first hypothesis:

$$l = \eta = \left(\frac{\nu^3}{\epsilon}\right)^{1/4}, \tag{2.55}$$

$$u = u_\eta = (\nu\epsilon)^{1/4}, \tag{2.56}$$

Danckwerts [1951] defined the mass transfer coefficient as:

$$K_L = \sqrt{D}\left(\frac{\epsilon}{\nu}\right)^{1/4}. \tag{2.57}$$

Equation 2.57 is the main results of the small eddy renewal model. It is applicable to turbulent flows with a free interface without external stresses on the surface. In this case the isotropy condition at the surface is no longer valid.

2.2.4.4 Surface divergence model

A completely different approach for gas transfer modelling was attempted by McCready et al. [1986]. Three-dimensional waves of various frequencies and wavelengths present at the surface were neglected, since the model is applicable to high Schmidt numbers scalars. In fact, for low diffusivities the concentration boundary layer is very thin compared to the curvatures imposed by the fluctuating surface. In this case, the surface can be safely approximated as flat. Concentrations and velocity fluctuations were considered to be two-dimensional at the interface and the derivatives of the concentration in the streamwise direction negligible. The governing equation for mass transfer at an interface is:

$$\frac{\partial c}{\partial t} + (\mathbf{u} \cdot \boldsymbol{\nabla})c = \frac{1}{Sc}\nabla^2 c, \tag{2.58}$$

where the terms are normalized with u_τ, ν and $c_s - c_b$. The Taylor expansion of the velocity field in the concentration boundary layer as a function of the distance from the interface is:

$$u = \overline{\langle u(y)\rangle} + \Xi(x, z, t), \tag{2.59}$$

$$v = \beta(x, z, t)y, \tag{2.60}$$

$$w = \gamma(x, z, t), \tag{2.61}$$

where Ξ is the time-varying part of the streamwise velocity gradient, β is the time-varying part of the normal velocity gradient (surface divergence) and γ is the time-varying part of the transverse velocity gradient. This velocity field satisfies the continuity equation.

With the calculations shown in appendix A.4 and considering that $K_L \sim 1/(\delta Sc)$, McCready et al. [1986] found:

$$K_L \sim \sqrt{\frac{\beta_{rms}}{Sc}} \quad \text{for} \quad \frac{\sigma\omega_c}{\omega_m} \text{ large}, \tag{2.62}$$

$$K_L \sim \sqrt{\frac{W_\beta(0)}{Sc}} \quad \text{for} \quad \frac{\sigma\omega_c}{\omega_m} \text{ small}, \tag{2.63}$$

where σ is a shape factor, ω_c is the critical frequency dividing high and low frequency regions and ω_m is the mean frequency (see appendix A.4 for the mathematical expressions). For intermediate values of $\sigma\omega_c/\omega_m$ the mass transfer velocity will depend on both β_{rms} and $W_\beta(0)$.

This model removes the main difficulty of the surface renewal model, the definition of the renewal time τ, replacing it with the unambiguous measurement of the surface divergence. Anyway, the measurement of the surface divergence must be taken very close to the surface and that is why this model has been supported by few experiments until now. In fact, the diffusive boundary layer thickness is very thin and the aforementioned measurements should be taken within ~ 1 mm from the interface. Moreover, in reality, the surface is never flat, but usually there are waves and surfactants that make the analysis of this thin layer very complex. All the experiments that tried to define the coefficient of proportionality of equation 2.62 gave very different results, with variations greater than a factor of three [Turney and Banerjee, 2013].

2.2.4.5 Wind speed parametrizations

Wind-shear acts directly at the interface between gas and liquid, where the resistance of mass exchange is the highest. The main consequence is an enhanced mass transfer. In field experiments, wind speed is an accessible variable compared to mass transfer velocity or small scales flow structures and the mass transfer velocity is usually computed through the wind speed 10 m above the surface. The most important parametrizations in this direction were proposed by Cole and Caraco [1998] and Wanninkhof et al. [2009]. The models proposed by the two studies were developed considering CO_2 in water at $20°C$ ($Sc = 600 - 660$):

$$K_{L,CC1998} = 0.215 U_{10}^{1.7} + 2.07 \ \ \text{[Cole and Caraco, 1998]}, \tag{2.64}$$

$$K_{L,W2009} = 0.1 U_{10} + 0.064 U_{10}^2 + 0.011 U_{10}^3 + 3 \ \ \text{[Wanninkhof et al., 2009]}, \tag{2.65}$$

where U_{10} is the wind velocity 10 m above the water surface. It is clear from these parametrizations that the transfer velocity cannot depend only on the wind speed, because for the condition $U_{10} = 0$, K_L is not null. Mass transfer must be, then, governed also by other processes, e.g. buoyancy flux, heat flux, dissipation, flow divergence, presence of surfactants.

The shear-free boundary condition at the surface (see chapter 3) does not allow to test the applicability of the wind speed parametrizations to the present simulations. This approximation limits the applicability of the present results to very windless conditions, in which the roughness of the surface is negligible.

2.2.5 Film-free and film-covered interfaces

The models presented above are valid for a flat shear-free surface and the mass transfer velocity was found to be proportional to $Sc^{-1/2}$. In experiments, it is hard to demonstrate this behavior, because, for the exponent of the Schmidt number to be equal to $-1/2$, the surface must be perfectly flat and clean. In this sense, the main limitation of experiments is the difficulty of avoiding deposition of particles (e.g. dust) on the surface of the water, during all the sets of experiments. This contamination of the surface changes the boundary condition and, consequently, the aforementioned models are no longer applicable.

For a free surface, the only component of the fluctuating velocity vector that is zero at the surface is v'. When the continuity equation is applied at the surface, the vertical derivative of
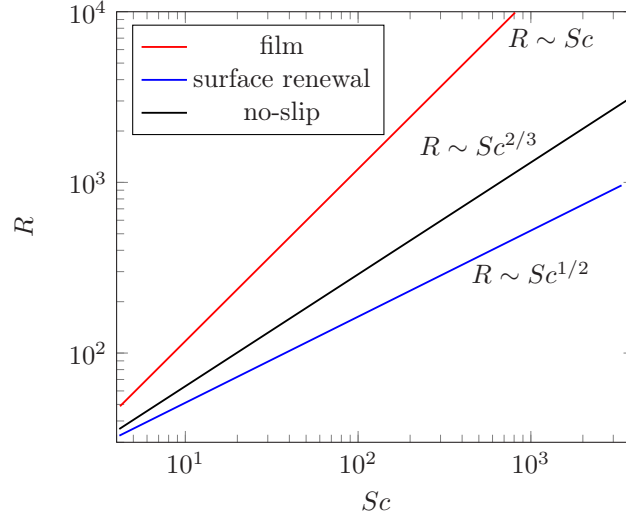
Figure 2.5: Mass transfer resistance as a function of the Schmidt number for the different models. Figure taken from Jähne [1980].

v' reads:

$$\frac{\partial v'}{\partial y} = -\left(\frac{\partial u'}{\partial x} + \frac{\partial w'}{\partial z}\right). \tag{2.66}$$

This equation is valid when the surface is clean and it allows dilation and contraction at the surface.

Surfactants are surface-active chemical agents that generally reduce gas exchange and are an important factor to consider in the analysis of interfacial gas transfer. They are usually present in natural waters and form a film on the surface or a patchy distribution. In this last case the surface tension varies on the surface and it results in elastic forces that attenuates the turbulent eddies. In this way, the gas exchange at the surface is influenced by their presence, particularly for gases with high Schmidt numbers/low diffusivities. The Schmidt number exponent in presence of surfactants on the surface was found to be $-2/3$ by Jähne et al. [1984], Richter and B. [2011]. This large difference in the exponent between clean and polluted surfaces is due to the fact that for a clean surface dilation and contraction of surface elements do not cause restoring forces, since the total area is not changed by the process , while in the case of surfactants there is a film on the surface that behaves like a rigid surface, imposing the 2D continuity equation at the surface. In this last scenario, equation 2.66 imposes that:

$$\frac{\partial v'}{\partial y} = 0, \tag{2.67}$$

changing completely the boundary condition at the surface and, therefore, the exponent of the Schmidt number relation from $-1/2$ to $-2/3$. This means that with the presence of surfactants an increase in the Schmidt number will translate in a mass transfer velocity reduced by a factor of 3 compared to the clean surface case. Figure 2.5 depicts the difference between the film model, where $K_L \propto Sc$ and the renewal models. As can be seen, the presence of surfactants modifies the dependency of the resistance (or mass transfer velocity) and the result lies between these two extreme cases. This is probably why, in the past decades, several experimental studies showed such different exponential dependency of K_L on Sc^{-n}. The different conditions at the surface of each study dictated different exponent n, as well described in Wissink et al. [2017].

The definition of the boundary condition at the surface is much easier in DNS, where it is imposed and, therefore, constant for the whole computation.

2.3 Pollutant transport in open channel flow

This section presents some background of pollutant transport. The first sub-section describes the governing equation, from which, in the second sub-section, the turbulent mixing models in rivers are developed.

2.3.1 Governing equations for pollutant transport

When pollutant transport is considered, a reaction term must be added to equation 2.21:

$$\frac{\partial c}{\partial t} + (\mathbf{u} \cdot \mathbf{\nabla})c = D\nabla^2 c + \mathcal{R}c, \tag{2.68}$$

where $\mathcal{R}$ is the reaction term for the scalar with concentration c. Most practical water quality predictions for rivers rely on a very simplified first-order kinetic model that usually reads:

$$c(t^*) = c(0)e^{-\mathcal{R}t^*}, \tag{2.69}$$

where t^* is a time greater than 0. In this first-order kinetic model, the concentration of pollutant is assumed to decay exponentially with time at a constant rate $\mathcal{R}$, from an initial concentration $c(0)$. The decay rate is usually measured in-situ and it usually spans over several order of magnitude (Thomann and Mueller [1987]). This uncertainty can be explained comparing the complexity of the turbulent environment in which pollutants disperse and the simplicity of the first-order kinetic model. It is clear that, in this kind of models, too many environmental factors are over-simplified and each coefficient developed until today considers only the factors present in that explicit study, hindering the development of a more complex universal model.

The details of the reaction rates chosen for the thesis will be presented in chapter 3.

2.3.2 Turbulent mixing in open channel flow

Mixing is a complex mechanism that is composed by stirring and diffusion. While stirring is a reversible mechanism, diffusion is not and, consequently, mixing is also irreversible. Taylor [1922], assuming a stationary homogeneous flow with a null mean velocity and a source point of pollutant, showed that the growth of the size of the cloud of pollutant for $t \gg T_x$, where T_x is the Lagrangian integral time scale, is time-independent and, in analogy with Fickian diffusion, defined a turbulent diffusion coefficient ϵ_x:

$$2\epsilon_x = \frac{d}{dt}\overline{\langle X_p^2(t) \rangle} = 2\overline{\langle U_p^2 \rangle}T_x, \tag{2.70}$$

where $\overline{\left\langle X_p^2(t) \right\rangle}$ is the spatial mean size of the cloud and U_p is the velocity of points inside the cloud. Here, the analysis is shown in the x-direction, but it is easily extended to the other directions. If the flow is considered to be anisotropic, the turbulent diffusion coefficients are spatially variable and then equation 2.68 becomes:

$$\frac{\partial \overline{\langle c \rangle}}{\partial t} + (\overline{\langle \mathbf{u} \rangle} \cdot \mathbf{\nabla})\overline{\langle c \rangle} = \mathbf{\nabla} \cdot (\boldsymbol{\epsilon}\mathbf{\nabla}\overline{\langle c \rangle}) + \mathcal{R}\overline{\langle c \rangle}, \tag{2.71}$$

where ϵ is different for each direction. In three-dimensions the condition $t \gg T_x$ is replaced with $t \gg T_L$, where $T_L = \frac{1}{3}(T_x + T_y + T_z)$. When the size of the cloud is much greater than the Lagrangian length scale and the scalars perfectly follow the flow $(\overline{\langle U_p^2 \rangle} \simeq \overline{\langle U^2 \rangle})$, the dispersion coefficient becomes[5]:

$$\epsilon_x = l_x \overline{\langle U^2 \rangle}, \tag{2.72}$$

because $l_x \equiv \overline{\langle U_p^2 \rangle} T_x^2$. The turbulent diffusion coefficient is the product of the Lagrangian length scale and the intensity of turbulence.

An open channel flow is a uniform, straight, infinitely-wide channel of constant depth. Since open channel flow satisfies the hypothesis of Taylor's theory, this can be directly applied. The turbulent diffusion coefficient in each direction is then:

$$\epsilon_j \propto H\, u_\tau. \tag{2.73}$$

The diffusion coefficient in vertical direction can be found following the approach used by Elder [1959]. From the definition of the shear stress and the logarithmic law of the wall, the vertical diffusion coefficient reads:

$$\epsilon_y = \kappa y/H(1 - y/H)H\, u_\tau. \tag{2.74}$$

The proportionality coefficient depends on the vertical direction and integrating over the depth of the channel can be theoretically estimated to be:

$$\epsilon_y = 0.067\, H\, u_\tau. \tag{2.75}$$

Csanady [1976] reported:

$$\epsilon_y = 0.05\, H\, u_\tau. \tag{2.76}$$

In the spanwise direction the mixing coefficient is based on several experimental studies [Elder, 1959, Lau and Krishnappan, 1977, Miller and Richardson, 19] and it is usually defined as follows:

$$\epsilon_z = (0.15 \pm 50\%)H\, u_\tau. \tag{2.77}$$

This wide range of values is due to the fact that in reality the coefficient strongly depends on side boundary effects, even for relatively wide systems. When the longitudinal mixing is considered, the analysis becomes much more complex, since it is impossible to distinguish between shear and turbulent dissipation effects. For this reason, the diffusion coefficient in the streamwise direction is not usually measured.

2.4 Previous experimental and numerical studies

The main goal of the aforementioned mass transfer models was to link the averaged mass transfer velocity K_L at the surface with easily measurable flow quantities. During the period in which these conceptual mass transfer models were developed, experimental techniques were improved. Non-intrusive measurements like laser-induced fluorescence (LIF) and particle image velocimetry (PIV) allowed the simultaneous analysis of velocity and concentration fields near the surface. Through the use of these techniques, Herlina and Jirka [2008] and Janzen et al.

---

[5]   Here, shown in x direction only for simplicity.

[2010] were able to directly compute the mass fluxes, for the first time ever in grid-stirred turbulence.

In subsequent years, Komori et al. [1982], Rashidi and Banerjee [1990], Rashidi et al. [1991] proposed different methods to directly measure the characteristic time of surface renewal events, but the lack of an unambiguous definition of the aforementioned event did not allow to clearly define the time scale. Through open channel flow experiments, Moog and Jirka [1999] tested the applicability of the surface renewal models and discovered that both small and large structures collaborate to increase the mass transfer for moderate to high Reynolds number flows. The analysis of their experimental data combined with data from previous literature confirmed the applicability of the small eddy model in open channel flow for $357 \leq Re_\tau \leq 4220$. They explained the dependency of mass transfer on small scales in their "chain saw model", in which the large scale motions transport turbulent energy to the surface, creating active zones for mass transfer. In these regions, mass transfer is controlled by small eddies for all the Reynolds considered in the study. Tamburrino and Gulliver [2002] used flow tracer particles to study surface divergence motions. Unfortunately, the PIV data suffered from flow tracers being too sparse to underline high divergence regions and too dense in convergence motions. Turney and Banerjee [2013] validated the surface divergence model for open channel flow with PIV and three dimensional PIV, concluding that it can accurately predict the mass transfer velocity, but only in windless conditions. Sanjou et al. [2017] modified the surface divergence model, in order to make it independent from the water depth in open channel flow configurations. The experimental focus on the surface divergence model is due to the fact that the surface renewal model relies on quantities that are hardly measurable in real rivers. On the contrary, the application of the surface divergence model requires only the analysis of the surface, which is a summary of the turbulent state below and it is easily accessible.

Several numerical experiments were performed in the same period. The main advantage of DNS compared to experiments is the control of the boundary and flow conditions and the availability of three dimensional fields. Herlina and Wissink [2014] and Herlina and Wissink [2019] performed DNS with Reynolds and Schmidt numbers ranging from 84 to 1856 and 1 to 500, respectively, in a flow driven by isotropic turbulence diffusing from below. These wide ranges allowed to prove the applicability of the two-regime model proposed by Theofanous et al. [1976] to isotropic-driven turbulent flows. Moreover, the concentration and mass fluxes profiles were analyzed, showing that previous experimental results were biased by the contamination of the surface of the tank that e.g. limited the peak of the mean concentration fluctuation and, consequently, hindered interfacial mass transfer.

The analysis of mass transfer in open channel flow through numerical simulations is more complex, since a second boundary layer is imposed by the presence of the bottom wall and the shear makes flow anisotropic. Various studies performed direct numerical simulations of interfacial mass transfer in open channel flow [Handler et al., 1999, Kermani et al., 2011, Nagaosa and Handler, 2003, 2012, Pan and Banerjee, 1995] and most of them focused on the interaction between coherent structures and mass transport, unveiling a strong correlation between vortices ejected from the bottom region and the concentration at the surface. Handler et al. [1999] performed a DNS of open channel flow for $Re_b = 2805$ and $Pr = 2$. They discovered that the thermal structure at the surface is strongly affected by different scalar boundary conditions at the surface and proposed a two-time-scale model. In the model, the scalar boundary layer is strained and compressed by the fast hydrodynamic time-scale, but it is reformed in a longer time linked to the diffusion scale. Through the analysis of cross-correlation, Handler et al.

[1999] proposed hairpin vortices as the dominant structures contributing to the transport of heat in open channel flow. After few years, Nagaosa and Handler [2003] performed a DNS of interfacial mass transfer in open channel flow for $2300 \leq Re_b \leq 5090$ and $Pr = 2$. Surface aligned vortices just below the surface were found to lie underneath high mass transfer regions. The arrangement of this vortices was found to create circular areas of vertical (upwelling and downwelling) motion, which enhanced interfacial mass transfer. These small vortices were found to be originated from hairpin structures that deform into ring-like vortices, as soon as they approach the surface. The hairpin eddies are originated at bottom of the channel and transported upward by Q2-events. This definition of surface event was quantified and its spatial extend was found to be comparable with flow macro length scales. It must be pointed out that the macro scales defined in the paper were extrapolated from the auto-correlation of vorticity and temperature and are still much smaller than the integral length scales computed from the streamwise velocity. Kermani et al. [2011] performed DNS for interfacial mass transfer in open channel flow at $Re_\tau \simeq 300$ and $0.71 \leq Sc \leq 8$. The authors were able to define different scalar transfer stages, using Lagrangian tracing. Nagaosa and Handler [2012], using the data from Nagaosa and Handler [2003] and performing new simulations with $2840 \leq Re_b \leq 11300$, proposed the use of two characteristic time-scales for surface renewal, based respectively on surface divergence and auto-correlation coefficient of the surface divergence divided by velocity fluctuations at the surface. The time-scales were found to be in agreement with previous experimental studies and proportional to $Re_b^{-3/5}$ for the range of Reynolds number considered. Since the Schmidt number considered in the paper was $Sc = 1$, the dependency of mass transfer on the diffusivity was left to future investigations.

The main drawback of DNSs is the excessive computational costs to resolve high Reynolds and Schmidt numbers flows. This is the main reason why, in the past decades, no direct numerical simulations of mass transfer in open channel flow were performed with both moderate/high Schmidt and Reynolds numbers in an adequate domain size. Magnaudet and Calmet [2006] overcame this limit, performing a large eddy simulation (LES), through which they were able to analyze the near surface regions statistics and find that the mass transfer velocity for $Re_\tau = 1280$ and $1 \leq Sc \leq 200$ is proportional to $Sc^{-1/2}$ and $Re^{-1/4}$.

In all the cited DNS studies of mass transfer in open channel flow, the focus was put on the effects of sub-surface flow structures, which are usually very small since the larger structures are suppressed by the presence of the surface. In order to capture these large structures, simulations with adequate domain sizes and moderate Reynolds numbers must be performed. Higher Reynolds numbers were considered in the study of heat transfer in close channel flow by Pirozzoli et al. [2016] and Abe et al. [2018], who performed DNS with Reynolds numbers up to $Re_\tau = 4000$. In close channel flow, $Re_\tau \geq 1000$ is needed, in order for the very large scale motions (VLSM) to have an influence on the turbulence intensities [Álamo et al., 2004, Hoyas and Jiménez, 2006, Moser et al., 1999]. Considering open channel flows, VLSM footprint is already visible for $Re_\tau = 550$ [Wang and Richter, 2019]. In order for such long structures to form, a proper domain size is required. One of the main limitations in the literature of interfacial mass transfer (open channel flow) is the use of small domain sizes that can not consider the influence that VLSM have on the phenomenon. In fact, in order for these structures to develop in an open channel configuration, the domain size must be twice as large in the streamwise and spanwise directions as the one used in close channel configurations, as Bauer et al. [2020] demonstrated.

The limitation on the Schmidt and Reynolds numbers imposed by DNS in the study of interfacial mass transfer in open channel flow hindered the possibility to test the applicability of the aforementioned interfacial mass transfer models for $Sc > 8$ and $Re_\tau > 600$. An increase in the Schmidt number translates directly into thinner filaments with very sharp concentration gradients, for which the resolution of the small scales becomes fundamental. In order to fill this gap, in the present thesis, scalar fields from $Sc = 4$ to $Sc = 200$ are resolved. At the same time, Reynolds numbers up to $Re_\tau = 630$ were employed to determine the role of different scales of motion on interfacial mass transfer for different turbulent levels and diffusivities. Moreover, a range of domain sizes was employed to check if the results from previous studies were biased by this choice.

3 Methodology

This chapter presents an overview of the finite-difference direct numerical simulation technique employed for the thesis. The DNSs were performed with the KCFlo in-house code developed by Kubrak et al. [2013], in order to resolve interfacial mass transfer for gases with low diffusivities. Since the difference between momentum and molecular diffusivities is very large for low diffusivities gases, the code employs a dual mesh approach, where the velocity field is solved on a base mesh, while the scalar fields are solved using a finer grid. The code was vastly used to analyze mass transfer across a flat surface, driven by isotropic turbulence diffusing from below (Herlina and Wissink [2014, 2019], Wissink et al. [2017]) and buoyant convection (Wissink and Herlina [2016]).

The chapter has been structured in four main sections. In the first section, the mathematical formulation describing the problems tackled in the thesis is presented. The second section depicts the characteristics of the computational setup, while the third section contains a description of the schemes implemented in the code. The last part of this section shows the efficiency of the code resolving scalar transport.

3.1 Governing equations

The problems under consideration are gas transfer and pollutant transport in a turbulent open channel flow. The mathematical system employed to describe these processes consists of the three-dimensional incompressible Navier-Stokes equations and advection-diffusion-reaction equations that model the scalars (e.g. gas, bacteria and heat) behavior. The complete mathematical formulation is:

$$\frac{\partial \mathbf{u}}{\partial t} + (\mathbf{u} \cdot \nabla)\mathbf{u} + \frac{1}{\rho_f}\nabla p = \nu\nabla^2\mathbf{u} + f_b + \boldsymbol{f}, \tag{3.1}$$

$$\nabla \cdot \mathbf{u} = 0, \tag{3.2}$$

$$\frac{\partial c_i}{\partial t} + (\mathbf{u} \cdot \nabla)c_i = D_i\nabla^2 c_i - \mathcal{R}_i c_i, \tag{3.3}$$

$$\frac{\partial T}{\partial t} + (\mathbf{u} \cdot \nabla)T = k_T\nabla^2 T. \tag{3.4}$$

In equations (3.1) to (3.4), c_i is the scalar concentration, D_i the diffusion of the dissolved scalar, $\mathcal{R}_i$ the reaction term, T the temperature field and k_T the thermal diffusivity. Equation 3.3 is the equation of the scalar that changes for each case considered in the thesis.

When mass transfer was considered, the advection-diffusion equation was resolved for the gas and reads:

$$\frac{\partial c_g}{\partial t} + (\mathbf{u} \cdot \nabla)c_g = D_g\nabla^2 c_g, \tag{3.5}$$

where the subscripts $*_g$ refers to the gas under consideration.

If pollutant transport was simulated, two advection-diffusion-reaction equations were solved by the code, one for bacteria and one for the gas:

$$\frac{\partial c_B}{\partial t} + (\mathbf{u} \cdot \nabla)c_B = D_B \nabla^2 c_B - \mathcal{R}_B \, c_B, \tag{3.6}$$

$$\frac{\partial c_{O_2}}{\partial t} + (\mathbf{u} \cdot \nabla)c_{O_2} = D_{O_2} \nabla^2 c_{O_2} - \mathcal{R}_{O_2} \, c_{O_2}, \tag{3.7}$$

where the subscripts $*_B$ and $*_{O_2}$ refer to bacteria and oxygen, respectively. The decay rates of bacteria and oxygen are bounded to the temperature. A change in this parameter modifies the reaction rates. For the present thesis, all the parameters were tuned on a temperature of $20°\,C$. $\mathcal{R}_B$ is the total decay rate of bacteria, which, in the present simulations, is composed by the UV-inactivation rate $\mathcal{R}_{UV}$, the bacterial natural die-off rate $\mathcal{R}_{nat}$ and the decay rate due to the higher metabolism induced by aerobic conditions $\mathcal{R}_G$, such that $\mathcal{R}_B = \mathcal{R}_{UV} + \mathcal{R}_{nat} + \mathcal{R}_G$. $\mathcal{R}_G$ depends on the oxygen concentration level available in the fluid, while the oxygen consumption rate $\mathcal{R}_{O_2}$ depends on the amount of bacteria present. The bacterial inactivation rate due to sunlight, $\mathcal{R}_{UV}$, is proportional to the product of the UV irradiance I_y and a UV sensitivity coefficient α_{UV}:

$$\mathcal{R}_{UV} = \alpha_{UV} I_y, \tag{3.8}$$

where I_y at a certain depth y (measured from the water surface) is usually described by the Lambert-Beer law:

$$I_y = I_0 e^{-k_{att} y}, \tag{3.9}$$

such that:

$$\mathcal{R}_{UV} = \alpha I_0 e^{-k_{att} y}, \tag{3.10}$$

where I_0 is the average surface UV irradiance and k_{att} is an attenuation factor. In all the simulations, we considered $\alpha I_0 = 0.00029\,s^{-1}$, $k_{att} = 1.998\,m^{-1}$, $\mathcal{R}_G = 9.8 \cdot 10^{-5}\frac{c_G}{3+c_G}\,s^{-1}$ and $\mathcal{R}_{nat} = 8.33 \cdot 10^{-6}\,s^{-1}$. The UV E. Coli sensitivity coefficient was estimated considering the decay rates of bacteria for UV irradiancies of $40\ W/m^2$ to be 0.08. The oxygen decay rate due to bacterial metabolism was chosen to be $\mathcal{R}_{O_2} = 4.63 \cdot 10^{-8}\frac{c_B}{2000\,MPN}s^{-1}$, where MPN is the most probable number of bacteria. These values were computed from the results of Garcia-Armisen and Servais [2009], Roslev et al. [2004], Schultz-Fademrecht et al. [2008], Sinton et al. [2002], Tchobanoglous et al. [2003] by the Engler-Bunte-Institute (EBI) of KIT. In all the simulations performed the re-growth rate of bacteria has always been considered to be null, since the analysis was focused on the self-purification processes happening in the first minutes of contact with water, when the bacteria are still in a lag state, due to the change of environment.

3.2 Computational setup

The computational setup is shown in figure 3.1. The numerical domain is defined by lengths L_x, L_y and L_z in streamwise (x), vertical (y) and spanwise (z) directions, respectively. The chosen domains are $3H \times H \times 3H$, $12H \times H \times 3H$ and $24H \times H \times 6H$, where H is the height of the open channel. A free-slip boundary condition at the top ($y/H = 1$) and a no-slip boundary condition at the bottom ($y/H = 0$) of the channel are applied for the velocity field, while periodic boundary conditions are employed in streamwise and spanwise directions. Every movement of the free-slip surface was neglected, which corresponds to zero Froude and Weber numbers.
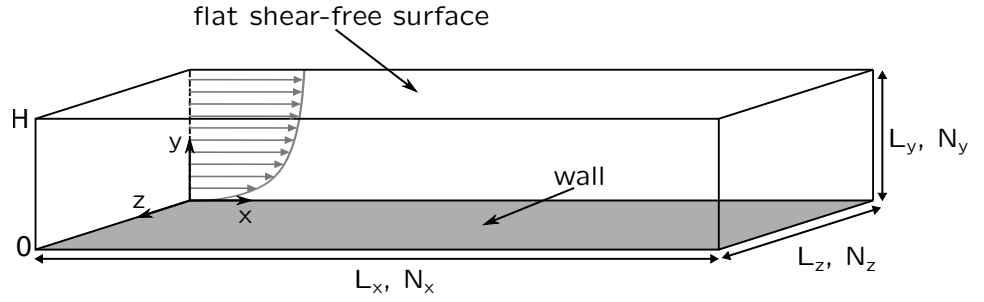
Figure 3.1: Computational geometry and coordinate system for open channel flow.

Therefore, the surface is considered to be flat, such that every influence waves can have on mass transport is neglected in the simulations. The boundary conditions employed for the scalars in the mass transfer simulations in the vertical directions are a Dirichlet boundary condition at the surface (c at saturation), modeling the atmosphere, and a Neumann boundary condition at the bottom of the channel. In the case of pollutant transport, a different boundary condition must be implemented at the surface, since the bacteria are not perpetually replaced at the interface between gas and liquid. For this reason, a Neumann boundary condition was imposed at the top of the channel. In all the scalar simulations, periodic boundary conditions were implemented in the homogeneous directions x and z. A detailed description of the implementation of the aforementioned boundary conditions in the code can be found in Kubrak et al. [2013].

The spatial discretization of the fluid flow was performed on a non-uniform Cartesian mesh using a staggered variable arrangement, where the pressure and scalar concentrations were defined in the center of the grid cells. The mesh was uniform in the homogeneous (x, z) directions and stretched in the vertical (y) direction to obtain finer meshes near the upper and lower boundaries with the following function:

$$y(j) = \left(1 - \frac{\tanh(y_\phi)}{\tanh(y_1)}\right)\frac{y(0)}{2} + \left(1 + \frac{\tanh(y_\phi)}{\tanh(y_1)}\right)\frac{y(n_y)}{2} \tag{3.11}$$

for $i = 1, ..., n_y$ (n_y =number of grid points in vertical direction), with:

$$y_1 = \frac{\delta}{2}, \tag{3.12}$$

$$y_\phi = \delta\left(\frac{j}{n_y} - 0.5\right), \tag{3.13}$$

$$\delta = \frac{j}{n_y}\sigma_t + \left(1 - \frac{j}{n_y}\right)\sigma_b, \tag{3.14}$$

where σ_t and σ_b are the parameters controlling the stretching at the top and at the bottom of the channel, respectively. They were chose to be $\sigma_b = 2$ and $\sigma_t = 2$ for the smallest, $\sigma_b = 2$ and $\sigma_t = 3$ for the mid and $\sigma_b = 2.3$ and $\sigma_t = 3$ for the largest domain size simulations. The stretching in the vertical direction allows to accurately resolve the fine scales produced by velocity and scalars fields in the boundary regions in a very efficient manner.
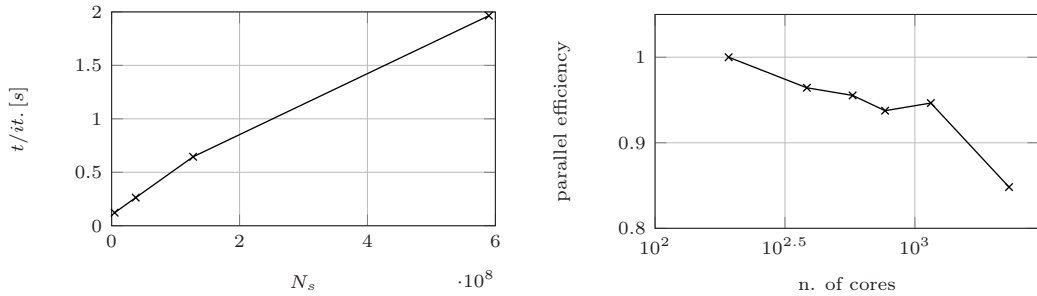
(a) Scaling of the execution time per iteration as a function of the total number of grid points of the scalar mesh N_s. This test was performed with the flow solved on the coarse mesh and one scalar on a refined mesh with a refinement factor f_R from 1 to 4. The number of cores is 144 in all simulations.

(b) Weak scaling with flow field resolved on the coarse mesh and three scalars ($Sc = 7$, 16 and 100) on the refined one, with refinement factors of $f_R^x, f_R^y, f_R^z = [6, 2, 2]$. The local grid size per core was $48 \times 96 \times 48$.

Figure 3.2: Tests of code performances.

3.3 Numerical method

The full set of governing equations was solved using the in-house KCFlo code [Kubrak et al., 2013]. The flow field was solved using a fourth-order central discretization of the diffusion combined with a fourth-order kinetic energy conserving discretization of the convection [Wissink, 2004]. The Poisson equation for the pressure was solved using a conjugate gradient solver, with simple diagonal preconditioning. The scalar advection-diffusion equations were discretized using a fifth-order weighted essentially non-oscillatory (WENO) scheme [Liu et al., 1994] for the scalar convection and a fourth-order accurate central scheme for the diffusion. The details of the discretization of flow and scalars equations are reported in Kubrak et al. [2013].

The solutions of both flow and scalar fields were advanced in time using the second-order accurate explicit Adams-Bashforth scheme. Up to five scalar advection-diffusion equations with different Schmidt numbers were solved simultaneously, enabling a direct comparison of scalar transport processes driven by exactly the same background turbulence.

In every simulation, a dual-mesh approach is employed, in order to consider the increase in the ratio between momentum and scalar diffusivity due to the decrease of D. This difference translates in the necessity to employ a much finer mesh to accurately resolve the low diffusivity scalar field compared to the coarser mesh required by the flow field in an efficient manner. In fact, scalar diffusivity can be up to three order of magnitude smaller than momentum diffusivity when $Sc = \mathcal{O}(10^2)$ are considered.

Note that the implementation of two grids made the interpolation of the different variables necessary, in order to compute the convective transport. In fact, the velocities are interpolated onto a sub-grid using a fourth-order Lagrange interpolation. Depending on the chosen refinement factor for the finer grid, an interpolation is necessary, in order to compute scalars and velocity quantities in the same sub-cell. When the refinement factor is chosen to be equal to 3, this interpolation is not necessary, since some velocities and the central sub-cell of the scalar are defined at the same location. The effectiveness and convergence of the dual-mesh approach was demonstrated in Herlina and Wissink [2014], Kubrak et al. [2013], Wissink and Herlina [2016].

The direct numerical simulations were performed on ForHLRII, bwUniClusterI and bwUniClusterII at the Steinbuch Centre for Computing (SCC) at KIT. Several tests were performed on ForHLRII, in order to determine the code performance in open channel flow configuration on the aforementioned supercomputer. Figure 3.2a shows the time per iteration for a test in which

the flow is solved on a coarse mesh and one scalar on a refined mesh with refinement factors f_R spanning from 1 to 4. 144 cores are employed for each simulation. The weak scaling is shown in figure 3.2b. In this case, three scalars were resolved on a finer mesh, with different refinement factors for each direction $f_R^x, f_R^y, f_R^z = [6, 2, 2]$. The local grid size per core was $48 \times 96 \times 48$. The noticeable decrease in the parallel efficiency for the largest number of cores employed is mainly due to communication. Note that the number of operations per time-step was found to be mainly dependent on the refinement factor f_R, as $O(f_R^3 N_f)$, where N_f is the total number of grid points in the flow field coarse mesh. Therefore, when using a refined scalar mesh, the solver of the scalar convection-diffusion equation dominates the total computing time.

4 Turbulent flow fields

The scalar (e.g. bacteria and gas) transport simulations presented in chapters 5 and 6 were started from fully developed turbulent flows. These were prepared by starting from a coarser mesh turbulent flow field interpolated to the desired mesh. On average around 50 bulk time units were required for the flow statistics to converge. The time windows chosen for each simulation are shown in table 4.1. The values averaged on the homogeneous planes x, z are represented by $\langle \cdot \rangle$, while the values averaged in time are represented by $\bar{\cdot}$. $\cdot^+$ represents averaged data normalized with viscous scales.

In this chapter, the statistics of the flow fields are presented. The chapter is divided in three main sections. In the first chapter, the two-point correlation and the 1D energy spectra of the streamwise velocity component were analyzed to evaluate the adequacy of the chosen domain sizes and grid resolutions. In the second section, the most important turbulent statistics are analyzed and compared with previous literature. A discussion of the presence of large and very large scale motions in the largest domain size considered and their interaction with small scale motions closes the chapter.[1]

4.1 Domain sizes and grid spacing

The flow parameters chosen for each simulation are shown in table 4.1. In order to verify the ability of the domain size to capture the largest scale of motions and the adequacy of the grid spacing to resolve the smallest Kolmogorov scales, two-point correlation and the 1D energy spectra of the streamwise velocity component were analyzed for all the simulations.

Before proceeding with the discussion of the results, a brief overview of the effect of the domain size on the flow structures in open channel flow is presented. A more detailed investigation can

---

[1] Part of the results reported in this chapter were also presented in Pinelli et al. [2022].

Case	Re_b	Re_τ	$L_x \times L_y \times L_z$	$N_x \times N_y \times N_z$	$\Delta t/t_b$	Δt^+	line
F01	3000	190	$3H \times H \times 3H$	$192 \times 128 \times 192$	360	4332	——
F02	4000	240	$3H \times H \times 3H$	$192 \times 128 \times 192$	260	3744	- - -
F03	5000	290	$3H \times H \times 3H$	$192 \times 128 \times 192$	380	6390	⋯⋯
F04	2875	180	$12H \times H \times 3H$	$384 \times 128 \times 192$	700	7900	——
F05	4000	240	$12H \times H \times 3H$	$384 \times 128 \times 192$	252	3630	- - -
F06	5000	290	$12H \times H \times 3H$	$384 \times 128 \times 192$	340	5720	⋯⋯
F07	3200	200	$24H \times H \times 6H$	$1152 \times 384 \times 1152$	120	1500	——
F08	6300	365	$24H \times H \times 6H$	$1152 \times 384 \times 1152$	80	1665	- - -
F09	12000	630	$24H \times H \times 6H$	$1152 \times 384 \times 1152$	100	3300	⋯⋯

Table 4.1: Computational parameters of flow simulations. Re_b is the bulk Reynolds number, Re_τ is the friction Reynolds number, L_x, L_y and L_z denote the size of the domain, H is the height of the domain, N_x, N_y and N_z are the number of grid points in x, y, z directions respectively, $\Delta t/t_b$ and Δt^+ are the time window over which the averaging is performed normalized with bulk time units and viscous scales, respectively.

(a) F03: $Re_\tau = 290$.

(b) F05: $Re_\tau = 290$.

(c) F09: $Re_\tau = 630$.
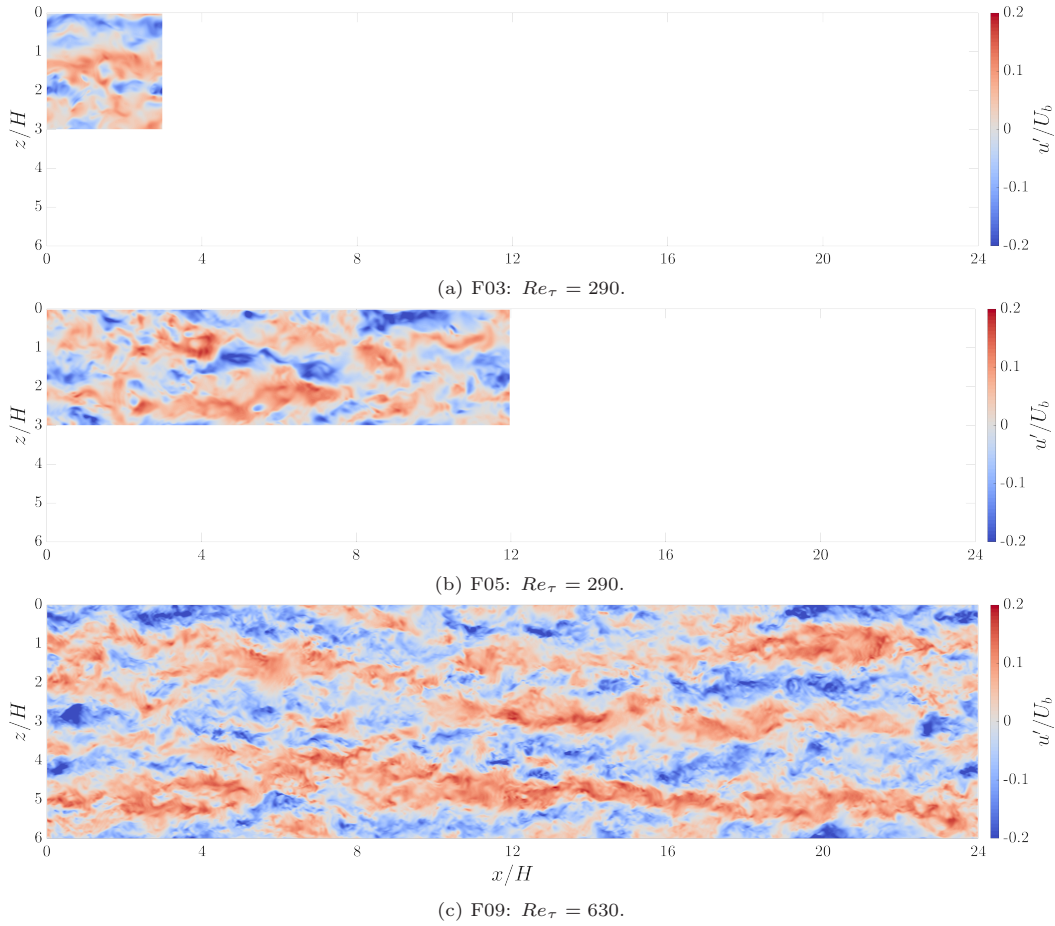
Figure 4.1: Instantaneous contour maps of u'/U_b in the plane $y/H = 0.6$ for simulations F03, F06 and F09.

be found in e.g. Bauer et al. [2020], Wang et al. [2020], while similar investigations for closed channel flow were carried out by e.g. Abe et al. [2018], Feldmann et al. [2018], Hwang and Cossu [2010], Lozano-Durán and Jiménez [2014].

One of the main findings reported in the investigations mentioned above is the appearance of very large coherent structures for large Re_τ. To assess the suitability of the domain sizes used in the present simulations for capturing such large coherent structures, typical snapshots of the streamwise velocity fluctuations u' at $y/H = 0.6$ for F03, F06, F09 are shown in figures 4.1. As can be seen in table 4.1, these cases have the highest Re_τ for each of the three domain sizes considered. In all figures, high and low velocity elongated streaky structures, which are characteristic of open channel flow, can be seen. The snapshots indicate that the streamwise extent of these coherent structures was captured quite well in the largest domain, but not in the smallest and mid domains. Furthermore, in figure 4.1c a coherent structure of length $\approx 20H$ can be observed. In the literature, structures of length $\gtrsim 10H$ are usually referred to as very large scale motions (VLSM) [Álamo et al., 2004, Del Álamo and Jiménez, 2003, Jiménez, 2012, Kim and Adrian, 1999], while the term large scale motions (LSM) is typically used for structures with a length of $\approx 1-3H$ [Balakumar and Adrian, 2007, Hutchins and Marusic, 2007, Kim and Adrian, 1999]. In open channel flow, the onset of the appearance of VLSM is still uncertain, i.e. to date such motions were confirmed to appear for $Re_\tau \geq 400$ [Bauer et al., 2020], $Re_\tau \geq 550$ [Wang and Richter, 2019] and experimentally at $Re_\tau \geq 700$ [Peruzzi et al., 2020]. The very large coherent structure seen in figure 4.1c is an example of such a very large scale motion that

(a) $y/H = 0.9956$ (F01, F02 and F03), $y/H = 0.9975$ (F04, F05 and F06) and $y/H = 0.9997$ (F07, F08 and F09).

(b) $y^+ \simeq 4.5$.
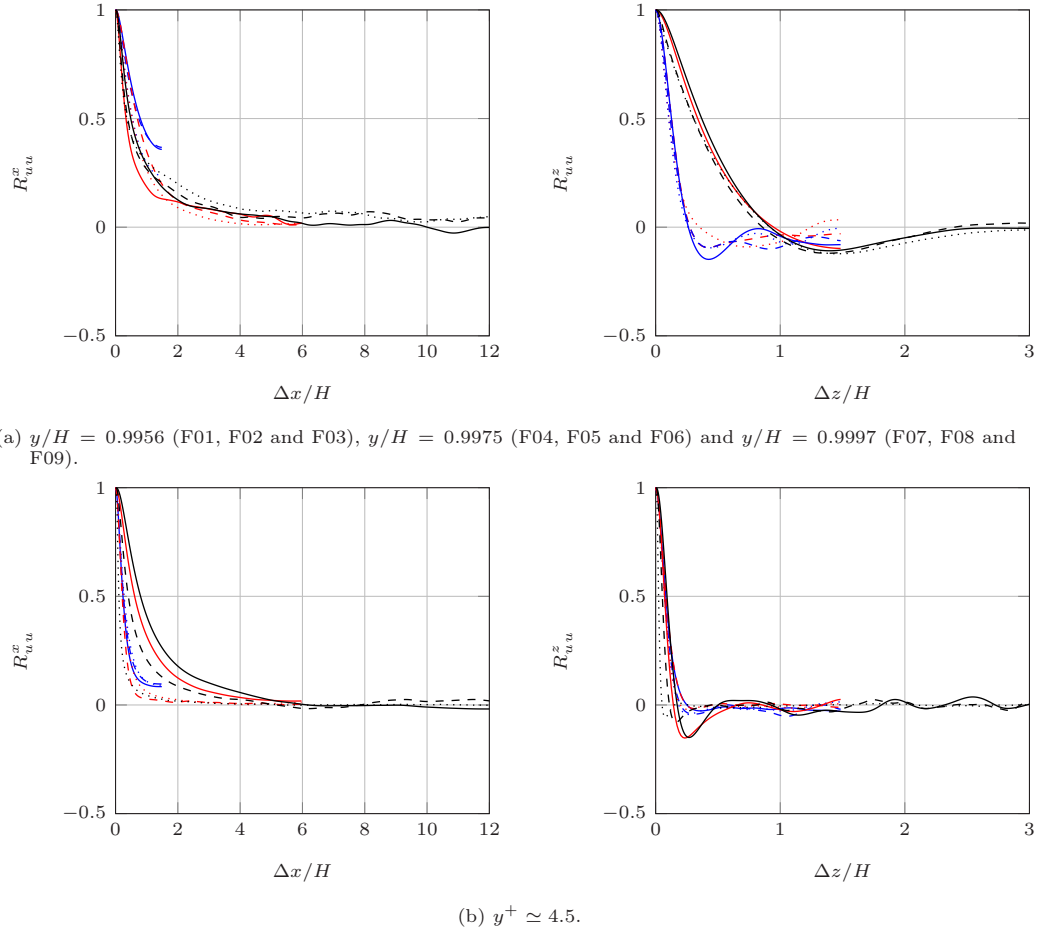
Figure 4.2: Two-point correlation for the streamwise velocity u' in streamwise x and spanwise z direction.

is found at $Re_\tau = 630$. Later, it will be shown that in the present simulations VLSM could already be detected at $Re_\tau = 365$. Further confirmations of the appearance of VLSM based on e.g. pre-multiplied spectra and velocity fluctuations analyses, is presented in the next sections.

The averaged two-point, one-time auto-covariance, from now on referred to as the two-point correlation, of a random field Ω is given by:

$$R^{\boldsymbol{x}}_{\Omega'_i \Omega'_j}(\boldsymbol{r}) = \overline{\left(\frac{\langle \Omega'_i(\boldsymbol{x},t) \Omega'_j(\boldsymbol{x}+\boldsymbol{r},t) \rangle}{\langle \Omega'_i(\boldsymbol{x},t) \Omega'_j(\boldsymbol{x},t) \rangle} \right)}, \tag{4.1}$$

where $\mathbf{r}$ is the separation vector between the two points. The two-point correlations for all the velocity components were evaluated in the homogeneous directions for different distances from the wall. Figure 4.2 depicts the two-point correlation of the streamwise velocity in streamwise and spanwise directions for all the simulations performed close to the wall $y^+ \simeq 4.5$ and near the surface $y/H \simeq 1$. Figure 4.2a shows that for both $Re_\tau = 365$ and 630, the proper de-correlation of u' in the largest domain (shown for $y/H = 0.9997$ in figure) was achieved in the spanwise direction for all y/H, but not in the streamwise direction. For $y/H > 0.7$ the minimum value for the streamwise R_{uu} was always smaller than 0.05, indicating a more marginal de-correlation. Even if the values for high separations are very low, correlation of the streamwise velocity component in streamwise direction shows that a larger domain size needs to be employed to achieve de-correlation. The positive side on using a slightly smaller domain size is that it

(a) $y/H = 0.1$.

(b) $y/H = 0.9$.
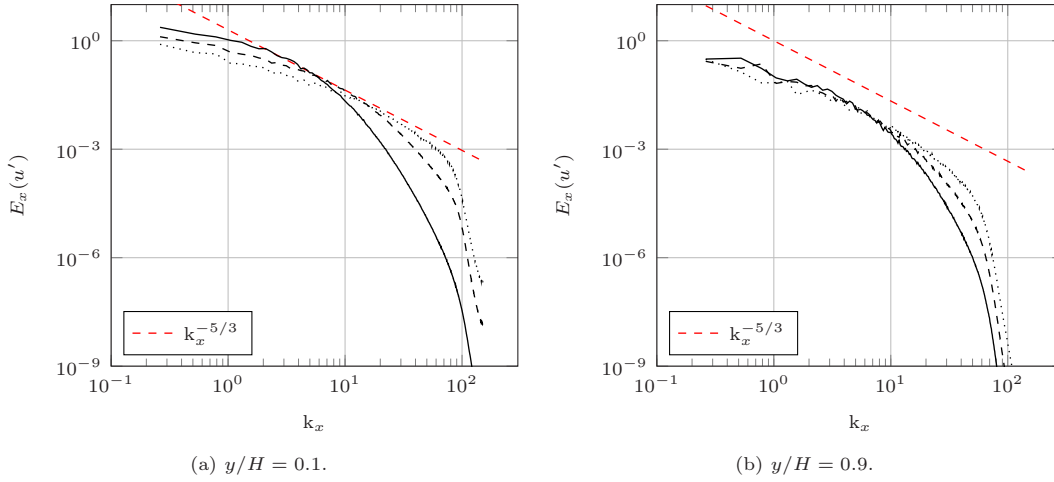
Figure 4.3: One-dimensional energy spectra for simulations F07, F08 and F09 in streamwise direction close to the surface ($y/H = 0.9$) and to the wall ($y/H = 0.1$).

hindered the meandering of these structures, allowing an easier analysis of their influence on mass transfer (see Chapter 5). For the simulation with the largest domain size and the lowest $Re_\tau = 200$, a de-correlation of u' in both horizontal directions was obtained for the entire depth. In the mid-sized simulations, the streamwise de-correlation was marginal for all cases, while in the smallest domain no de-correlation was achieved at any height (see figure 4.2b). Therefore, a domain size of $3H \times 3H \times H$ is too small to fully capture turbulent open channel flow, even for Re_τ as low as 190. The three simulations with the largest domain sizes are considered the only simulations in which the chosen domain size demonstrates to be adequate to capture both large and very large scale motions.

In homogeneous turbulence, the Fourier space representation of the two-point correlation is the spectrum tensor, defined as:

$$\Phi^{\mathbf{k}}_{\Omega_i \Omega_j}(\mathbf{k}, t) = \frac{1}{(2\pi)^3} \iiint_{-\infty}^{\infty} R^{\mathbf{r}}_{\Omega_i \Omega_j} e^{-i\mathbf{k}\cdot\mathbf{r}} d\mathbf{r}, \tag{4.2}$$

where $\mathbf{k} = (\mathrm{k}_x, \mathrm{k}_y, \mathrm{k}_z)$ is the continuous wavenumber vector. The energy spectrum function is obtained by removing all the directional information from $\Phi_{ij}(\mathbf{k})$ and it is defined as:

$$E(\mathrm{k}, t) = \iiint_{-\infty}^{\infty} \frac{1}{2} \Phi^{\mathbf{k}}_{\Omega_i \Omega_i}(\mathbf{k}, t) \delta(|\mathbf{k}| - \mathrm{k}) d\mathbf{k}, \tag{4.3}$$

where k is here independent from $\mathbf{k}$. The one-dimensional streamwise energy spectra of the velocity components for the simulations with the largest domain size (F07, F08 and F09) is shown in figure 4.3. As also observed for all other simulations, no energy pile-up at high wavenumbers was observed, demonstrating that the smallest scales of motion were well resolved. Furthermore, the existence of an inertial sub-range, indicated by the $\mathrm{k}^{-5/3}$ power law, can be clearly seen. All the simulations showed similar behaviors across the vertical direction, but only the simulations with the largest domain size are shown.

4.2 Turbulent statistics

This section presents the analysis of the main flow field statistics. In the first sub-section, the total shear stress was found to be linearly dependent on the height of the channel for all
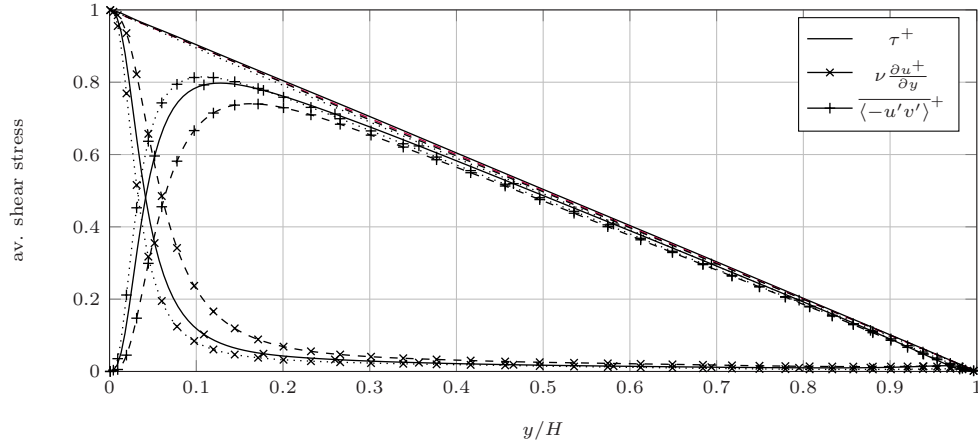
Figure 4.4: Total $\tau^+ = \frac{\langle\tau\rangle}{u_\tau^2}$, viscous $\nu\frac{\partial u^+}{\partial y}$ and turbulent $\overline{\langle -u'v'\rangle}^+$ shear stress for simulations —— F07, - - - F08 and ⋯⋯ F09.

	F01	F02	F03	F04	F05	F06	F07	F08	F09
κ	0.4795	0.4199	0.4301	0.3891	0.3924	0.3918	0.3933	0.3909	0.3798
B	7.6201	6.3537	6.5720	5.5159	5.4220	5.4887	5.3869	5.2819	4.8371

Table 4.2: Constants of the log law $u^+ = \frac{1}{\kappa}y^+ + B$ computed by linear regression for $y^+ > 30$ and $y/H < 0.7$.

the simulations performed. In the second sub-section, the law of the wall approximated well the mean velocity profiles of every simulation. The third sub-section analyzes the influence of turbulent intensity and domain size on the velocity fluctuations, while the last sub-section shows that the turbulent kinetic energy equation is fulfilled for all the simulations. In addition, it was found that $Re_\tau = 0.166Re_b^{0.88}$, which is in agreement with e.g. Bauer et al. [2020], Lee and Moser [2015], Pope [2000].

4.2.1 Shear stress

Figure 4.4 depicts the total shear stress $\tau^+ = \frac{\langle\tau\rangle}{u_\tau^2}$ and its viscous $\nu\frac{\partial u^+}{\partial y}$ and turbulent $-\overline{\langle u'v'\rangle}^+$ components for the simulations performed on the largest domain size. The viscous stress dominates at the wall, while the Reynolds stress becomes important in the bulk and at the top of the channel. As the Reynolds number increases, the height at which the turbulent stress becomes larger than its laminar counterpart decreases, underlying the necessity to employ a much finer grid when higher levels of turbulence are considered. The linearity of the total shear stress indicates that the flow is statistically stationary and confirms that the chosen number of time and space samples is sufficient to reach reliable one-point statistics. Only the simulations performed on the largest domain size are shown, since they are considered to be the most problematic cases. The shear stresses for all the simulations are shown in appendix A.5.

4.2.2 Mean streamwise velocity profile

A logarithmic plot of the mean velocity profile as function of wall units is shown in figure 4.5. u^+ was found to be linearly dependent on the wall units for $y^+ \leq 5$, in agreement with Pope [2000]. The figure confirms that the viscous sub-layer thickness does not depend on the Reynolds number when the vertical dimension is normalized with viscous scales. Further away from the
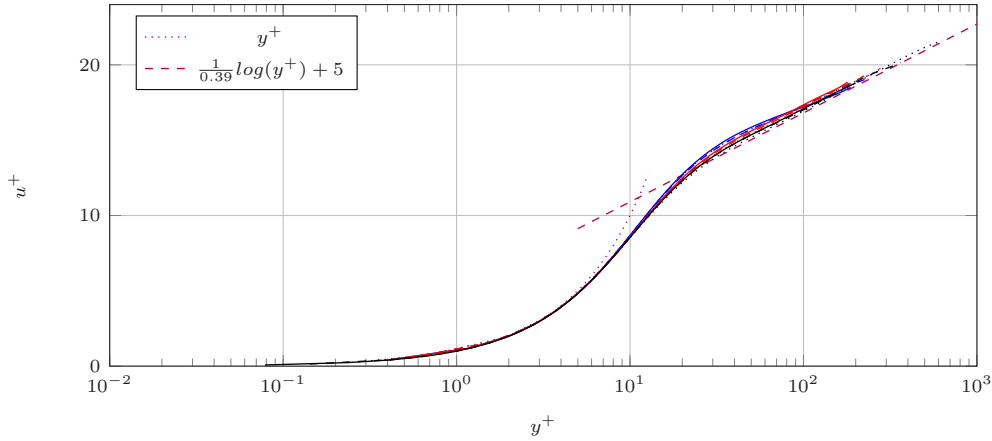
Figure 4.5: Law of the wall applied to the results of all the simulations performed.

wall, the dependency of u^+ on the viscosity becomes weaker and a buffer layer between the viscous sub-layer and the logarithmic region is reached for all the simulations performed at $5 \leq y^+ \leq 30$. The logarithmic law of the wall introduced by von Karman [1930]:

$$u^+ = \frac{1}{\kappa} ln\, y^+ + B, \tag{4.4}$$

was found to be applicable to all the simulations for $y^+ \geq 30$ and $y/H < 0.7$, with the values of κ and B listed in table 4.2. The variation of the values looks quite large, but it is mostly due to the choice of the range for the curve fitting that is somewhat arbitrary, as well explained by Lee and Moser [2015]. Moreover, an analysis of the indicator function $y^+ \partial u^+ / \partial y^+$ showed that the results obtained from the small domain-sized simulations suffer from statistical noise, which makes the definition of these constants quite arbitrary, as confirmed by Lee and Moser [2015] for their simulation with domain size $2\pi H \times H \times \pi H$. Figure 4.5 shows that all the plots can be well modelled by the logarithmic law of the wall with parameters $\kappa = 0.39$ and $B = 5$, which are widely accepted values for wall-bounded flows.

4.2.3 Velocity fluctuations

Figure 4.6a depicts the open channel turbulence intensities normalized by u_τ in the region $y^+ \leq 120$. The peak of the rms of the streamwise velocity component is located at $y^+ \simeq 15$ for all the domain size and Reynolds numbers employed. The values of the peak of u_{rms}^+ vary from one domain size to the other and they span from 2.7 to 3. An increase in the Reynolds number determines an increase in the value of the streamwise velocity fluctuation peak, when the same domain size is consider. The position of the peaks $y^+ \simeq 15$ and their values were found to fall in the range provided by previous literature [Kim et al., 1987, Pope, 2000, Wang and Richter, 2019]. The simulations performed with the smallest domain size showed higher values of the velocity fluctuations in the streamwise direction and smaller values for v_{rms} and w_{rms}, in agreement with the findings of Abe et al. [2018], Lee and Moser [2015]. Abe et al. [2018] explained this behavior with a weakened energy redistribution between the velocity fluctuations, due to lower energy fluxes present in domain sizes with $L_x < 6.4H$. Since the velocity fluctuations of the simulations performed on the smallest domain size are known to be biased, they will not be taken into account in the following analysis.
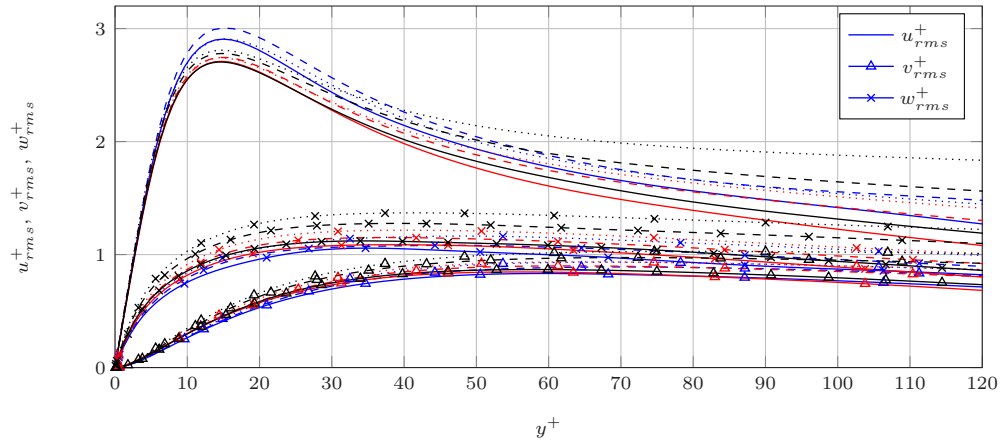
(a) Velocity fluctuations and vertical direction normalized with friction velocity and near-surface viscous length scale, respectively.
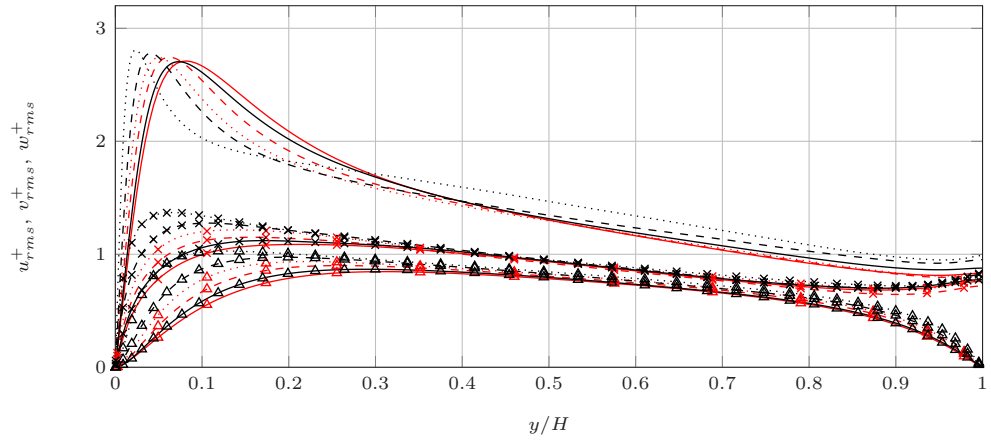
(b) Velocity fluctuations and vertical direction normalized with friction velocity and height of the channel, respectively.

Figure 4.6: Velocity fluctuation as a function of the vertical direction for all the simulations performed.
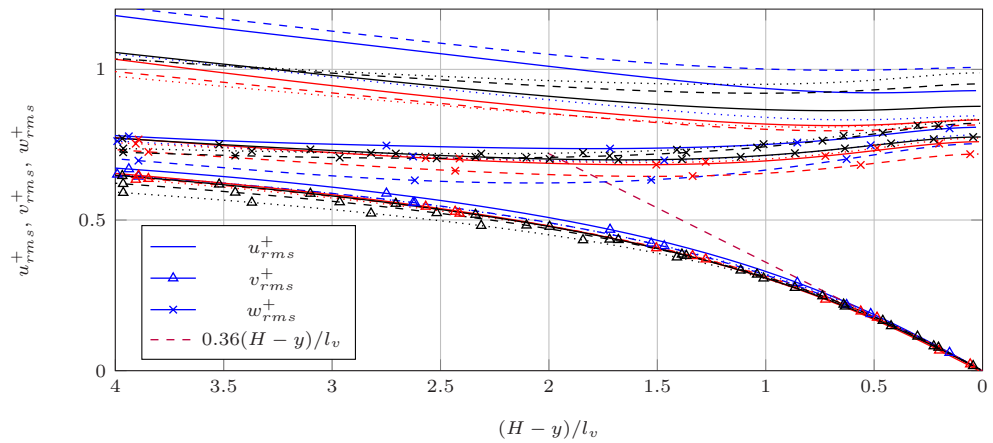
Figure 4.7: Velocity fluctuation as a function of the vertical direction normalized with the near-surface viscous scale l_v for all the simulations performed. All v_{rms}^+ have linear behavior for $(H - y)/l_v \leq 0.6$ with a constant of proportionality equal to 0.36.

Figure 4.6b depicts the velocity fluctuations normalized with the friction velocity as a function of the vertical direction y/H. The streamwise velocity fluctuations for $Re_\tau \geq 365$ showed higher values compared to the other simulations, which almost collapse on the same curve. In wall-bounded flows, this increase is usually associated to the presence of VLSM, which become more energetic when the Reynolds number is increased [Álamo et al., 2004, Hoyas and Jiménez, 2006, Kim and Adrian, 1999]. In the present simulations, the effect of these structures on the turbulent intensities seems to be important already for Reynolds numbers as low as $Re_\tau = 365$. Therefore, in turbulent open channel flow, the domain size must be very large already at moderate Reynolds numbers, as figure 4.2a also confirms.

In the region $y/H \geq 0.4$, the values of v_{rms}^+ and w_{rms}^+ become similar for all the Reynolds numbers and domain sizes considered. At the surface, vertical fluctuations are damped and the turbulent kinetic energy is redistributed in the horizontal directions, which explains the increase observed near the surface in the u_{rms}^+ and w_{rms}^+ profiles. The region in which v_{rms}^+ starts to decrease is defined here surface-influenced region. While the boundary layer thickness at the wall strongly depends on the Reynolds number, the surface-influenced region thickness was found to be $0.25 \leq \delta_{SI}/H \leq 0.4$ for all the simulations performed. This region is defined in section 5.3 to start from the point of maximum $I = \overline{\langle u'u' + v'v' + w'w' \rangle} / \overline{\langle u'u' + w'w' \rangle}$ and to extend up to the surface. I can be seen as a measurement of the Reynolds stress anisotropy.

Bauer et al. [2020] reported that when the vertical direction is normalized with the near-surface viscous scale $l_v = Re_\tau^{-1/2} H$, v_{rms}^+ grows linearly moving from the surface toward the bulk of the channel for $(H-y)/l_v \leq 0.6$. In this region, all the values for the different Reynolds numbers considered were found to collapse and were well approximated by $v_{rms} = 0.36 \frac{H-y}{l_v}$. Figure 4.7 depicts the behavior of the velocity fluctuations in the vicinity of the free-surface for the present simulations and the scaling found in Bauer et al. [2020] is confirmed. Although the region in which the vertical derivative of the vertical velocity is linear is usually referred to as the Kolmogorov sub-layer, the above-mentioned scaling shows that the near-surface viscous scale l_v works better. With this finding, Bauer et al. [2020] demonstrated that a much finer grid resolution is required when an open channel flow is considered instead of a close channel flow. Our choice of a double stretching in the vertical direction at the two extremes of the domain is justified by the necessity to properly resolve this layer in an efficient manner.

At the surface, the u_{rms}^+ values ranging from 0.88 to 1 and the w_{rms}^+ values ranging from 0.78 to 0.83 were found to be in agreement with Borue et al. [1995], Komori et al. [1982], Nezu and Rodi [1986]. The small variation observed was explained by Calmet and Magnaudet [2003], who suggested a weak dependency of the values on the Reynolds number due to the very small turbulent kinetic energy dissipation in this region.

4.2.4 Turbulent kinetic energy budget

The turbulent kinetic energy equation budget reads:

$$\frac{\partial k}{\partial t} + \overline{\left\langle u_j \frac{\partial k}{\partial x_j} \right\rangle} = -\frac{1}{\rho} \frac{\partial \overline{\langle u_i' p' \rangle}}{\partial x_i} - \frac{1}{2} \frac{\partial \overline{\langle u_j' u_j' u_i' \rangle}}{\partial x_i} + \nu \frac{\partial^2 k}{\partial x_j^2} - \overline{\langle u_i' u_j' \rangle} \frac{\partial \langle u_i \rangle}{\partial x_j} - \nu \overline{\left\langle \frac{\partial u_i'}{\partial x_j} \frac{\partial u_i'}{\partial x_j} \right\rangle}, \quad (4.5)$$

where $k = \frac{1}{2}\left(\langle u'^2 \rangle + \langle v'^2 \rangle + \langle w'^2 \rangle \right)$ is the turbulent kinetic energy. Since open channel flows are statistically stationary as well as homogeneous in the streamwise and spanwise directions,
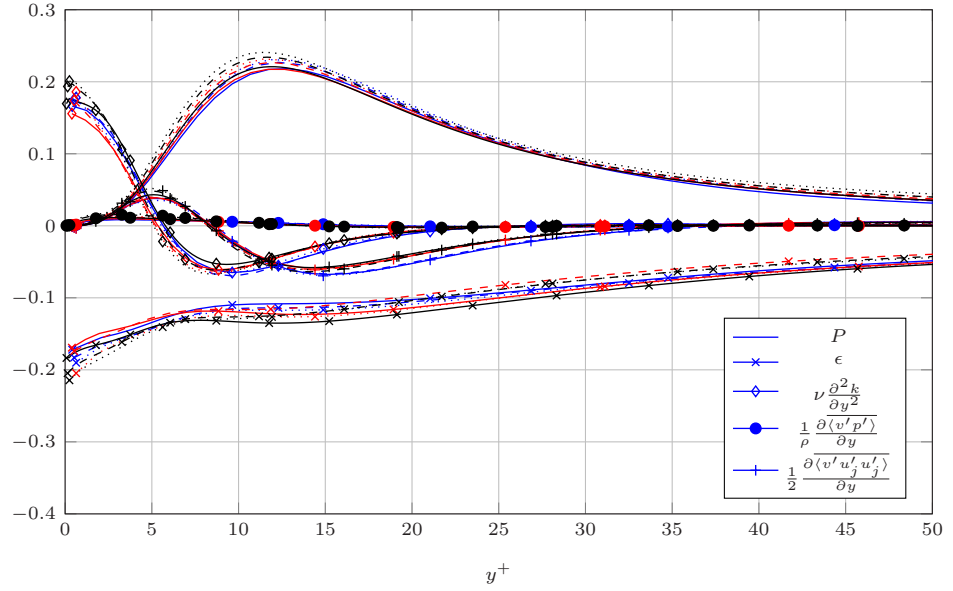
(a) Near the wall.
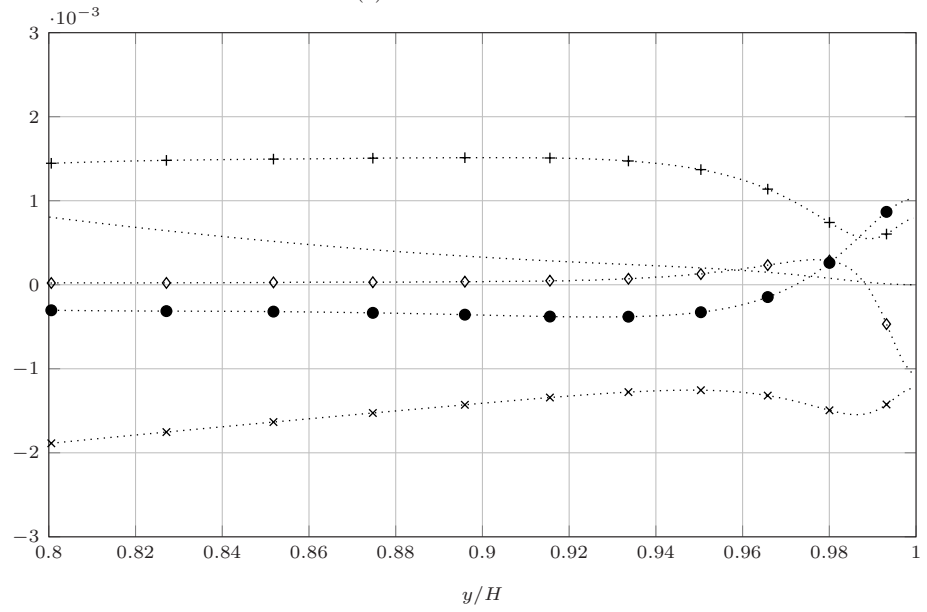
(b) Near the free-surface for simulation F09.

Figure 4.8: Turbulent kinetic energy budget: production $P = -\overline{\langle u'v'\rangle}\frac{\partial \overline{\langle u\rangle}}{\partial y}$, dissipation $\epsilon = 2\nu\overline{\langle S'_{ij}S'_{ij}\rangle}$, viscous diffusion $\nu\frac{\partial^2 k}{\partial y^2}$, pressure transport $\frac{1}{\rho}\frac{\partial \overline{\langle v'p'\rangle}}{\partial y}$ and turbulent convection $\frac{1}{2}\frac{\partial \overline{\langle v'u'_j u'_j\rangle}}{\partial y}$.

equation 4.5 can be simplified in the form (see Pope [2000]):

$$P - \epsilon + \nu \frac{\partial^2 k}{\partial y^2} - \frac{1}{\rho} \frac{\partial \overline{\langle v'p' \rangle}}{\partial y} - \frac{1}{2} \frac{\partial \overline{\langle v'u'_j u'_j \rangle}}{\partial y} = 0, \tag{4.6}$$

where $P = -\overline{\langle u'_i u'_j \rangle} \frac{\partial \langle u_i \rangle}{\partial x_j}$ is the production and $\epsilon = \nu \overline{\langle \frac{\partial u'_i}{\partial x_j} \frac{\partial u'_i}{\partial x_j} \rangle}$ the dissipation of turbulent kinetic energy. The remaining terms are usually defined as viscous diffusion $\nu \frac{\partial^2 k}{\partial y^2}$, pressure transport $\frac{1}{\rho} \frac{\partial \overline{\langle v'p' \rangle}}{\partial y}$ and turbulent convection $\frac{1}{2} \frac{\partial \overline{\langle v'u'_j u'_j \rangle}}{\partial y}$.

Figure 4.8a depicts the profile of each of the aforementioned components of the turbulent kinetic energy equation for all the simulations performed in the vicinity of the wall. When the turbulent kinetic energy components and the vertical height are normalized with viscous scales, the results from the different simulations show only a weak dependency on the Reynolds number in the inner layer. P increases from zero at the wall as y^3, to reach its maximum around $y^+ = 12$ for all the simulations. It can be demonstrated (Pope [2000]) that this peak occurs precisely where the viscous and Reynolds stresses are equal. Around this peak, production exceeds dissipation and the excess energy is transported away by turbulent convection and viscous transport. The latter transports energy to the wall, while the former also toward the log-law region. The contribution of pressure transport in this region is small and do not participate in the transport. Dissipation reaches its maximum at the wall and it is balanced by the viscous transport that is the only other non-negligible component.

Figure 4.8b depicts the behavior of the turbulent kinetic energy components in the vicinity of the surface for simulation F09. The choice to show only one simulation results is dictated by the lack of a unified scaling for every component from the bulk of the channel to its surface. The free-slip boundary condition allows all the components of the turbulent kinetic energy equation but the production to be non-zero at the surface. In the region $y/H \geq 0.8$, production is weak and the evolution of turbulent kinetic energy is essentially a balance between the total diffusion terms and the dissipation. The only component that is constantly positive is turbulent transport, which brings the energy toward the surface. Pressure transport becomes negative for $y/H \leq 0.97$ and reduces the transport of turbulence toward the surface. The variation of the viscous diffusion component from positive to negative produces a net increase of the sink terms in the turbulent kinetic energy budget. This is balanced by the positive value of the pressure transport at the surface. In this region, all the components but the pressure transport experience an abrupt variation. Calmet and Magnaudet [2003] linked this rapid change to viscous mechanisms that act only in the vicinity of the surface.

4.3 Very large scale motions

The analysis performed in this section focuses on the effects of VLSM on flow statistics. The first sub-section defines the size of coherent motions for different Reynolds numbers through pre-multiplied energy spectra of the streamwise velocity. In the second part, the study of integral length scales and their link to anisotropy are considered. In the end, the interaction between VLSM and small vortices is discussed.

(a) F07: $Re_\tau = 200$.

(b) F08: $Re_\tau = 365$.

(c) F09: $Re_\tau = 630$.
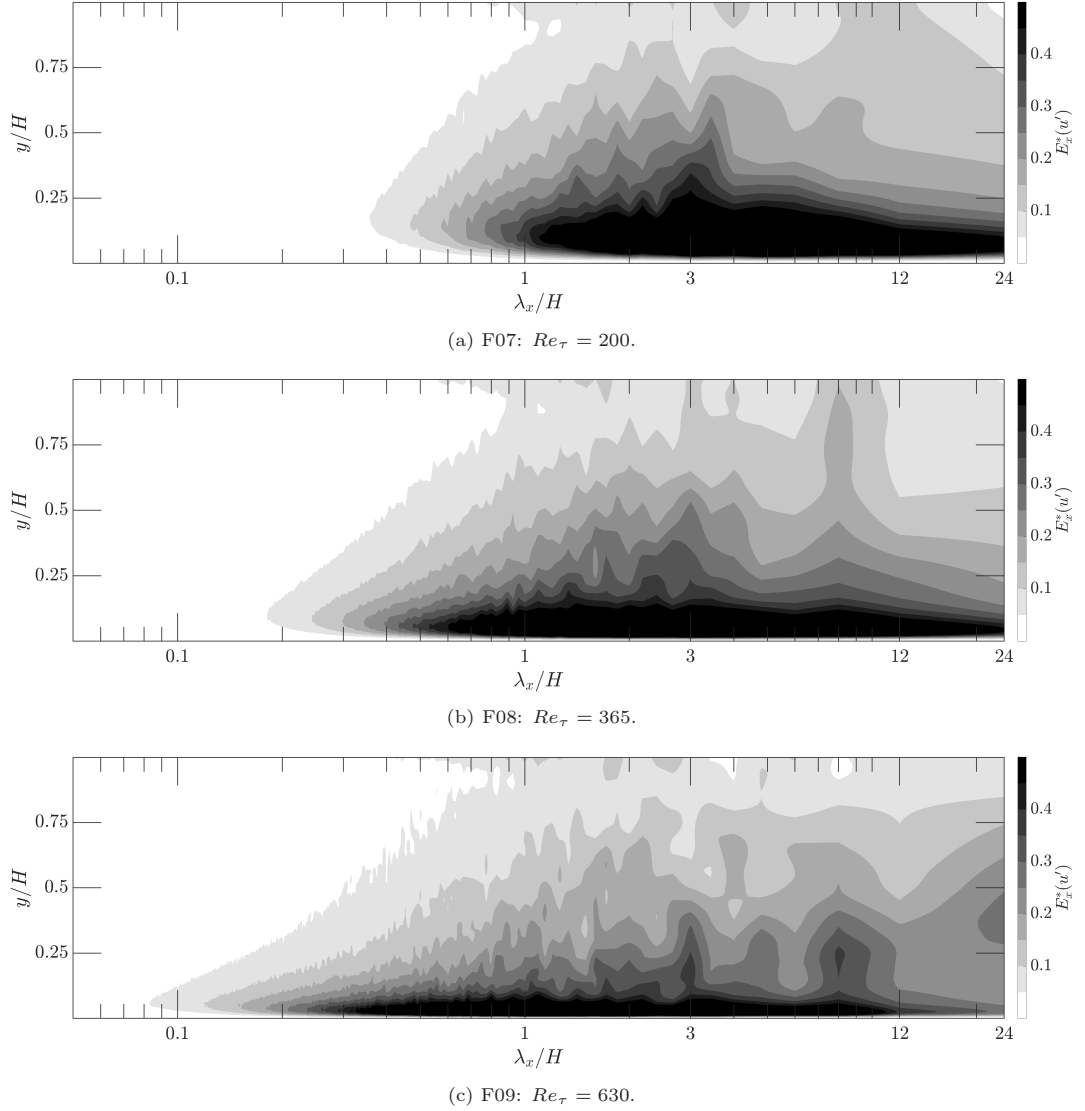
Figure 4.9: Contour maps of the averaged normalized pre-multiplied 1D spectra of the longitudinal velocity component in the streamwise direction ($E_x^*(u') = \mathrm{k}_x E_x(u')/(\mathrm{k}_x E_x(u'))_{max}$) as a function of non-dimensional streamwise wavelength (λ_x/H) and distance from the wall (y/H) for simulations F07, F08 and F09.

4.3.1 Pre-multiplied energy spectra

Figures 4.9 and 4.10 show the contour maps of the pre-multiplied 1D energy spectra of the longitudinal velocity component as a function of non-dimensional streamwise λ_x/H and spanwise λ_z/H wavelengths, respectively, and distance from the wall y/H for the simulations performed in the $24H \times 6H \times H$ domain (F07-F09). The wavelengths covered by the peak underline the scale of the most energetic structures of the flow field [Perry et al., 1986]. As expected, for increasing Reynolds number the amount of energy at smaller wavelengths was found to increase, especially near the bottom of the channel.

In the streamwise spectra (figure 4.9), an energy peak at a wavelength of $\lambda_x/H \approx 3$ was identified in all three cases. This peak is associated with LSM. It should be noted that in the spectra, the location of the peaks with higher wavelengths becomes less accurate due to the limited size of the computational domain $L_x = 24H$, $L_z = 6H$. Even though the location may

(a) F07: $Re_\tau = 200$.

(b) F08: $Re_\tau = 365$.

(c) F09: $Re_\tau = 630$.
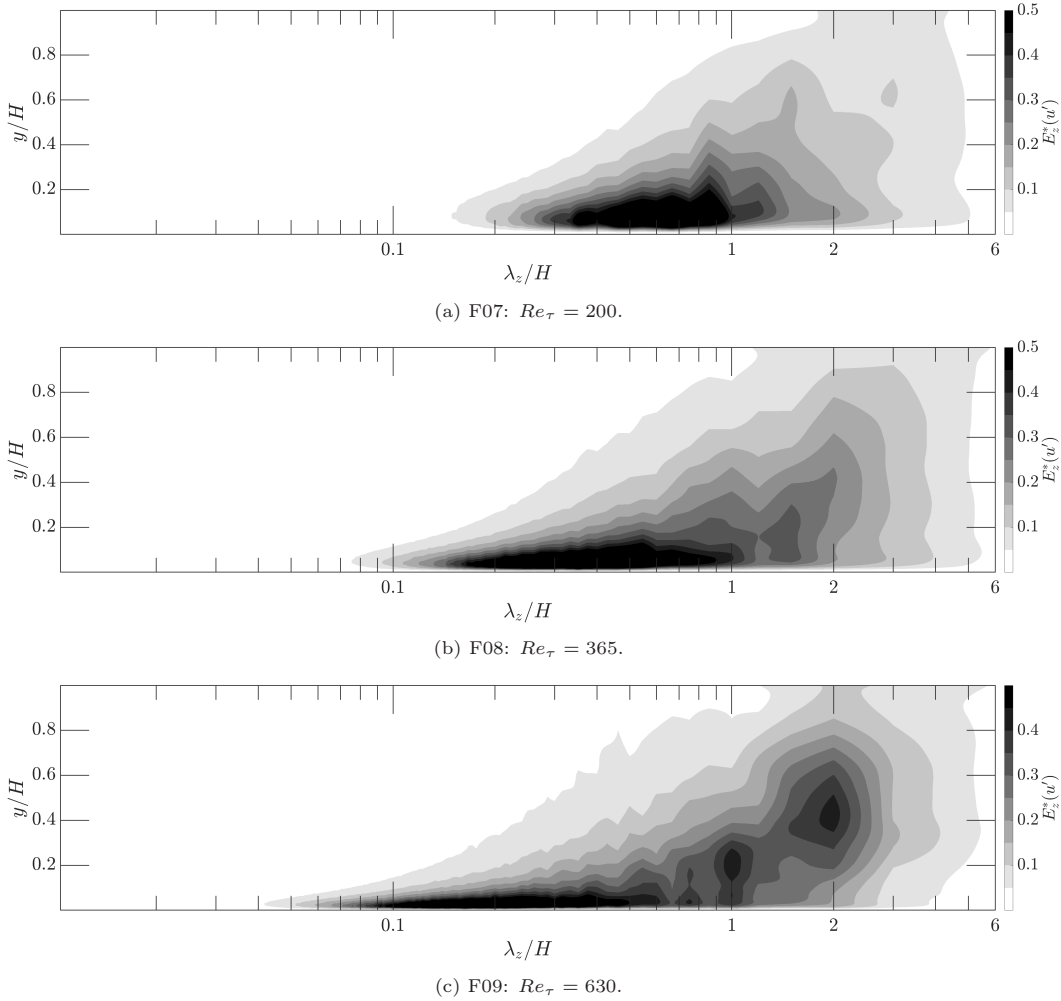
Figure 4.10: Contour maps of the averaged normalized pre-multiplied 1D spectra of the longitudinal velocity component in the spanwise direction ($E_z^*(u') = \mathrm{k}_z E_z(u')/(\mathrm{k}_z E_z(u'))_{max}$) as a function of non-dimensional spanwise wavelength (λ_z/H) and distance from the wall (y/H) for simulations F07, F08 and F09.

not be entirely correct, the energy peaks observed at $\lambda_x \gtrsim 10H$, which extend over virtually the whole channel height, indicate the presence of VLSM for $Re_\tau \geq 365$ (F08, F09). Previous literature sets the limit for the double peak to appear in canonical wall bounded flows at $Re_\tau = 1700$ (Hutchins and Marusic [2007]) and the VLSM effect on the streamwise turbulence intensities is usually considered to be visible at $Re_\tau \geq 1000$ (Moser et al. [1999], Hoyas and Jiménez [2006], Álamo et al. [2004]). These studies focused on close channel flow, while experimental [Peruzzi et al., 2020] and numerical [Wang and Richter, 2019] works on open channel flows observed the presence of a second peak in the spectral density as soon as $Re_\tau = 550$ is reached, in agreement with the present results. As expected, the early appearance of VLSM in open channel flows confirms the necessity to employ very large domain sizes, even when moderate Reynolds numbers are considered.

When examining the spanwise spectra (figure 4.10), energy peaks at $\lambda_z/H \approx 1$, which relate to LSM, were detected in all three cases. High energy values at $\lambda_z \geq 2$ (typical for VLSM) were observed for $Re_\tau = 365$ and $Re_\tau = 630$ when $y/H \geq 0.3$ and 0.1, respectively.

Figure 4.11 shows the pre-multiplied energy spectra of the longitudinal velocity in streamwise direction for the highest Reynolds number employed with the small and mid domain size simu-

(a) F03: $Re_\tau = 290$.

(b) F06: $Re_\tau = 290$.
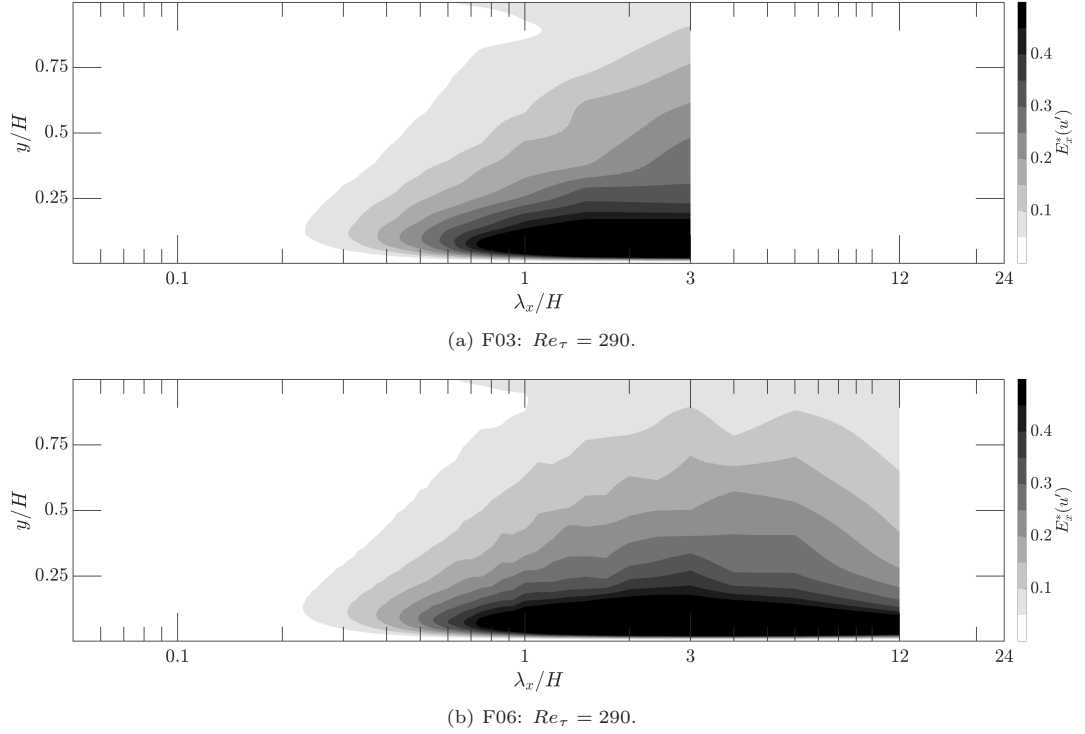
Figure 4.11: Contour maps of the averaged normalized pre-multiplied 1D spectra of the longitudinal velocity component in the streamwise direction ($E_x^*(u') = k_x E_x(u')/(k_x E_x(u'))_{max}$) as a function of non-dimensional streamwise wavelength (λ_x/H) and distance from the wall (y/H) for simulations F03 and F06.

lations. The analysis of this quantity underlined the inability of the smallest domain considered to capture even the LSM. In fact, the peak seems to extend above the maximum wavelength of the domain. The simulations with domain size $12H \times H \times 3H$ were able to partially capture these motions, but too small to be used with higher Reynolds numbers, in order to observe VLSM.

4.3.2 Integral length scales and anisotropy

Figure 4.12 shows the integral length scales for the velocity components in the homogeneous directions as a function of y/H for the largest domain size simulations F07, F08 and F09. For $y/H > 0.3$, a significant increase in the integral length scale in the $x-$direction L_{uu}^x was observed for $Re_\tau \geq 365$. The value of this quantity for the two highest Reynolds numbers considered was found to be almost twice the value found with $Re_\tau = 200$. Increasing Re_τ from 365 to 630 resulted in a marginal increase in L_{uu}^x by about 10% (figure 4.12a). This significant growth in L_{uu}^x for $Re_\tau \geq 365$ corresponds to the presence of VLSM. For $y/H \leq 0.05$, all integral length scales in the x-direction (L_{uu}^x, L_{vv}^x and L_{ww}^x) can be seen to decrease with increasing Reynolds number. This trend persists for L_{vv}^x for (almost) every y/H, and for L_{ww}^x until $y/H \approx 0.8$. Compared to the $x-$direction, with the possible exception of L_{ww}^z, the integral length scales in the $z-$direction do not show any significant Reynolds number effect. This could be due to the small difference in spanwise size between large and very large scale motions. In fact, while the size of VLSM in the streamwise direction is usually larger than $10H$, their size in the spanwise direction is usually $\simeq 2H$. On the other hand, the size of LSM is usually around $3H$ in the streamwise and H in the spanwise direction. It is clear how the presence of VLSM strongly

(a) Streamwise velocity component.

(b) Spanwise velocity component.

(c) Vertical velocity component.
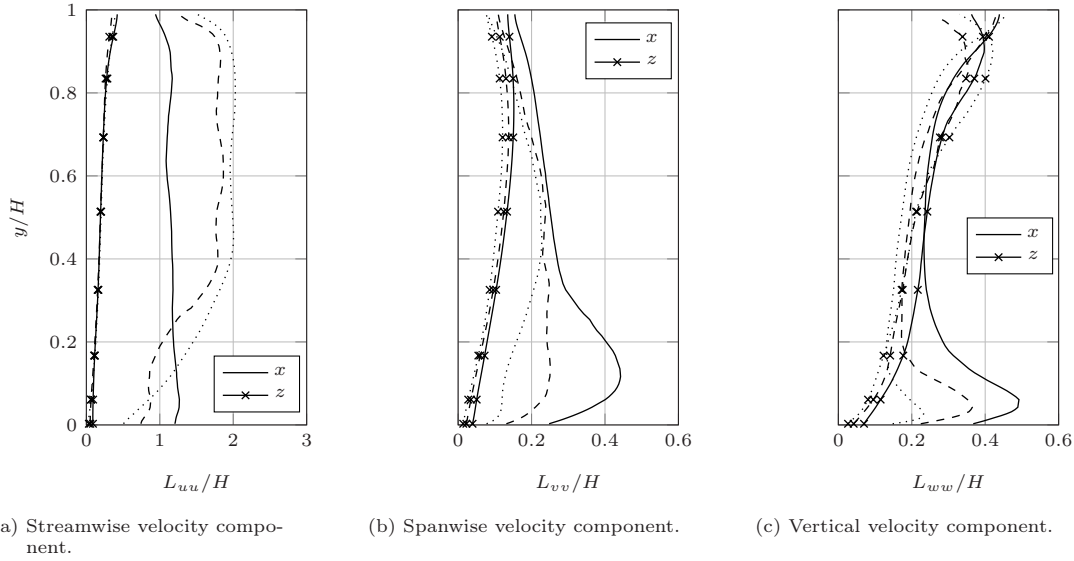
Figure 4.12: Averaged integral length scales for —— $Re_\tau = 200$, - - - $Re_\tau = 365$ and ⋯⋯ $Re_\tau = 630$ in streamwise x and spanwise z directions. The simulations were performed on a domain size of $24H \times H \times 6H$.

(a) Non-zero components of the anisotropy tensor as a function of the vertical direction normalized with the channel height H.

(b) Lumley triangle for the invariants of the Reynolds-stress. The color represents the vertical position of the anisotropy invariants normalized with the channel height H.
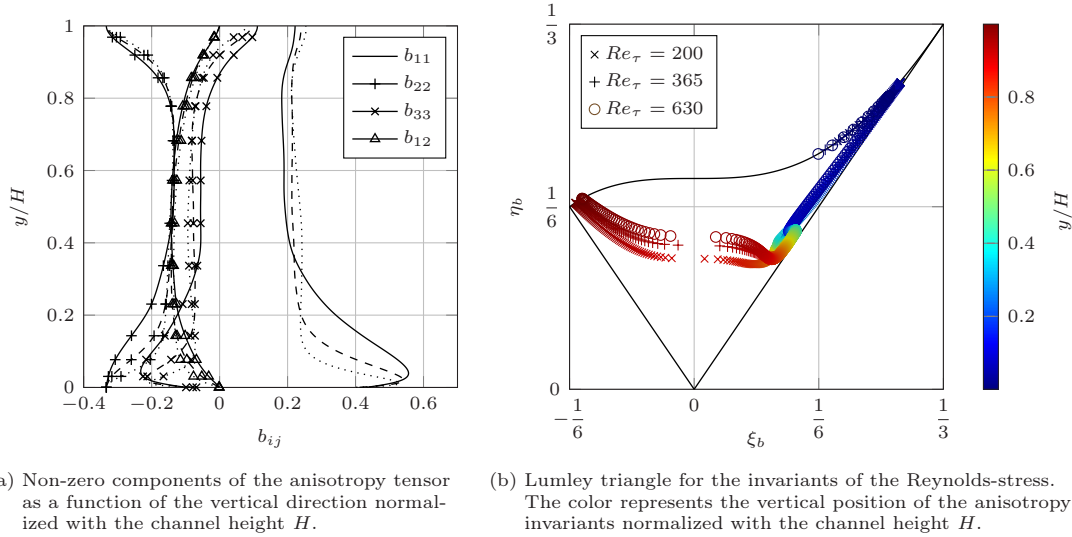
Figure 4.13: Representations of the anisotropy tensor for simulations F07, F08 and F09.

impact the integral length scales computed in the streamwise direction, while it does not affect their size in the spanwise direction.

The analysis of the integral length scales has been performed only on the largest domain size simulations, since de-correlation, even if marginal for $Re_\tau \geq 365$ at $y/H \geq 0.7$, is achieved at any height only in these runs. The values of the different integral length scales for every simulation are depicted in appendix A.6.

The anisotropy of the flow is increased when higher turbulence levels are considered. The anisotropy tensor **b** can be computed from the Reynolds stress tensor, as follows:

$$b_{ij} = \frac{\overline{\langle u_i' u_j' \rangle}}{2k} - \frac{\delta_{ij}}{3},$$

$$(4.7)$$
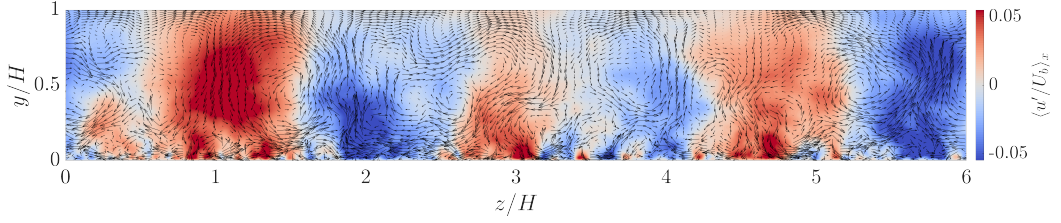
Figure 4.14: Contour plots of the streamwise averaged streamwise velocity fluctuation $\langle u'/U_b \rangle_x$ at a random chosen time from simulation F09. The black arrows represent the streamwise averaged velocity vector field.

where δ_{ij} is the Kronecker delta. Figure 4.13a shows the behavior of the different components of the anisotropy tensor in the vertical direction for different Reynolds numbers. In all the simulations, three regions can be defined. In the viscous wall region, the stress tensor is highly anisotropic, with large gradients. In the logarithmic region, the profiles show a plateau, while at the top of the channel, all the components deviate from the isotropic state due to the presence of the surface. It can be observed that b_{11} and b_{22} moves further away from 0 for $y/H \geq 0.4$, when the Reynolds number is increased. On the contrary, the values of b_{22} and b_{12} seem to be unaffected by the change in Re_τ. This means that, when higher turbulence levels are considered, the flow field becomes more anisotropic in the homogeneous directions x and z at $y/H \geq 0.4$.

The structure of b_{ij} can be graphically expressed through its two non-trivial invariants:

$$\eta_b = \sqrt{\frac{1}{6} b_{ij} b_{ji}}, \tag{4.8}$$

$$\xi_b = \left(\frac{1}{6} b_{ij} b_{jk} b_{ki} \right)^{\frac{1}{3}}, \tag{4.9}$$

where Einstein summation convention implies summation over repeated indices. Figure 4.13b depicts the Lumley triangles for Reynolds ranging from $Re_\tau = 200$ to 630 and a domain size of $24H \times H \times 6H$. The figure shows that near the wall, the turbulent fluctuations are very close to a two-dimensional state in which the vertical component is suppressed. Increasing the height, the points move towards a one-dimensional condition (upper right part of the triangle, around $1/6 \leq \xi_b \leq 1/3$ and $\eta_b = 1/3$). In the bulk of the channel, the points approach an isotropic state, defined as $\xi_b = 0$ and $\eta_b = 0$, up to the surface-influenced region, where there is a sudden deviation back toward the 2D state, $\xi_b = -1/6$ and $\eta_b = 1/6$. As can be seen, an increase in the Reynolds number increases the distance between the anisotropic invariant points close to the surface and the isotropic state.

4.3.3 Effect of VLSM on upwelling and downwelling regions

This section underlines the dynamics of the turbulent coherent vortices, from their formation at the wall to their interaction with the flat-shear surface. Hunt et al. [1988] proposed to define a vortex as a region where the vorticity magnitude is greater than the magnitude of the rate of strain. In order to define these regions, the authors developed the so-called Q-criterion. This criterion of vortex identification is based on the decomposition of the velocity gradient in two components, the rate-of-strain tensor $\boldsymbol{S} = \frac{1}{2}[\boldsymbol{\nabla u} + (\boldsymbol{\nabla u})^T]$ and the vorticity tensor $\boldsymbol{\Omega} = \frac{1}{2}[\boldsymbol{\nabla u} - (\boldsymbol{\nabla u})^T]$:

$$\boldsymbol{\nabla u} = \boldsymbol{S} + \boldsymbol{\Omega}. \tag{4.10}$$

u'/U_b

−0.20   0.20

y/H

0.50   1.00
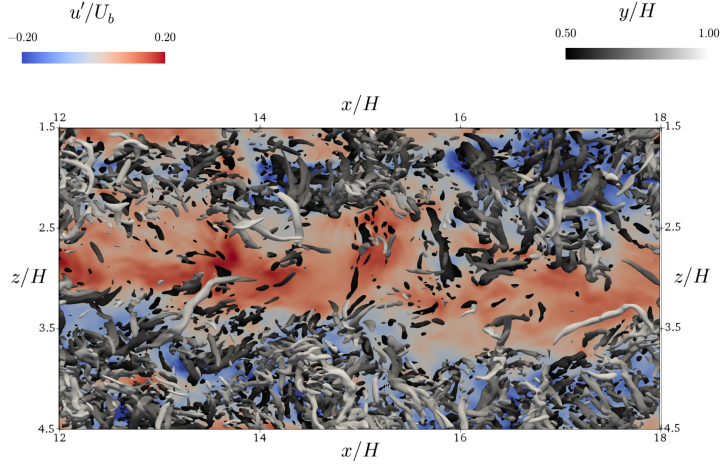
(a) Contour plot of the instantaneous streamwise velocity u' at $y/H = 0.5$ and iso-contours with values of $Q = 1$ colored with the normalized height of the channel y/H.

u'/U_b

−0.2   0.2

v'/U_b

−0.10   0.10
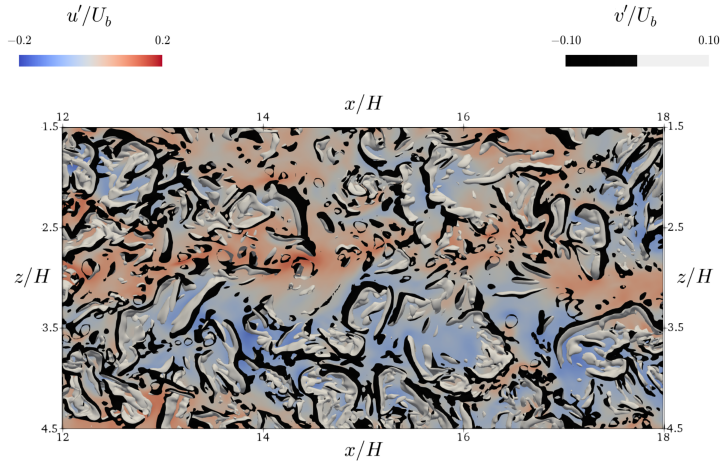
(b) Contour plot of the instantaneous streamwise velocity u' at $y/H = 0.9$ and iso-contours with values of $Q = 0.1$ colored with instantaneous streamwise u' and vertical v' velocity fluctuations, respectively.

Figure 4.15: Typical vortical structures visualized by iso-surfaces of the second invariant of ∇u for simulation F09. The color represents the fluctuating streamwise velocity component at different height of the channel.

From this definition, Hunt et al. [1988] defined a vortex as a spatial region where:

$$\hat{Q} = \frac{1}{2}(|\mathbf{\Omega}|^2 - |\mathbf{S}|^2) > 0, \tag{4.11}$$

where $\hat{Q}$ is the second invariant of the velocity gradient tensor. In order to avoid a random choice for the threshold to impose on the value of $\hat{Q}$ for vortex visualization, in the following, the normalization employed by Nagaosa and Handler [2003] is applied. Since vortices are produced by the presence of the bottom wall, the same threshold spanning over the whole channel would either underline too few vortices at the surface when a high value is chosen or cause confusion, because the iso-surface of $\hat{Q}$ covers too much volume of the flow domain, when the threshold is low. Therefore, the normalized value Q reads:

$$Q(x,y,z,t) = \frac{\hat{Q}(x,y,z,t)}{\hat{Q}_{rms}(y)}, \tag{4.12}$$

where $\hat{Q}_{rms}$ is the rms of $\hat{Q}$. The normalization is based on the fact that the value of the root-mean-square of Q has a peak in the vicinity of the wall, such that a decrease in the amount of visualized vortices is locally applied. The main advantages of this normalization are the ability to visualize vortices all over the channel, instead of having them concentrated at the wall, and the possibility to determine a universal threshold level Q for the whole channel, as demonstrated in Nagaosa and Handler [2003].

Figure 4.14 shows contours of the streamwise-averaged velocity fluctuation $\langle u' \rangle_x$, together with streamwise-averaged velocity vectors. Large areas with high and low speed streamwise flow can be observed, which extend almost from the bottom to the top of the channel. Downward moving flow is typically present in the high $\langle u' \rangle_x$ areas, while in the low $\langle u' \rangle_x$ areas the flow tends to move upwards. It was observed in figure 4.1 that these high and low speed areas extend over a significant streamwise portion of the channel, and are related to VLSM. The rotation of large streamwise-aligned vortices create two regions on their sides, an upwelling and a downwelling region, and spanwise movements above and below themselves. This observation is coherent with the overall model depicted in Zhong et al. [2016]. The larger is the Reynolds number the larger and stronger are these vortices. Due to their disposition and rotation directions, divergence regions lies over upwelling motions and, vice versa, convergence regions over downwelling motions. While Zhong et al. [2016]'s model focused on the description of large scale motions, here the effect of these structures on smaller vortices is analyzed.

Figure 4.15a shows contours of streamwise velocity fluctuations u' in the plane at $y/H = 0.5$. Superimposed on this plot are small-scale vortical structures in the interval $0.5 \leq y/H \leq 1$ that are visualized using the aforementioned normalized Q-criterion. It is known that low-speed streaks form due to the upward ejection of relatively slow moving fluid from the lower part of the boundary layer [e.g. Komori et al., 1982], while high-speed streaks form when relatively fast moving fluid moves downwards. In figure 4.15a, it can be seen that the vast majority of the small-scale vortical structures is present inside large low-speed streaks that extend toward the surface. The presence of these small structures in low-speed streaks is explained by the fact that the turbulence intensity in the lower part of the boundary layer is significantly larger than in the upper part. Figure 4.14 shows that these vertical motions are mostly due to the presence of large streamwise vortices that, rotating, transport the small eddies toward the surface. When the small vortices approach the surface they either align with or become orthogonal to the surface, which are referred to by surface-aligned and surface-attached vortices, respectively. Figure 4.15b shows an instantaneous snapshot of the upper part $(y/H \geq 0.9)$ of the channel. Most of the surface-attached vortices were found above downwelling motions corresponding to high-speed streaks. As mentioned above, in low-speed streaks most of the vortical structures are present. These structures tend to align with the surface due to the shear generated underneath the divergent flow at the surface. In these low-speed regions, the surface aligned vortices are often ring-shaped, which, according to Nagaosa and Handler [2003], started their life as hairpin vortices from near the bottom of the channel.

The implications of the above on interfacial mass transfer will be discussed in chapter 5.

5 Mass transfer

This chapter presents the interfacial mass transfer simulations results. These were started from the flow fields analyzed in chapter 4. Table 5.1 shows the parameters chosen for such simulations. Refinement factors up to 6 were employed in order to simulate mass transfer for Schmidt numbers ranging from 1 to 200. The bulk Reynolds number was varied from 2875 to 12000. Different domain sizes were employed, in order to assess the effect of VLSM, present only in the largest domain considered (see section 4.3), on mass transfer. On average 40 bulk time units for the small and mid domain simulations and 20 for the large domain simulations were needed for the scalar statistics to converge. Statistics were then collected for a time window dependent on the domain size. All the flow statistics presented in the present chapter are computed in the same time window in which mass transfer is studied. Therefore, they could differ from the statistics shown in chapter 4, even if the differences are expected to be small. The values averaged on the homogeneous planes x, z are represented by $\langle \cdot \rangle$, while the values averaged in time are represented by $\overline{\cdot}$. $\cdot^+$ represents averaged data normalized with viscous scales.

The chapter is divided in three main sections. The first section proves the adequacy of the meshes employed for the most problematic simulations performed. The second section demonstrates the sufficiency of the chosen time window that allows to capture correctly scalar statistics. The third section describes the applicability of the mass transfer models described in chapter 2 to the present results. In the end, an analysis of the interaction between surface divergence and mass transfer is performed. Instantaneous snapshots define the role of the different turbulent coherent structures typical of open channel flow in the mass transfer phenomenon. A comparison with the isotropic turbulence driven flow data of Herlina and Wissink [2019] shows the effect of choosing different flow types. [1]

---

[1] Part of the results reported in this chapter were also presented in Pinelli et al. [2022].

Run	Re_b	Re_τ	Sc	$L_x \times L_y \times L_z$	$N_x \times N_y \times N_z$	$f_R^x \times f_R^y \times f_R^z$	$\Delta t/t_b$
G01	3000	190	$8^R, 16^R$	$3H \times H \times 3H$	$192 \times 128 \times 192$	$3 \times 2 \times 3$	200
G02	4000	240	8^R	$3H \times H \times 3H$	$192 \times 128 \times 192$	$2 \times 2 \times 2$	100
G03	5000	290	$4^R, 8^R$	$3H \times H \times 3H$	$192 \times 128 \times 192$	$3 \times 3 \times 3$	120
G04	2875	180	$7, 64^R, 100^R$	$12H \times H \times 3H$	$384 \times 128 \times 192$	$3 \times 4 \times 3$	230
G05	4000	240	$7, 16^R, 32^R$	$12H \times H \times 3H$	$384 \times 128 \times 192$	$2 \times 2 \times 2$	130
G06	5000	290	$7^R, 16^R$	$12H \times H \times 3H$	$384 \times 128 \times 192$	$3 \times 3 \times 3$	120
G07	3200	200	$7, 16^R, 200^R$	$24H \times H \times 6H$	$1152 \times 384 \times 1152$	$6 \times 2 \times 2$	60
G08	6400	365	$7^R, 16^R, 100^R$	$24H \times H \times 6H$	$1152 \times 384 \times 1152$	$6 \times 2 \times 2$	60
G09	12000	630	$7^R, 16^R, 64^R$	$24H \times H \times 6H$	$1152 \times 384 \times 1152$	$6 \times 2 \times 2$	60

Table 5.1: Overview of simulations. Re_b is the bulk Reynolds number, Re_τ is the friction Reynolds number, Sc is the Schmidt number, H is the channel height, $L_x \times L_y \times L_z$ denote the size of the domain in x, y, z directions, respectively, x, N_y and N_z are the number of grid points of the base mesh, while $f_R^x \times f_R^y \times f_R^z$ represents the refinement factors applied to the scalar mesh for the Sc with superscript $*^R$ in x, y, z directions, respectively, and $\Delta t/t_b$ is the time window employed for the average.
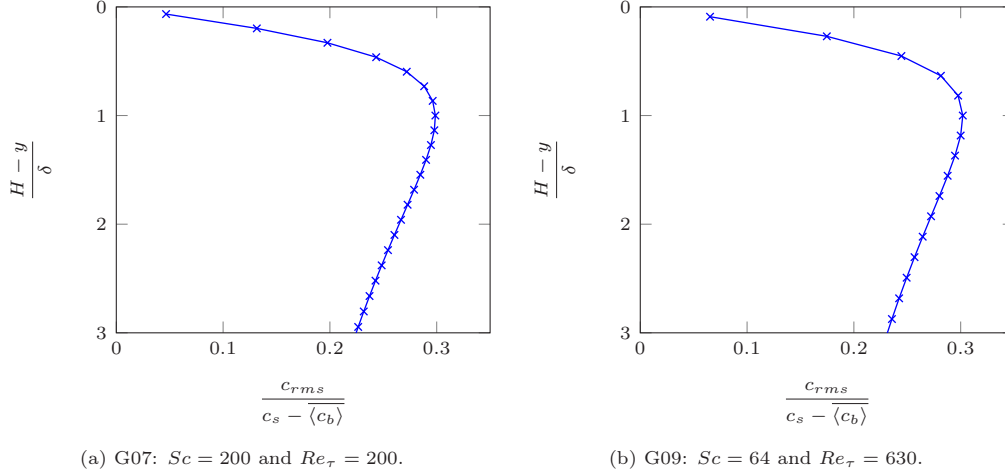
(a) G07: $Sc = 200$ and $Re_\tau = 200$.

(b) G09: $Sc = 64$ and $Re_\tau = 630$.

Figure 5.1: rms of concentration to prove the fulfillment of the second criterion described in Grötzbach [1983] for simulations G07 and G09.
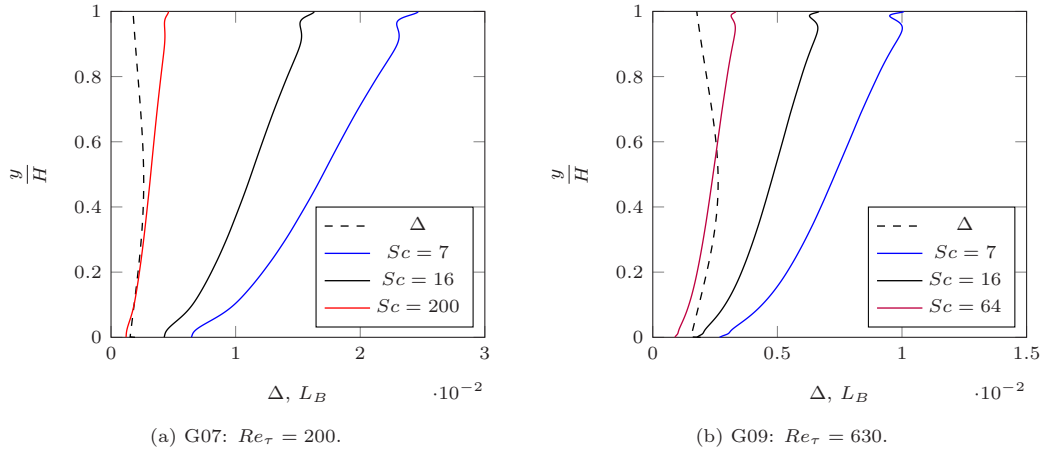
(a) G07: $Re_\tau = 200$.

(b) G09: $Re_\tau = 630$.

Figure 5.2: Comparison between mean grid width Δ and Batchelor scales L_B for simulations G07 and G09.

5.1 Definition of the refinement factor

Before proceeding to the analysis of the scalar statistics, the method chosen in the present thesis to define the refinement factor to apply to the scalar simulations is presented. Grötzbach [1983] proposed three criteria for the determination of the grid spacing that allows accurate direct numerical simulations of heat transfer in turbulent flows:

1. "the periodicity lengths must be chosen large enough to record all relevant large-scale vortices." [Grötzbach, 1983]

2. "The vertical grid width distribution must be able to resolve the steep gradients in the velocity and temperature fields near the boundaries." [Grötzbach, 1983]

3. "The mean grid widths must be smaller than the smallest relevant turbulence elements." [Grötzbach, 1983]

In the paper, these criteria were tested comparing different direct numerical simulations for the Rayleigh-Bénard convection of air in an infinite channel. In the present chapter, only the second and third criteria were considered to test the grid resolution chosen to correctly resolve the Batchelor scales, since the adequacy of the domain lengths was assessed in chapter 4.

Grötzbach [1983] demonstrated that the second criterion for $Sc \geq 1$ is fulfilled using a minimum of 3 nodes within the scalar boundary layer. This condition allowed the correct resolution of the scalar fluxes. Moreover, the mean grid width, defined as $\Delta = (\Delta x \, \Delta y \, \Delta z)^{1/3}$, must be $\leq \pi L_B$, in order to satisfy the third criterion. $L_B = \nu/\sqrt{Sc}$ is the Batchelor scale and defines the minimum length scale for scalar motion.

Figure 5.1 depicts the root mean square of the concentration c_{rms} in the vertical direction normalized by the diffusive boundary layer thickness δ (see section 5.2.1 for a detailed discussion of this quantity). Figure 5.1 shows the fulfillment of the second criterion for the simulations with the highest Schmidt (figure 5.1a) and Reynolds (figure 5.1b) numbers performed. 8 grid points can be observed in position $(H - y)/\delta \leq 1$ for G07 and 6 in G09, such that the second criterion is definitely satisfied for both the simulations. In figure 5.2, the mean grid width is compared to the Batchelor scales for $Sc = 7, 16, 200$ (G07) and $Sc = 7, 16, 64$ (G09). Δ is always smaller than L_B for $Sc \leq 16$ in both the simulations. When $Sc = 200$ and $Re_\tau = 200$ are considered, the third criterion is fulfilled for $y/H \geq 0.1$, while for simulation G09 and $Sc = 64$, only for $y/H \geq 0.55$. In both cases, no oscillations in the instantaneous concentration were detected in the bottom part of the channel and the data were found to be valid for the analysis of interfacial mass transfer. Moreover, 8 and 6 points lie within the diffusive boundary layer for both simulations (see figure 5.1), such that the chosen mesh at the surface is more than capable to resolve the small scales typical of high Schmidt and Reynolds numbers close to the surface. A part from these two extreme cases, all the other simulations completely fulfilled the second and third criteria defined in Grötzbach [1983].

5.2 Statistics of the scalars

As stated in section 3.2, mass transfer was modelled considering a Dirichlet boundary condition at the surface (c at saturation). In order to save computational time, the simulations were started with a concentration field that represents the solution of the unsteady diffusion equation at a chosen time $t = 10$ for the small domain size simulations and $t = 12$ for the others. The concentration gradient created is the mechanism that causes mass transfer at the surface. If a simulation is run for long enough time, the whole domain will be saturated and mass transfer will consequently stop due to the absence of a vertical concentration gradient. This sets a maximum in the gathering of the scalar statistics. Moreover, to ensure that the obtained scalar statistics are quasi-steady, these were collected after a transient period of time. Therefore, the time ranges chosen for the scalar statistics span between these two extremes and the condition $\partial \langle c \rangle / \partial y > 0$ was always fulfilled.

In the first sub-section, the diffusive boundary layer thickness is analyzed, in order to define its dependency on Schmidt and Reynolds numbers. This scale is then employed to normalize the vertical direction to study concentration and mass fluxes vertical profiles.

5.2.1 Boundary layer thickness

Figure 5.3 shows typical contours of the concentration and qualitatively depicts the interaction between the turbulent open channel flow and the scalar transport at (a),(c) $Sc = 7$, (d) $Sc = 64$ and (b) $Sc = 100$. The thickness of the concentration boundary layer δ depends on both the Reynolds and the Schmidt numbers. Comparing the left (low Sc) and right (high Sc) panes, it can be clearly seen that an increase in Schmidt number at constant Re_b results in much finer concentration filaments in the bulk and a significantly reduced δ. The same effect can be seen

(a) G08: $Re_b = 6400$ and $Sc = 7$.

(b) G08: $Re_b = 6400$ and $Sc = 100$.

(c) G09: $Re_b = 12000$ and $Sc = 7$.

(d) G09: $Re_b = 12000$ and $Sc = 64$.
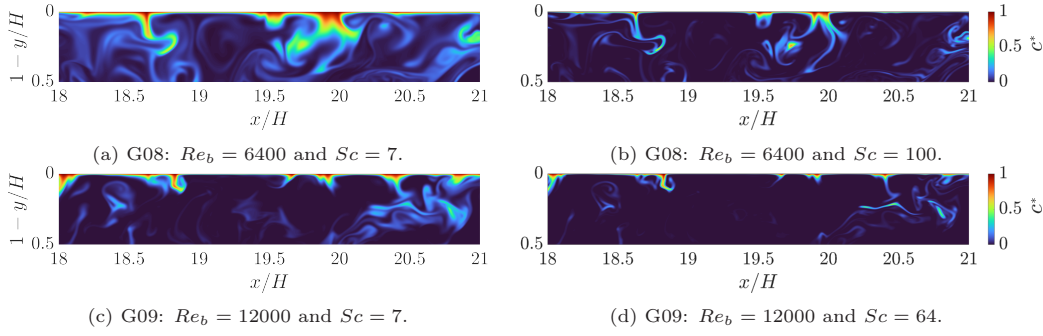
Figure 5.3: On the top row, slices of simulation G08 in the xy-plane at $z/H = 3$. On the bottom row, slices of simulation G09 in the xy-plane at $z/H = 3$. The colormaps represent the normalized concentration $c^* = \frac{c - \langle c_b \rangle}{c_s - \langle c_b \rangle}$ for the different Schmidt numbers. All the figures are taken at time $t/t_b = 42$ and for $Sc = 7$ (left panes), 100 (right top pane) and 64 (right bottom pane).
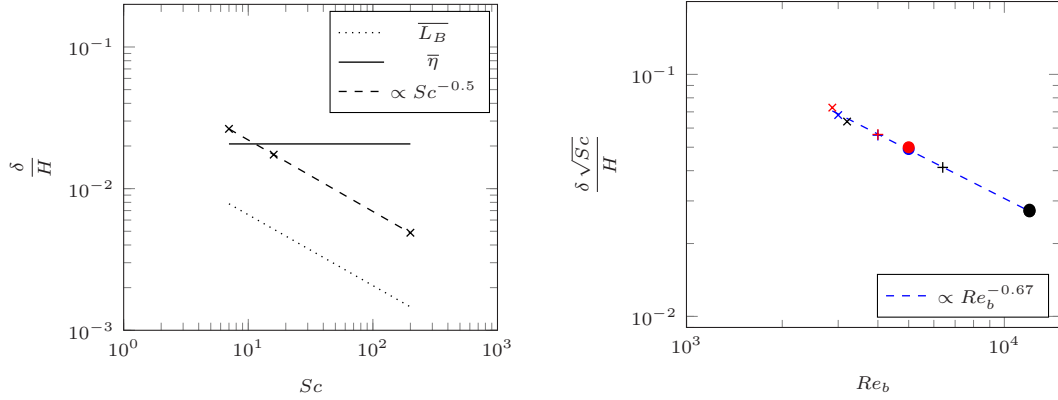
(a) Variation of boundary layer thickness δ with Sc compared to the Kolmogorov η and the Batchelor L_B scales for simulation G07.

(b) Variation of boundary layer thickness δ normalized with $\sqrt{Sc}$ with Re_b.

Figure 5.4: Variation of scalar boundary layer thickness δ with Schmidt Sc and bulk Reynolds Re_b numbers for simulations × G01, + G02, ● G03, × G04, + G05, ● G06, × G07, + G08, ● G09.

comparing figures 5.3a and 5.3c, where only the Reynolds number varies. Even if the Schmidt number is the same, it can be clearly observed a reduction in the thickness of the boundary layer and a thinning of the size of the structures. Note that the above reduction in δ at a fixed Re_b is due to the increase in interfacial mass transfer resistance with increasing Schmidt number. At a fixed Sc, the increase in turbulence in the bulk associated with an increase in Re_b results in improved mixing with a reduction of δ, which in this case promotes mass transfer.

The thickness of the diffusive concentration boundary layer δ is identified using

$$\delta = \frac{D}{K_L} = Sh^{-1}H, \tag{5.1}$$

where the Sherwood number $Sh = K_L H / D$ is the ratio between the convective and the diffusive mass transfer. As illustrated in figure 5.4a for simulation G07, in all simulations δ was found to scale with $Sc^{-0.5}$, which is in agreement with the theoretical prediction for a shear-free interface [Jähne and Haußecker, 1998, Ledwell and Jirka, 1984]. Included in this plot are the thicknesses of the Kolmogorov sublayer η and the Batchelor sublayer $L_B = \eta/\sqrt{Sc}$ at the interface. Except for $Sc = 7$, it was found that $L_B < \delta < \eta$ for all the simulations performed, which is in agreement with Herlina and Wissink [2014].

(a) Concentration profiles for $Re_b = 6400$.

(b) Concentration profiles for $Sc = 16$, $Sc = 20$ (HW19) and $Sc \simeq 500$ (HJ08).

(c) rms of the concentration for $Re_b = 6400$.

(d) rms of the concentration for $Sc = 16$, $Sc = 20$ (HW19) and $Sc \simeq 500$ (HJ08).
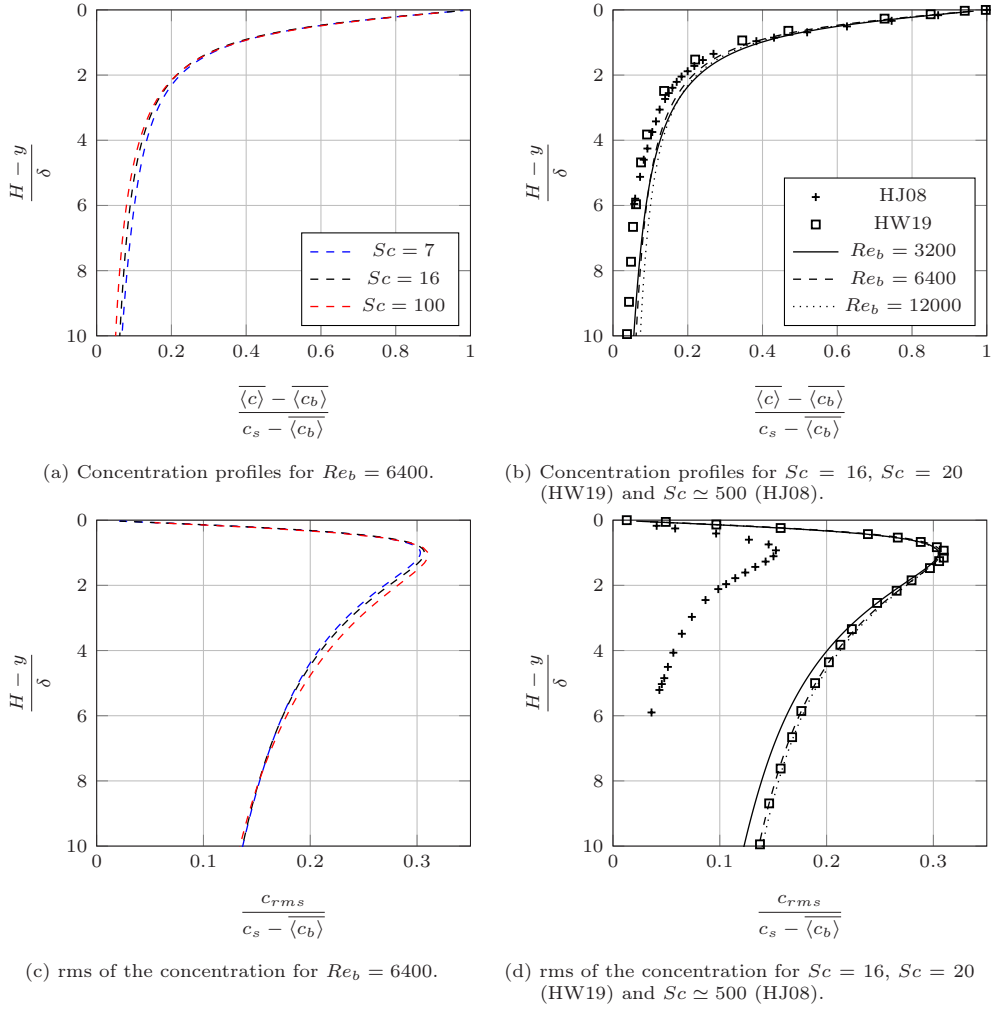
Figure 5.5: Profiles for mean and rms of the concentration as a function of the vertical direction for simulations G06, G07 and G08 for different Schmidt and Reynolds numbers. Mean and rms of concentration are normalized with the difference between the concentration at the surface c_s and in the bulk c_b, while the vertical direction is non-dimensionalized with the concentration boundary layer thickness δ. The data are compared with Herlina and Jirka [2008] (HJ08) and Herlina and Wissink [2019] (HW19) with $Re_T = 780$, $Sc \simeq 500$ and $Re_T = 1200$, $Sc = 20$ respectively.

Figure 5.4b shows the variation of $\delta\sqrt{Sc}$ with the bulk Reynolds number Re_b. The best fit through the data points was found with a linear regression to be $\delta\sqrt{Sc} \propto Re^{-0.67}$. This scaling is similar to the one found by Nagaosa and Handler [2012], $Sh\sqrt{Sc} \propto Re_b^{0.75}$, as will be discussed further in section 5.3.

5.2.2 Mean and fluctuating concentration profiles

Figure 5.5 shows mean and r.m.s. of concentration fluctuations:

$$c_{rms} = \sqrt{\langle c^2 \rangle - \langle c \rangle^2} \tag{5.2}$$

at various Reynolds and Schmidt numbers for simulations G07, G08 and G09. As discussed above, the boundary layer thickness δ depends on both the molecular diffusivity (Sc) and the Reynolds number (Re_b). Thus, it is expected that the vertical profiles of the normalized mean scalar quantities exhibit self-similarity when the vertical y direction is normalized by δ. This is
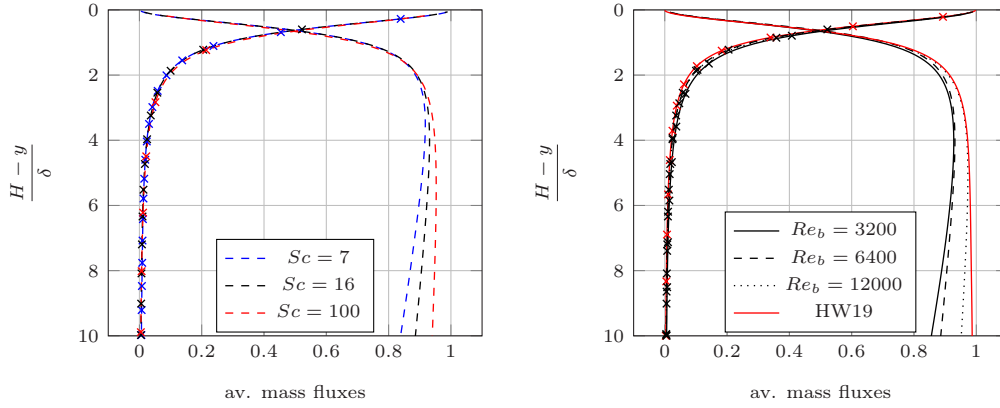
(a) Mass fluxes near the surface for simulation G08.

(b) Mass fluxes near the surface for simulations G07, G08 and G09 for $Sc = 16$ compared with Herlina and Wissink [2019] (HW19).

Figure 5.6: Variation of the diffusive (cross) and turbulent (solid) mass fluxes with depth for different Schmidt and Reynolds numbers. The mass fluxes are normalized by the total mass flux at the surface and the vertical direction with the diffusive boundary layer thickness δ. The data are taken from simulations G07, G08 and G09.

confirmed in figures 5.5a and 5.5b, where all the concentration profiles collapse in one plot for different Schmidt and Reynolds numbers. A comparison with previous experimental [Herlina and Jirka, 2008] and numerical results [Herlina and Wissink, 2019] shows a very good agreement, even though the flow and the Reynolds numbers are different.

In all simulations, the magnitude of δ was found to be virtually identical to the distance between the surface and the point at which the r.m.s. of the concentrations reaches its maximum. Hence, the c_{rms} peak in figures 5.5c and 5.5d is located at $(H - y)/H = \delta/H$. The maximum $c_{rms}/(c_s - \overline{\langle c_b \rangle})$ values were ≈ 0.3 for all the simulations performed, which is in agreement with previous numerical [Herlina and Wissink, 2014, 2019, Magnaudet and Calmet, 2006] and experimental [Atmane and George, 2002] results. The lower normalized c_{rms} peak values of $\approx 0.1 - 0.2$ obtained in the experiments of Herlina and Jirka [2008] indicate a partially contaminated surface, as confirmed by the numerical studies of Khakpour et al. [2011], Wissink et al. [2017].

5.2.3 Interfacial mass flux

As mentioned in the previous sections, the total averaged mass flux comprises a diffusive $\overline{\langle j_d \rangle} = -D\frac{\partial \langle c \rangle}{\partial y}$ and a turbulent $\overline{\langle j_t \rangle} = \overline{\langle c'v' \rangle}$ component. Figure 5.6 illustrates that j_d acts mainly at the surface, where v' is damped due to the two-dimensionality imposed by the free-slip boundary condition. While the contribution of j_d to the total flux reduces with distance from the surface, at the same time j_t gradually takes over. At $y \simeq 0.65\delta$ the diffusive and turbulent mass fluxes are equally important for the scalar vertical transport towards the bulk for all the Reynolds and Schmidt numbers considered, in agreement with results from isotropic turbulence driven flows [Herlina and Wissink, 2014, 2019]. The normalization of the depth of the channel with the boundary layer thickness allows to remove the dependency on the Schmidt and Reynolds numbers in the vicinity of the surface ($(H - y)/\delta \leq 10$) in isotropic turbulence driven flow, as demonstrated in Herlina and Jirka [2008], Herlina and Wissink [2014, 2019], Janzen et al. [2010]. On the contrary, figure 5.6 shows that, when a no slip boundary condition at the bottom is considered, the fluxes collapse only within $(H - y)/\delta \leq 2$ in the time windows considered. Below this threshold, turbulent mass flux in the present simulations shows lower values compared to

(a) Variation of normalized $K_L\sqrt{Sc}/U_b$ with Re_b.

(b) Variation of normalized $K_L\sqrt{Sc}/u_\tau$ with Re_τ.

(c) Variation of normalized $K_L\sqrt{Sc}/u_\infty$ with Re_T.

(d) Variation of $K_L\sqrt{H/(D\,U_b)}$ with $\sqrt{\beta_{rms}H/U_b}$.
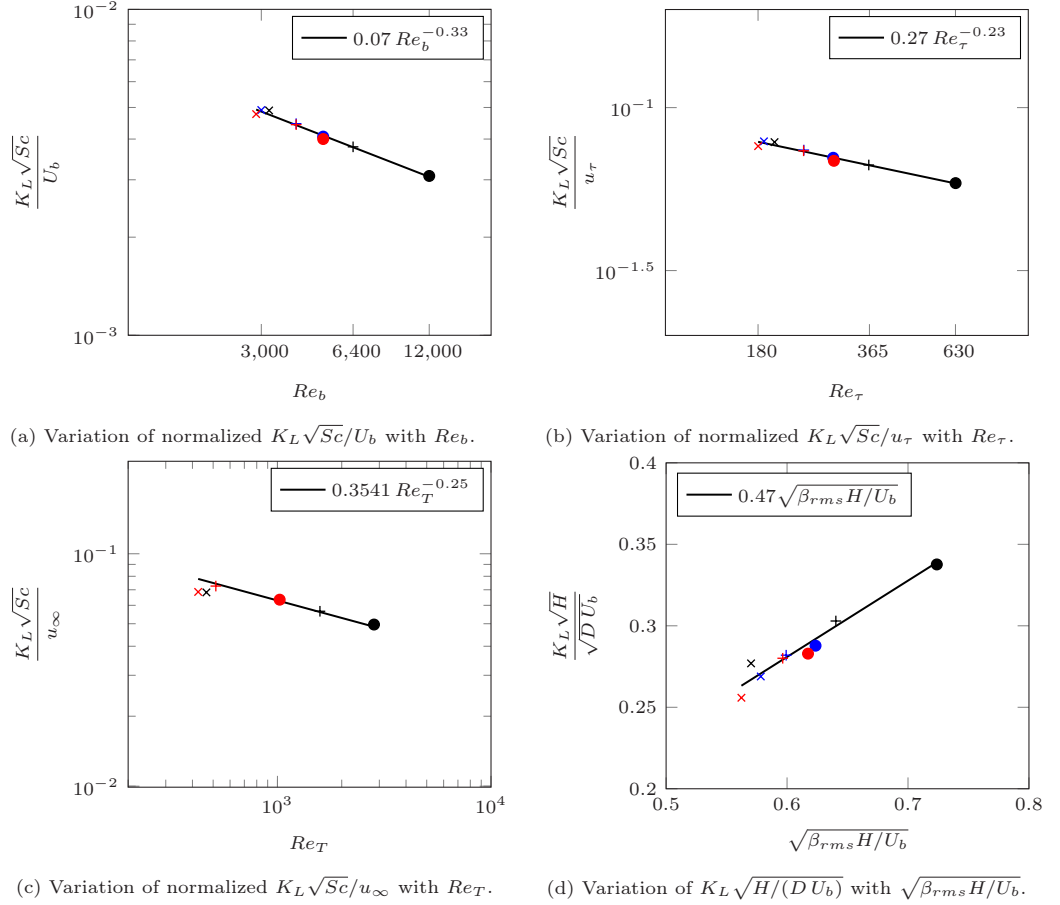
Figure 5.7: Averaged normalized mass transfer velocity K_L as a function of bulk Re_b, friction Re_τ, turbulent Re_T Reynolds numbers and surface divergence β. The simulations presented are × G01, + G02, ● G03, × G04, + G05, ● G06, × G07, + G08, ● G09.

isotropic turbulence driven flows, with differences of $5-15\%$ already at 10δ from the surface. This difference seems to decrease when higher Reynolds and Schmidt numbers are considered.

5.3 Scaling of mass transfer velocity

As mentioned above, $\delta = Sh^{-1}H$, thus it can be readily inferred from figure 5.4 that the mean transfer velocities K_L obtained in the present simulations scale with $Sc^{-0.5}$ and $Re_b^{-0.33}$ (cf. figure 5.7a). In Wissink et al. [2017], it was found that surface conditions progressively change the exponent of $K_L \propto Sc^n$ from $n = -1/2$ for a clean surface to $n = -2/3$ for a contaminated surface. The present study focuses only on clean surface interfacial mass transfer, therefore, the exponent found in all the simulations (-0.5) confirms the validity of the results. The scaling of $K_L \propto Re_b^{-0.33}$ is in agreement with the DNS of Nagaosa and Handler [2012] who showed that $Sh \propto Re_b^{0.75}$, i.e. $K_L \propto Re_b^{-0.25}$. The depicted data in Moog and Jirka [1999] were found to scale as $K_L \propto Re_\tau^{-0.29}$ with a 95% confidence for the reported exponent that spanned from -0.14 to -0.44. A linear regression of the present data showed that $K_L/u_\tau \propto Re_\tau^{-0.23}$ (cf. figure 5.7b), which is inside the aforementioned interval of confidence. The limitations of the cited papers were the scatter and large uncertainties present in the data of Moog and Jirka [1999] and the limited computational domains ($5H \times H \times 2.5H$ for $Re_\tau = 150$ and $2H \times H \times H$ for $Re_\tau = 600$) and Schmidt number ($Sc = 1$) employed by Nagaosa and Handler
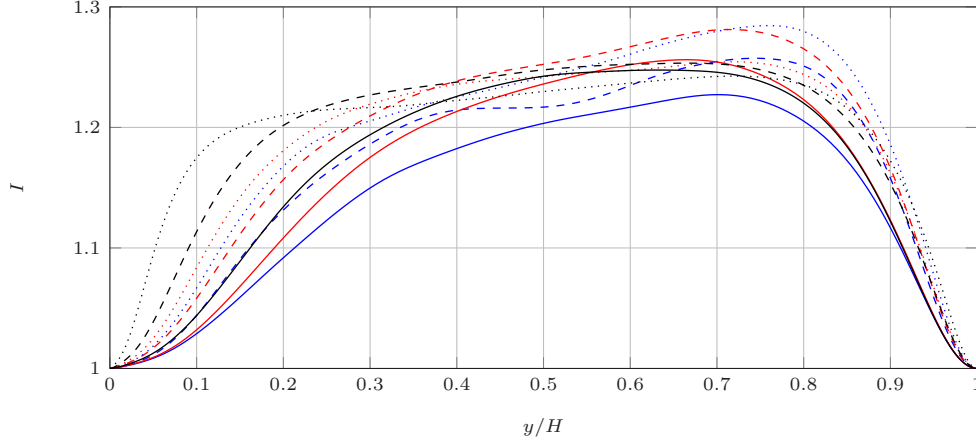
Figure 5.8: Vertical profiles of the Reynolds stress anisotropy function $I = \frac{\overline{\langle u'u'+v'v'+w'w'\rangle}}{\langle u'u'+w'w'\rangle}$ for —— G01, - - - G02, $\cdots\cdots$ G03, —— G04, - - - G05, $\cdots\cdots$ G06, —— G07, - - - G08 and $\cdots\cdots$ G09.

	G01	G02	G03	G04	G05	G06	G07	G08	G09
$(H-\delta_{SI})/H$	0.7034	0.7397	0.7573	0.6666	0.7102	0.7208	0.6327	0.6651	0.7226
u_∞	0.0711	0.0663	0.0589	0.0696	0.0610	0.0631	0.0718	0.0669	0.0621
L_∞	-	-	-	1.0626	1.0550	1.6246	1.0121	1.8457	1.8992
Re_T	-	-	-	425	515	1025	465	1581	2833

Table 5.2: Definition of the turbulent Reynolds number for the simulations listed in table 5.1, $Re_T = 2L_\infty u_\infty/\nu$. δ_{SI} defines the position of the maximum of the Reynolds stress anisotropy function $I = \overline{\langle u'u' + v'v' + w'w'\rangle}/\langle u'u' + w'w'\rangle$. The quantities are computed at the vertical position corresponding to the boundary layer thickness δ_{SI}.

[2012]. Therefore, the conclusions of Nagaosa and Handler [2012] are limited to high diffusivity substances disperse in flows without any influence of large scale motions and the minimum Reynolds number considered in Moog and Jirka [1999] was still a moderate value ($Re_\tau \simeq 400$).

In the two-regime model proposed by Theofanous et al. [1976], the turbulent Reynolds number $Re_T = u_\infty 2L_\infty/\nu$ is used as a measure of turbulence characteristics that is independent on the way that turbulence is generated, e.g. by wind-shear, bottom-shear, or buoyancy. In the present thesis, the surface influenced layer δ_{SI} is defined as the depth at which the maximum of Reynolds stress anisotropy function $I = \overline{\langle u'u' + v'v' + w'w'\rangle}/\langle u'u' + w'w'\rangle$ lies. Figure 5.8 depicts the vertical profile of the aforementioned quantity that defines undoubtedly the position at which v_{rms} deviates toward 0 for every simulation performed. Once δ_{SI} was defined, u_∞ and L_∞ were chosen to be $u_{rms}(\delta_{SI})$ and $L^x_{uu}(\delta_{SI})$, respectively. The values of u_∞, L_∞ and Re_T obtained in the present simulations are summarized in table 5.2. The two-regime model applies the large eddy renewal model [Fortescue and Pearson, 1967] to low Reynolds numbers flows and the small eddy renewal model [Banerjee et al., 1968, Lamont and Scott, 1970] only to high Reynolds numbers. As can be seen in figure 5.7c and table 5.2, the present data that fall above the critical $R_T = 500$ suggested by Theofanous et al. [1976] shows very good agreement with the small-eddy model, which can be written as $\frac{K_L}{u_\infty} = a \, Re_T^{-0.25} Sc^{-0.5}$. Moreover, the use of Re_T allows to compare the present open channel results with those of isotropic turbulent driven flow mass transfer. The constant of proportionality found from linear regression for simulations with $Re_T \geq 515$ (0.3541) agrees well with the value 0.3425 used in Herlina and Wissink [2019]. The present results support the applicability of the small eddy model in open channel flow for
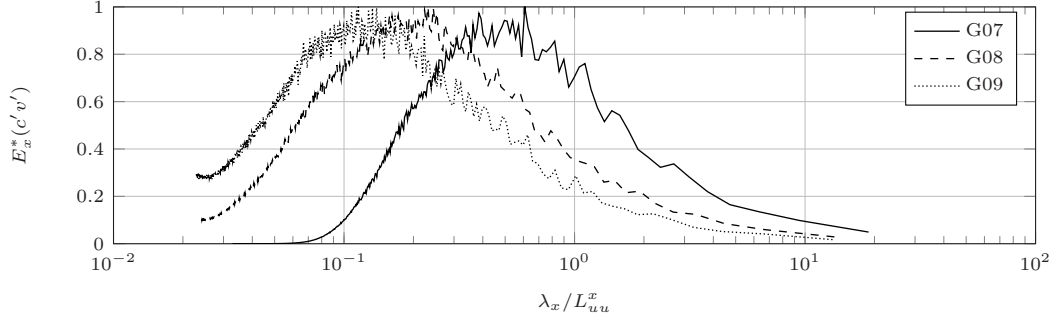
Figure 5.9: Averaged normalized pre-multiplied spectral density of the turbulent mass flux j_t ($E_x^*(c'v') = $ $k_x E_x(c'v')/(k_x E(c'v'))_{max}$) at $(H - y)/\delta = 5$. The domain size of all the results shown is $24H \times H \times 6H$.

$240 \leq Re_\tau \leq 630$ and Schmidt numbers ranging from 4 to 200. The domain sizes considered to compute Re_T allow to capture the large scale motions typical of moderate Reynolds numbers turbulent open channel flows.

The above is further confirmed by evaluating the pre-multiplied time-averaged spectral density of the turbulent mass flux $j_t = c'v'$ at a distance of 5δ from the surface. Figure 5.9 shows the normalized pre-multiplied spectra as a function of the normalized wavelength λ_x/L_{uu}^x. It can be seen that in all three cases, high-energy values were found at wavelengths significantly smaller than the integral length scales. Also, as expected, the peaks tend to move towards smaller scales at higher turbulence levels (from $\lambda_x/L_{uu}^x \simeq 0.6$ for $Re_\tau = 200$ to 0.1 for $Re_\tau = 630$). The shown spectra confirms the predominant importance of small scales to interfacial mass transfer in turbulent open channel flow for $Re_T > 500$.

5.4 Surface divergence and mass transfer

Starting from the applicability of the SDM developed by McCready et al. [1986], this section analyzes the correlation between mass transfer velocity and surface divergence $\rho(k_l, \beta)$ and the mechanisms linking them. Different values for $\rho(k_l, \beta)$ were found in regions with different flow characteristics instantaneously. This was quantified with conditional averaging.

5.4.1 Correlation between surface divergence and mass transfer

Previous studies showed that surface divergence model $K_L = \phi\sqrt{\beta_{rms}D}$ [McCready et al., 1986] generally provides a good prediction of the mass transfer velocity [Herlina and Wissink, 2019, Kermani et al., 2011, Nagaosa and Handler, 2012, Sanjou et al., 2017]. The approximately linear variation of $K_L/(U_b\sqrt{D})$ with $\sqrt{\beta_{rms}H/U_b}$, shown in figure 5.7d, confirms that the surface divergence model performs reasonably well also when applied to the present simulations. Previous numerical studies found the constant of proportionality for the SDM to be $0.41 \leq \phi \leq$ 0.46 for $1 \leq Sc \leq 8$ and $150 \leq Re_\tau \leq 600$ [Kermani et al., 2011, Nagaosa and Handler, 2012] in open channel flow. The present result $\phi = 0.455$ extends the validity of this range to $Sc = 200$ and $Re_\tau = 630$.

Herlina and Wissink [2019] found that, despite the good average correlation between β and k_l, this value tends to deteriorate with Re_T for interfacial mass transfer driven by isotropic turbulence. In contrast, in the present simulations $\overline{\rho(k_l, \beta)}$ was found to increase when higher turbulence levels were considered.

(a) Correlation as a function of the Schmidt number for simulations G07, G08 and G09.

(b) The Schmidt number was $Sc = 8$ for the small domain simulations, while 7 for the others. The data from NH12 have $Sc = 1$.

(c) Results from the large domain size simulations G07, G08 and G09. The correlation decreases with higher Schmidt numbers, when Re_T is constant.

Figure 5.10: Average correlation between mass transfer velocity k_l and surface divergence β as a function of Sc, Re_b and Re_T. HW19 and NH12 represent the data from Herlina and Wissink [2019] and Nagaosa and Handler [2012], respectively. The correlations are computed from simulations × G01, + G02, ● G03, × G04, + G05, ● G06, × G07, + G08, ● G09.

Figure 5.10a shows that the correlation decreases when lower diffusivities are considered. For $Sc = 1$ momentum and scalar diffusivity are identical and the correlation is not influenced by differences in diffusive time scales. When higher Schmidt numbers are considered, the time scale of the scalar becomes larger than their flow counterpart and, consequently, a lower correlation between the two quantities is expected. In the same way, a decrease in the correlation coefficient can be expected when higher turbulent levels are considered, due to the decrease in the diffusive time scale of the flow field, as proposed by Herlina and Wissink [2019]. On the contrary, for open channel flow, simulations at fixed Schmidt numbers indicate that the correlation increases with the Reynolds number and reaches a plateau for $Re_b \geq 6400$. Figure 5.10b depicts the time-averaged correlation between the instantaneous mass transfer velocity k_l and surface divergence $\beta = -\partial v/\partial y$, combined with results from Nagaosa and Handler [2012]. The correlation obtained from all simulations is shown as a function of Re_b. When increasing the Reynolds number, a slight increase in $\overline{\rho(k_l, \beta)}$ was observed in both present and Nagaosa and Handler [2012]'s data.

(a) G07 slice over a low speed region.

(b) G07 slice over a high speed region.

(c) G09 slice over a low speed region.
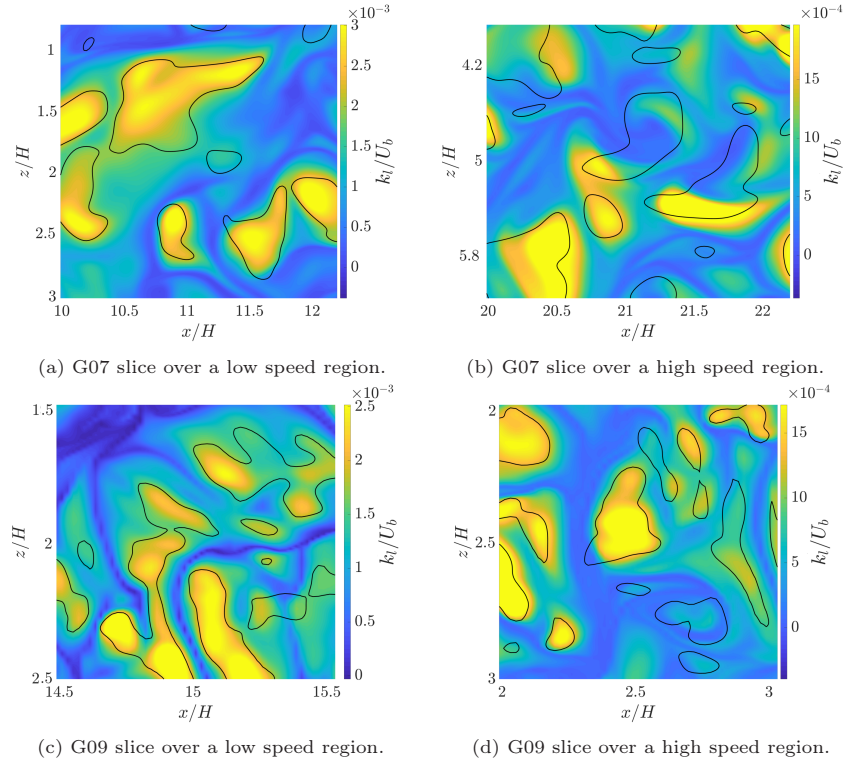
(d) G09 slice over a high speed region.

Figure 5.11: Comparison of top plane ($y/H = 0.9994$) slices of G07 (top panes) and G09 (bottom panes) over low (left panes) and high (right panes) velocity regions. The colorbars represent normalized mass transfer velocity k_l, while the black iso-lines depict $\beta' = \sigma(\beta')$. The correlation between k_l and β for the shown regions were found to be 0.8106 for G07 and 0.8754 for G09 in the low velocity region, while 0.4484 for G07 and 0.6557 for G09 in the high velocity region.

The higher values for the correlations computed in the cited paper are probably due to the low Schmidt number considered ($Sc = 1$), as explained above.

Figure 5.10c depicts $\overline{\rho(k_l, \beta)}$ as a function of the turbulent Reynolds number, combined with results from Herlina and Wissink [2019]. The values for $\overline{\rho(k_l, \beta)}$ found in the present thesis and in Nagaosa and Handler [2012] for open channel flow were slightly lower than the ones reported by Herlina and Wissink [2019]. It can be seen that, in isotropic turbulence driven flows, initially the correlation $\overline{\rho(k_l, \beta)}$ gradually reduces with increasing Re_T to reach a plateau around $\rho \approx 0.79$. In contrast, in the large-box simulations (G07, G08, G09) the correlation $\rho(k_l, \beta)$ was observed to improve slightly with Re_T. This can be explained considering that, while in isotropic turbulence driven flows only upwelling and downwelling motions can cause high and low divergence regions at the surface, in open channel flows, more complex structures modify the path of vertical scalar transport, e.g. LSM and VLSM. Therefore, in the latter case, anisotropic coherent structures seem to disturb the vertical motions reducing the overall correlation compared to isotropic turbulence driven flow.

Figures 5.11 shows zoomed instantaneous snapshots of k_l over regions of low and high velocity at the surface for simulations G07 and G09. Since the streamwise integral length scale of β scales with the Reynolds number, as depicted in figure 5.12, the area of the zoomed region was chosen to be $15L_{\beta\beta}^x \times 15L_{\beta\beta}^x$, such that the size of the structures looks similar in the pictures, even if the Reynolds number is different. In figure 5.11, the regions with high surface divergence, highlighted with black iso-lines, show a qualitative higher correlation when the zoomed area lies above a low speed streak. The instantaneous correlations computed for each snapshot confirm this qualitative observation. In fact, while the correlation between k_l and β in figures 5.11a and
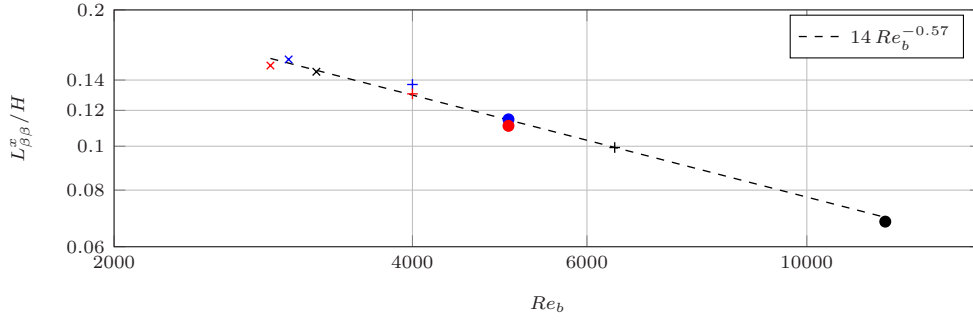
Figure 5.12: Streamwise integral length scale of the surface divergence at the surface as a function of the bulk Reynolds number. The symbols represent: × G01, + G02, ● G03, × G04, + G05, ● G06, × G07, + G08, ● G09.

Run	high-speed		low-speed		
	A_h	$\overline{\rho_h(k_l, \beta)}$	A_l	$\overline{\rho_l(k_l, \beta)}$	$\overline{\rho(k_l, \beta)}$
G07	0.154	0.578	0.151	0.780	0.6880
G08	0.154	0.623	0.157	0.786	0.7197
G09	0.154	0.640	0.156	0.787	0.722

Table 5.3: Averaged surface fraction area (A_h, A_l) and correlation coefficient ($\overline{\rho_h(k_l, \beta)}$, $\overline{\rho_l(k_l, \beta)}$) over high and low speed regions and total averaged correlation coefficient $\overline{\rho(k_l, \beta)}$ for different Reynolds numbers. The high and low speed streaks were chosen such that $u' > \sigma(u')$ and $u' < -\sigma(u')$, respectively. $\sigma(*)$ is the standard deviation of the quantity $*$ over the whole mean plane.

5.11c were found to be 0.8106 and 0.8754, respectively, the correlations for figures 5.11b and 5.11d were almost half, with values of 0.4484 and 0.6557.

Table 5.3 shows that the averaged correlation $\overline{\rho(k_l, \beta)}$ was markedly higher in the low-speed regions ($u' < -0.5\sigma(u')$) than in the high-speed regions ($u' > 0.5\sigma(u')$). Furthermore, while $\overline{\rho_l(k_l, \beta)}$ was found to be approximately independent of Re_T, the correlation was found to increase with Re_T in the high-speed regions. The latter causing the observed overall increased correlation with Re_T.

5.4.2 Role of surface attached and parallel vortices in mass transfer

The aforementioned increased correlation was linked to the distribution of surface parallel vortical structures (SPVS) close to the surface. Figure 5.13 depicts a 3D view of simulation G07. The view captures the domain from the top and the iso-surface represents vortices at $y/H \geq 0.9$ through the Q-criterion (equation 4.12) with a threshold of $Q = 0.1$. In order to highlight the direction of rotation, the iso-surface is colored with the instantaneous vertical velocity fluctuation v', where black and white coloring depict downward and upward motions, respectively. The color-lines representing the instantaneous mass transfer velocity k_l for $Sc = 200$ lie at $y/H = 0.9997$, the last vertical point of the computational mesh. Figure 5.13 shows the effect of surface attached and aligned vortices on mass transfer. Surface aligned vortices are arranged in ring-like shapes, in which the upwelling part faces the center of the structure, white in the figure. The group of vortices forms a closed upwelling region and, once the fluid with low concentration in the bulk of the channel enters this motion, it is dragged toward the surface. The kinetic energy contained in the vertical motion is converted in streamwise and spanwise velocities at the surface, due to the presence of the boundary. Therefore, once this motion impacts the surface, it creates high surface divergence that will push the saturated fluid outside
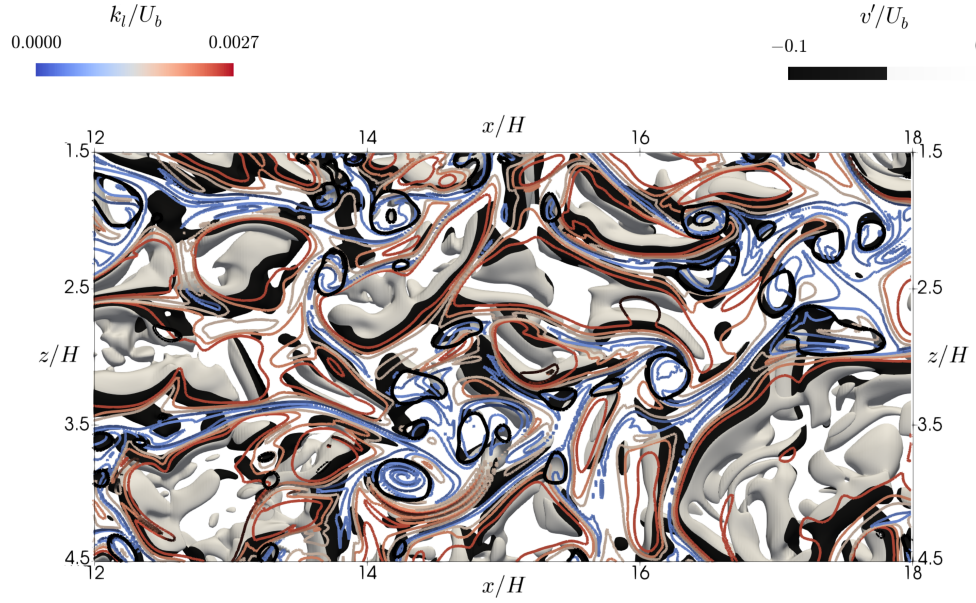
Figure 5.13: Top view of simulation G07 for $Sc = 200$. The colored iso-lines represent the mass transfer velocity at the surface. The iso-contours colored with v' represent vortices at $y/H \geq 0.9$ through the Q-criterion with a threshold of $Q = 0.1$.

of the region. Therefore, these SPVS typically contribute to a good correlation $\overline{\rho(k_l, \beta)}$. As a consequence of this motions, the concentration around these ring-like vortices is very high. Downwelling motions preserve the equilibrium of the flow and bring down the old saturated fluid at the surface, thickening the scalar boundary layer and reducing mass transfer locally. Hence, the mass transfer velocity in convergence zones is usually low, blue in the picture. Qualitatively looking at the picture, it is possible to observe that surface attached vortices mostly lie in low k_l regions and seem to accumulate saturated fluid in one point.

Nagaosa and Handler [2003] described surface attached and aligned vortices as the final stage of the deformation of hairpin vortices coming from below and interacting with the surface. Hairpin-like coherent vortices produced near intense Q2-events at the wall were found to advect toward the surface and deform either aligning the head with the surface or splitting themselves in two legs that attach to it.

Figure 5.14 depicts the position of surface attached and parallel vortical structures visualized with $Q = 0.1$ compared to high and low mass transfer velocity regions. The slices are taken at 5δ from the surface and are colored with instantaneous normalized mass transfer velocity k_l. It can be observed that surface aligned (attached) vortices mostly lie over high (low) k_l regions. The aforementioned mechanism seems to be quite stable, since both figures 5.14a and 5.14b show the same vortical distribution, even though the bulk Reynolds number for simulation G09 is almost four times larger than for simulation G07.

Figure 5.15 depicts 3D views of simulations G07 and G09. As in figure 5.14, the vortices are underlined with $Q = 0.1$, while they are colored with the streamwise velocity fluctuation u'. The slices are taken at 5δ from the surface and colored with the instantaneous streamwise velocity fluctuation u'. A comparison of figure 5.15a and 5.15b shows that, for low Re_b, SPVS are mainly present near low-speed regions, while for larger Re_b this distribution was observed to become more uniform (possibly due to increased mixing). As a result, $\overline{\rho(k_l, \beta)}$ is expected to increase inside the high-speed regions, and hence overall, when higher Reynolds numbers are considered. This is confirmed in the result of the quantitative analysis depicted in table 5.3.

(a) G07: $Re_b = 3200$.

(b) G09: $Re_b = 12000$.

Figure 5.14: 3D snapshots for simulations G07 and G09. Vortices are visualized through the Q-criterion, with a threshold of $Q = 0.1$, colored with instantaneous mass transfer velocity k_l. The slice lies at $(H - y)/\delta = 5$ and is colored with the instantaneous interfacial mass transfer velocity k_l.

5.4.3 Effect of streaky structures on local mass transfer

Figure 5.16 shows contour plots of time-averaged streamwise velocity fluctuations $\overline{u'}$ and mass transfer velocity $\overline{k_l}$ at $y/H = 0.9997$ for simulations G07, G08 and G09. The average was performed in time and considering a frame moving with a speed equal to the average stream-wise velocity in that plane. The average was performed over the time windows presented in table 5.1. The contour plots indicate footprints of very large structures present in the simulations with $Re_\tau \geq 365$, confirming the observations depicted in chapter 4. As opposed to isotropic turbulence driven flow, the high and low velocity regions in open channel flow are organized in streaks. Moreover, upwelling and downwelling motions seems to be linked to the presence of LSM and VLSM, since the low and high $\overline{k_l}$ regions seems to have a coherent shape. For $Re_\tau = 630$, more high mass transfer velocity regions can be spotted over high velocity regions compared to G08 and, particularly, G07. This confirms that more divergence areas are

(a) G07: $Re_b = 3200$
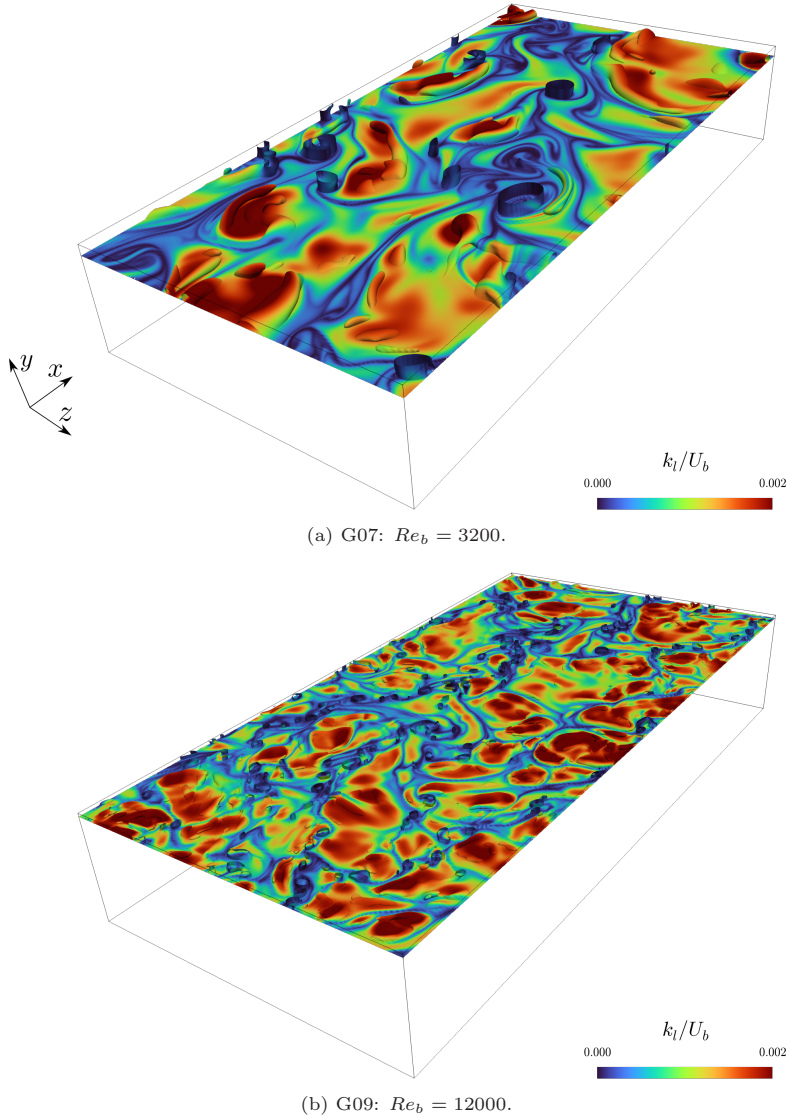

(b) G09: $Re_b = 12000$
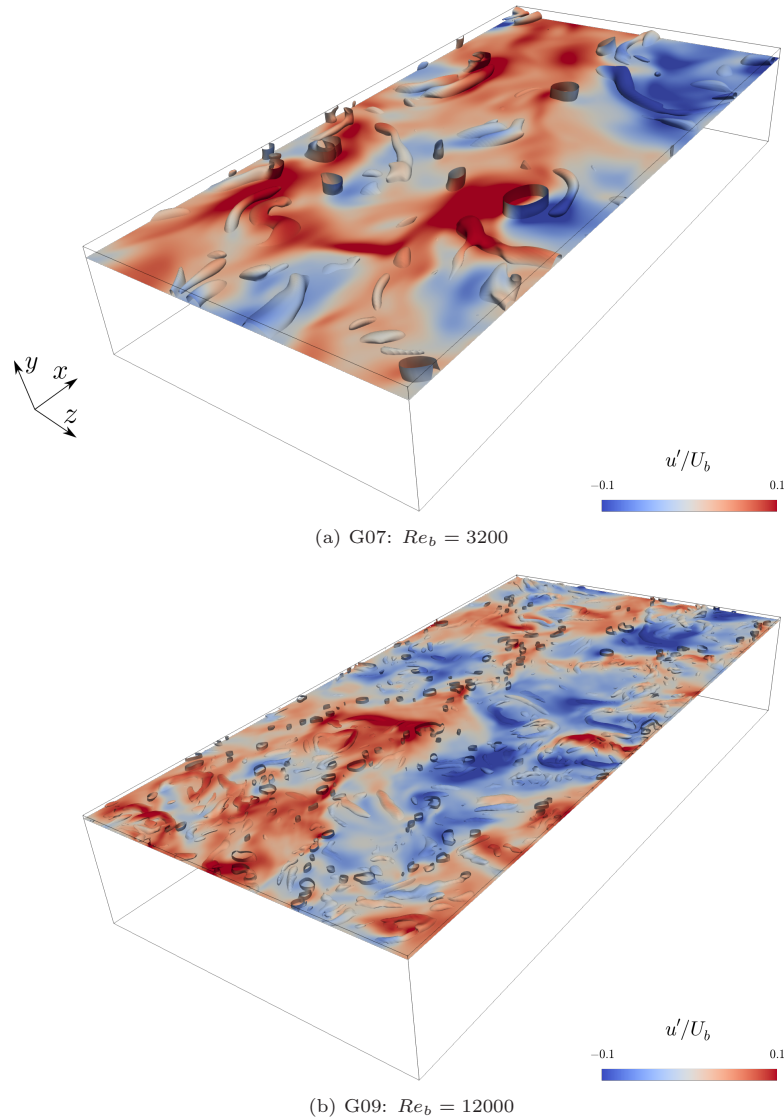
Figure 5.15: 3D snapshots for simulations G07 and G09. The vortices are visualized through the Q-criterion, with a threshold of $Q = 0.1$, colored with instantaneous streamwise velocity fluctuation u'. The slice lies at $(H - y)/\delta = 5$ and is colored with the instantaneous streamwise velocity fluctuation u'.

present when higher turbulence levels are considered, as qualitatively observed in the previous sub-section.

5.5 Effect of vortical structures on mass transfer

The present section is based on the theoretical "chain saw model" proposed by Moog and Jirka [1999]. Here, a visual confirmation of the model is given that helps to explain the mechanisms described in this chapter.

Figure 5.17 depicts the streamwise spatial average of the streamwise velocity fluctuation $\langle u' \rangle_x$ for G07, G08 and G09. As underlined in section 4.3.3, the velocity vectors confirm the collapse of downwelling regions and high velocity streaks. This effect is stronger for the higher Reynolds numbers considered, where the vortices span the whole domain length, but it is still visible for $Re_\tau = 200$. Moreover, the black iso-lines representing constant concentrations show that, due

(a) G07: $Re_\tau = 200$.

(b) G08: $Re_\tau = 365$.

(c) G09: $Re_\tau = 630$.
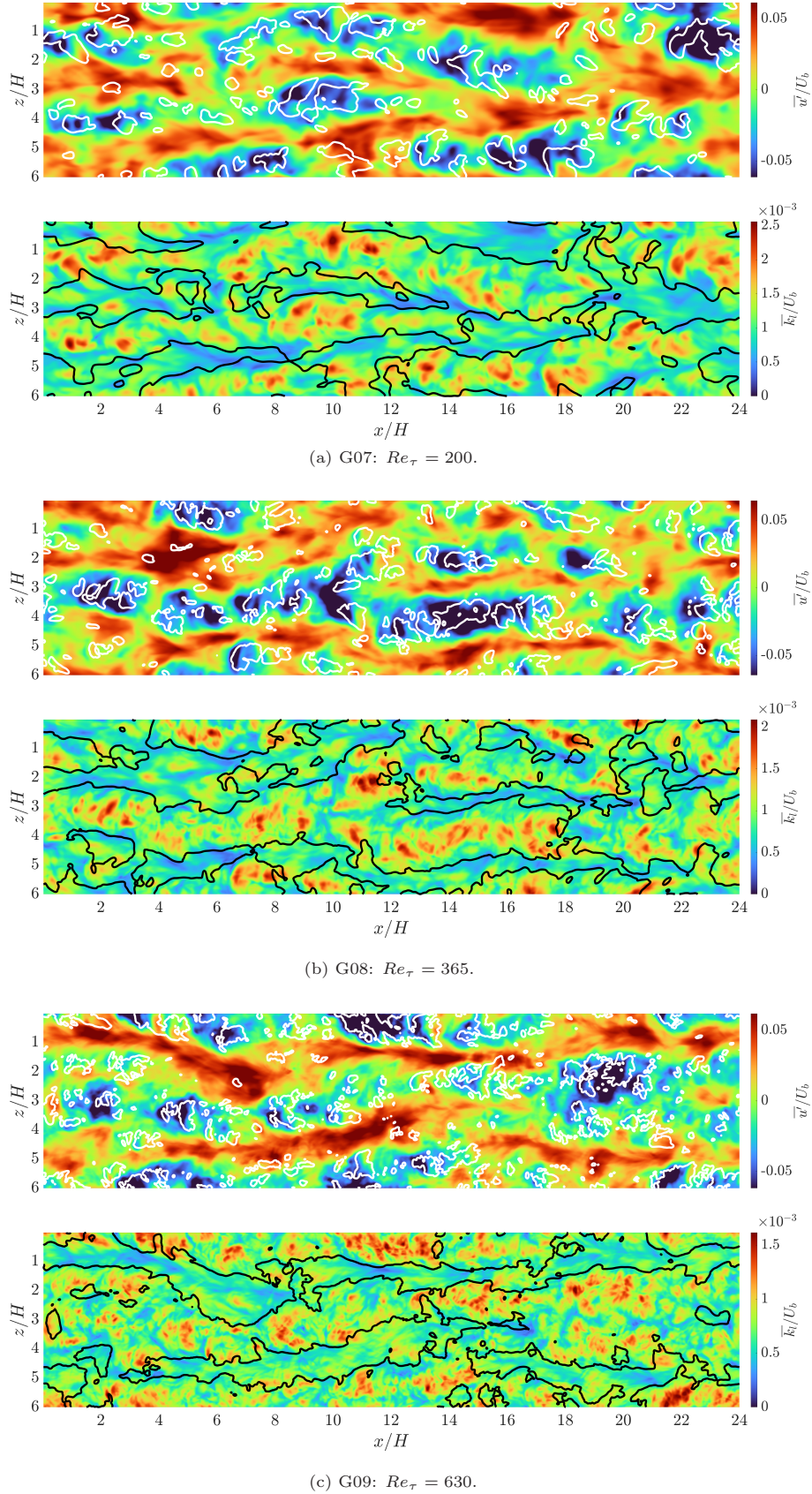
Figure 5.16: Contour plots of time-averaged streamwise velocity fluctuation $\overline{u'}$ and mass transfer velocity $\overline{k_l}$ at $y/H = 0.9997$ for simulations G07, G08 and G09. Averaging was performed on the time window defined in table 5.1 by considering a coordinate system which moved as fast as the mean streamwise velocity at $y/H = 0.9997$. The white and black iso-lines represent $\overline{k_l} = K_L + \sigma(\overline{k_l})$ and $\overline{u'} = \sigma(\overline{u'})$, respectively.

(a) $Re_\tau = 200$.

(b) $Re_\tau = 365$.

(c) $Re_\tau = 630$.
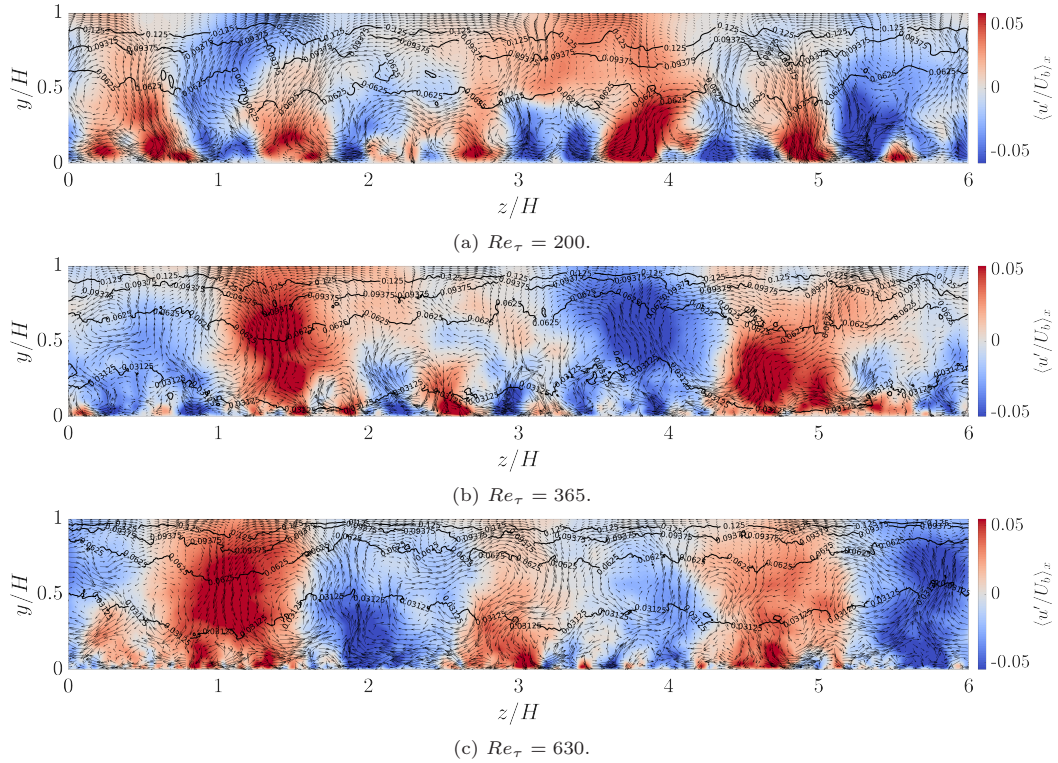
Figure 5.17: Contour plots of streamwise velocity fluctuation averaged over the whole streamwise dimension at $t/t_b \simeq 64$ for simulations G07, G08 and G09. Black iso-lines represent concentration levels averaged over the whole streamwise direction, while the black arrows represent the velocity vectors in the plane averaged over the whole streamwise dimension.

to this upward (downward) motions, the near concentration gradient becomes steeper (milder) in low (high) velocity streaks, confirming what observed above. Therefore, it can be assumed that the rotation of the streamwise aligned large structures creates upwelling and downwelling regions that bring the small vortices from the bulk of the channel to its surface. It is clear from the figure that the size and the strength of these structures increase with Reynolds number. In fact, while the size of the streamwise aligned vortices reaches at most $0.5H$ for G07, in G08 and G09 the blue and red regions cover the whole vertical extension of the domain. Moreover, the large vortices for $Re_\tau \geq 365$ strongly modifies the depth reached by the scalar, while in figure 5.17a only marginal oscillations due to the flow motions can be observed. At the interface, the small vortices brought up by the rotation of the large streamwise aligned structures actively enhance mass transfer and this is the reason why spectral analysis (cf. section 5.3) showed that the scales of motions that have an active role in mass transfer are the small scales. This should not mislead to think that only these scales are important, since without the large scale motions that increase the exchange of fluid parcels from the bottom to the top of the channel, turbulent mass transfer would be hindered.

6 Pollutant transport

In the past centuries, the aggregation of small villages into larger urban centers started a rise in devastating epidemics due to problems in sewage disposal and supply of clean drinking water. In the nineteenth century, with the increase in size of cities due to industrialization, the spread of diseases and infections became a major problem. In 1854, physician John Snow linked the spread of cholera to the contaminated drinking water supply [Walters, 2013]. His intuition started the development of the, so called, wastewater treatment facilities. During the last century, the research in this direction have significantly reduced the incidence of wastewater diseases in developed countries. At the present day, surface water contamination due to point loadings, such as combined sewer overflows, is one of the major cause of surface water pollution in developed countries [Walters, 2013]. During a strong rainfall event, urban sewage can overflow, leading to discharge of contaminated water into streams. These pollutants usually contain harmful pathogens like Salmonella, Legionella, hepatitis A, polioviruses, entamoeba histolytica. Since measurements of the contamination level for each pathogen is practically impossible, researchers usually test the water for coliform group of bacteria that were found to be an indicator of the presence of this pathogens, fecal indicator bacteria (from now on FIB) [Thomann and Mueller, 1987]. These microorganisms are accustomed to life in human or animal bodies where nutrient levels are high and the temperature is constant and approximately $37°$ C. Once FIB enter the streaming water body, several mechanisms will reduce the population, until extinction, strongly reducing their long-term survival. A different temperature between bacteria and water will cause buoyancy effects that strongly affect the distribution of the pollutant. Moreover, the natural bacterial death rate is increased by inactivation caused by the penetration of sun light in the water body and, once the bacteria are mixed by turbulent processes, possibly by the presence of oxygen in the water. The latter activates bacteria's metabolism which decreases their life-time.

This chapter presents DNSs of pollutant transport in open channel flow. Figure 6.1 depicts a schematic of the problem under consideration, while the set up of the simulations was presented in chapter 3 (figure 3.1). All the simulations were performed for $\Delta t/t_b \simeq 100$, in order to simulate the first minutes in which the pollutant enters in water. The values averaged on the homogeneous planes x, z are represented by $\langle \cdot \rangle$, while the values averaged in time are represented by $\bar{\cdot}$. $\cdot^+$ represents averaged data normalized with viscous scales.

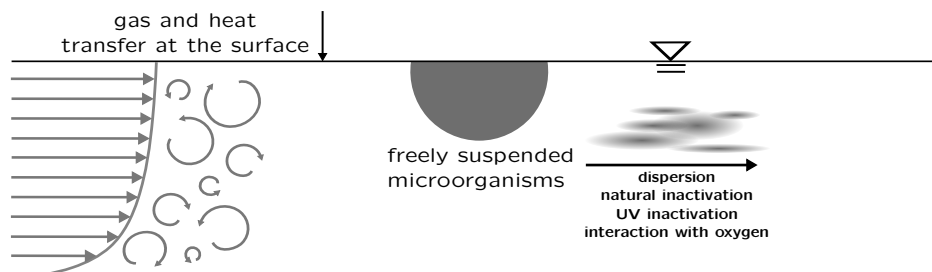Figure 6.1: Schematic of pollutant transport.

	L01	L02	L03	L04	L05	L06	L02B	L03B	L04B	L05B	L06B	L07B
$\mathcal{R}_{nat}$			✓	✓	✓	✓		✓	✓	✓	✓	✓
$\mathcal{R}_{UV}$		✓		✓	✓	✓	✓		✓	✓	✓	✓
$\mathcal{R}_{G}$			✓	✓	✓	✓		✓	✓	✓	✓	✓
Ri	0	0	0	0	0	0	-0.62	-0.62	-0.62	-0.62	-0.62	0.62
$c^*_{O_2,b}$	0	0	0	0	0.5	0.75	0	0	0	0.5	0.75	0

Table 6.1: Summary of parameter sensitivity analysis simulations. $\mathcal{R}_{nat}$ is the bacterial natural decay rate, $\mathcal{R}_{UV}$ is the bacterial UV-inactivation rate, $\mathcal{R}_G$ is the decay rate due to the higher metabolism triggered by the presence of high oxygen concentrations, Ri is the Richardson number (equation 6.2) and $c^*_{O_2,b} = c_{O_2,b}/c_{O_2,s}$ represents the normalized concentration of oxygen present in the bulk of the channel at time $t/t_b = 0$. All the values chosen for the decay rates were presented in chapter 3. The grid resolution is $192 \times 192 \times 128$, the domain size $3H \times H \times 3H$, the Reynolds number $Re_b = 3000$ and the Schmidt number 7 for the bacteria and 4 for oxygen for all the simulations in the table. For each case two different initial conditions for the bacteria were considered, a cloud (half sphere with a radius of $0.45H$) near the surface of the channel and a thin ($0.02H$ thick) homogeneous layer just below the surface.

The first section analyzes the role of the different decay rates considered in the present study, to define which of them are negligible. In the second section, the mass of bacteria was approximated with the one dimensional model presented in section 2.3.1 and the results compared with the data of the parameter sensitivity analysis simulations. The third section considers the effect of simulating FIB with different Schmidt numbers. In the end, a comparison between averaged and instantaneous quantities enlightens the impact that spatial heterogeneities typical of turbulent flows have on pollutant transport.

6.1 Parameter sensitivity analysis

In the pollutant transport simulations, the concentration fields of bacteria and dissolved gas (oxygen) were coupled through the first-order reaction terms $\mathcal{R}_{O_2}$ (oxygen consumption rate) and $\mathcal{R}_B$ (bacterial decay rate). The values used for the decay rates were recommended by the Engler-Bunte-Institut of KIT and were described in section 3.1. The Schmidt numbers chosen for representing the bacteria and dissolved oxygen were first set to $Sc = 7$ and $Sc = 4$, respectively. Even though these Sc are significantly lower than the realistic Schmidt numbers for E. Coli bacteria ($Sc \simeq \mathcal{O}(10^3)$) and dissolved oxygen in water ($Sc \simeq 500$), the combination between them was chosen such that the resulting Schmidt number ratio was similar to the realistic one. The simulations employed to perform the parameter sensitivity analysis are summarized in table 6.1. All simulations were started from the exact same turbulent flow field and all the simulations parameters were kept constant, in order to provide a fair comparison between all cases. In order to compare the different reaction rates, the total mass of bacteria was computed as follows:

$$m_B = \sum_{i=0}^{n_x} \sum_{j=0}^{n_y} \sum_{k=0}^{n_z} c_B(i,j,k). \tag{6.1}$$

In the pollutant transport simulations in which the released wastewater discharge had a different density (temperature) than the ambient fluid, the temperature equation affects the Navier-Stokes equations, causing buoyancy currents.

As illustrated in figure 6.2 two different initial conditions of wastewater discharge were considered. In the first case a cloud (half sphere with a radius of $0.45H$) of freely-suspended bacteria was released near the surface of the channel, while in the second scenario a thin ($0.02H$ thick)

(a) $t/t_b = 0.1$

(b) $t/t_b = 0.1$

(c) $t/t_b = 38.5$

(d) $t/t_b = 38.5$

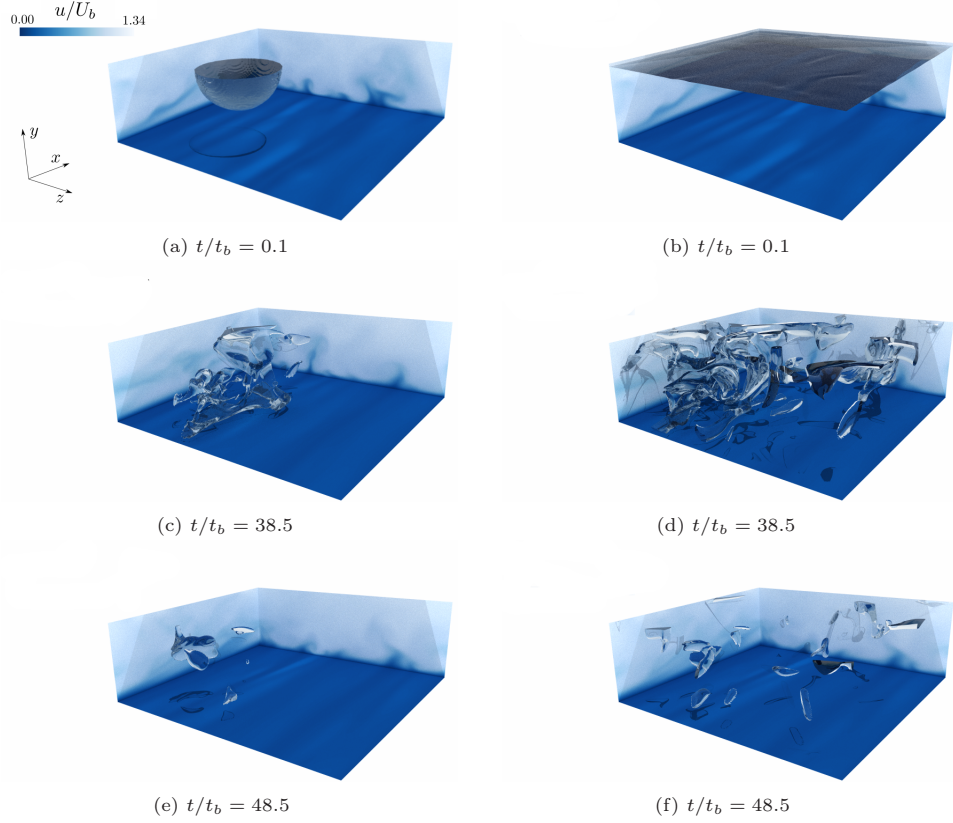(e) $t/t_b = 48.5$

(f) $t/t_b = 48.5$

Figure 6.2: Time evolution of a blob (a, c and e) and a layer (b, d and f) of freely-suspended bacteria in open-channel flow shown as iso-surfaces of $c_B = 0.1$. The snapshots are taken from simulations L04.

homogeneous layer of freely-suspended bacteria near the surface was discharged. As can be seen in figures 6.2a to 6.2d, during a short initial period after the release the bacterial distribution varies between the two cases and hence, a different interaction between bacteria and dissolved oxygen concentration can be expected. After typically about 50 bulk time units, in both cases, the bacteria distributions become similar, as observed in figures 6.2e and 6.2f.

To study the effect of UV-inactivation upon the removal of bacteria, simulations with and without $\mathcal{R}_{UV}$ were performed. After a relatively short time, the effect of UV-inactivation became observable. The decrease of the total mass of bacteria present in the domain is much faster when $\mathcal{R}_{UV}$ is active, as figure 6.3a clearly shows. In fact, a difference of $\simeq 8\%$ is observable already at $\simeq 100$ bulk time units after the discharge.

It is likely that density differences (e.g. due to temperature differences) occur between the river water and the pollutant discharged into the river. Even very small relative density differences are expected to alter the flow field significantly and consequently the pollutant transport and/or its decay rate. Figure 6.4 depicts the effect that buoyancy has on a blob of pollutant. The Richardson number is defined as the ratio between buoyancy and the flow shear terms:

$$Ri = \frac{g c_\beta \Delta T H}{u_b^2}, \tag{6.2}$$

where g is the gravitational acceleration considered to act in the y directiont and $\Delta T = T_{b,0} - T_{B,0}$ is the difference between the initial temperature of the ambient fluid $T_{b,0}$ and the initial temperature of the pollutant $T_{B,0}$. Note that by assuming $g = -9.81\,\mathrm{m/s^2}$, $c_\beta = 0.000207\,\mathrm{K^{-1}}$ and $H = 0.1\,\mathrm{m}$, the cases $Ri = \pm0.62$ represent cases with $\Delta T \approx \pm2.75\,\mathrm{K}$. For $Ri = 0$ the

(a) Simulations with and without $\mathcal{R}_{UV}$ activated.

(b) Simulations with positive, neutral and negative buoyancy. In all the simulations $\mathcal{R}_{UV}$ was active.

(c) Simulations with 0% and 75% percent of oxygen concentration in the bulk. In both simulations all the decay rates were active.
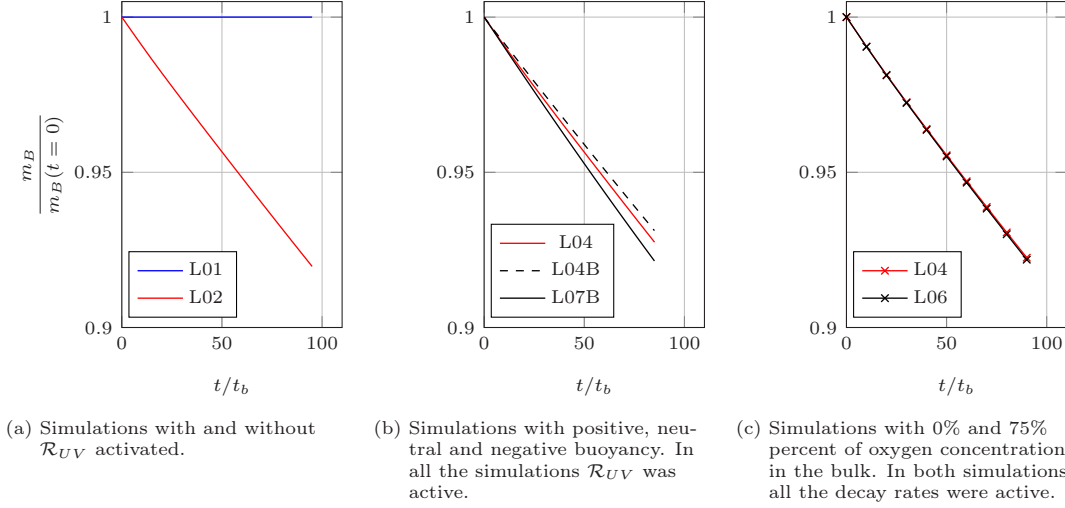
Figure 6.3: Decrease of the total mass of bacterial concentration due to UV-inactivation, buoyancy and oxygen concentration in the bulk. The total mass is normalized by the total initial mass. The simulations considered here are the ones in which the bacteria were introduced in the flow as a thin ($0.02H$ thick) layer just below the surface.
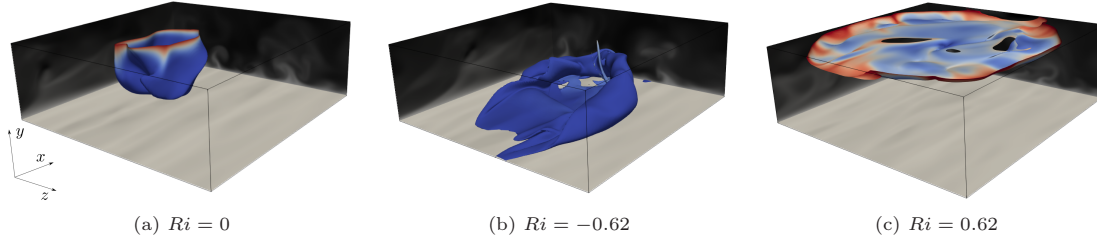

(a) $Ri = 0$

(b) $Ri = -0.62$

(c) $Ri = 0.62$

Figure 6.4: Instantaneous 3D snapshots representing the effect of buoyancy on pollutant concentration. The slices in background are colored with u'/U_b from low, white, to high, black. The iso-contour represents $c_B = 0.1$ and it is colored with c_G from low, blue, to high, red. The snapshots are taken from simulations L04, L04B and L07B at time $t/t_b = 30$.

blob maintains its shape and position in the time range shown in the figure. On the other hand, for $Ri = -0.62$ and the same amount of time, the blob sinks and lies on the bottom wall. In this position, the concentration of oxygen is very low, as denoted by the blue color of the iso-contour, and the action of the sunlight is weaker. When $Ri = 0.62$ is employed, the blob floats on the surface, where the concentration of oxygen is very high and the UV-inactivation really strong. Therefore, a faster (slower) decrease in the total mass of bacteria is expected when $Ri = 0.62$ ($Ri = -0.62$) is employed. The case with $Ri = 0$ should have a decay rate faster than $Ri = -0.62$ and slower than $Ri = 0.62$. Figure 6.3b shows the evolution of the total mass of bacteria with time for the aforementioned cases, where the initial difference in density corresponds to $\Delta T = \pm 2.75\,\mathrm{K}$ between the pollutant and the ambient water. The figure confirms quantitatively what was observed in figure 6.4. The bacterial decay rate in the case with negative buoyancy (pollutant temperature lower than water temperature and $Ri = -0.62$) is slower than in the other two cases, while, when buoyancy is positive, bacteria accumulates at the top of the channel, where the effect of $\mathcal{R}_G$ and $\mathcal{R}_{UV}$ are the highest, and, therefore, the total mass decreases much faster.

The overall decay rate of bacteria increases with increasing dissolved oxygen concentration in the water body. In fact, when oxygen is available, bacteria start their life cycle and their metabolism becomes faster. Since in the present thesis the growth mechanisms are not considered, a faster metabolism directly translates into a higher decay rate. To explore this effect

Parameter	$\Delta t/t_b$	difference [%]
$\mathcal{R}_{nat}$	99.3	0.03
$\mathcal{R}_{UV}$	96.2	7.5
$O_2\vert_b$	95.06	0.05
Ri	86.4	1.2
IC	98.2	0.2

Table 6.2: Results of the parameter sensitivity analysis. $\mathcal{R}_{nat}$ is the bacterial natural decay rate, $\mathcal{R}_{UV}$ is the decay rate due to UV-inactivation, $O_2\vert_b$ is the percentage of oxygen present in the bulk of the channel at time $t/t_b = 0$, Ri is the Richardson number and IC are the two different initial conditions employed, which can be a thin ($0.02H$ thick) layer just below the surface or a half sphere with radius $0.45H$ with the flat part collapsing with the surface.

| **Name**	Re_b	Sc	$L_x \times L_y \times L_z$	$N_x \times N_y \times N_z$
S01	3000	7	$3H \times H \times 3H$	$192 \times 128 \times 192$
S02	3000	28	$3H \times H \times 3H$	$384 \times 256 \times 384$
S03	3000	49	$3H \times H \times 3H$	$576 \times 384 \times 576$
S04	3000	100	$3H \times H \times 3H$	$768 \times 512 \times 768$
S05	2785	7	$12H \times H \times 3H$	$384 \times 128 \times 192$

Table 6.3: Computational parameters of simulations for the Schmidt number comparison and the heterogeneities analysis. Re_b is the bulk Reynolds number, L_x, L_y and L_z denote the size of the domain, H is the height of the domain, N_x, N_y and N_z are the number of grid points for the refined scalar mesh. The base mesh size employed for the flow field was the same as the scalar mesh for S01.

on the fate of bacteria in turbulent open-channel flow, simulations with different initial bulk oxygen concentrations $c_{O_2,b}$ were performed for the cases with and without buoyancy. Figure 6.3c compares the time evolution of the total mass of bacteria for $c^*_{O_2,b} = c_{O_2,b}/c_{O_2,s} = 0$ and $c^*_{O_2,b} = 0.75$, for the cases without buoyancy effects. At least in the range of the present simulation time, the effect of varying the bulk oxygen concentration was negligible. The main reason for this results can be the very low value of the bacterial decay rate due to oxygen consumption that is of the order of $\mathcal{O}(10^{-5})$. Moreover, the interaction between the two species usually happens in very small filaments where high concentration of oxygen and bacteria are present that cover only a small part of the total numerical volume. Even though a decrease due to this factor is present, its magnitude was found to be negligible compared to the other decay rates.

Table 6.2 summarizes the results of the parameter sensitivity analysis, showing that only UV-inactivation produced substantial modification to the bacterial concentration. Moreover, it was observed that $\mathcal{R}_{UV}$ is more effective when the pollutant is close to the surface. Since buoyancy affects the spatial distribution of the bacteria, the effect of temperature differences between the pollutant and the ambient fluid were found to be non-negligible.

6.2 Effect of Schmidt number and spatial heterogeneities

Even though bacteria have typically very low diffusivity in water and, consequently, a high Schmidt number $Sc = \mathcal{O}(10^3)$, for the above parameter sensitivity studies, it was assumed to be sufficient to perform simulations at a (low) $Sc = 7$ for the bacteria. However, when investigating the effect of instantaneous spatial heterogeneities, which are characteristic of turbulent open
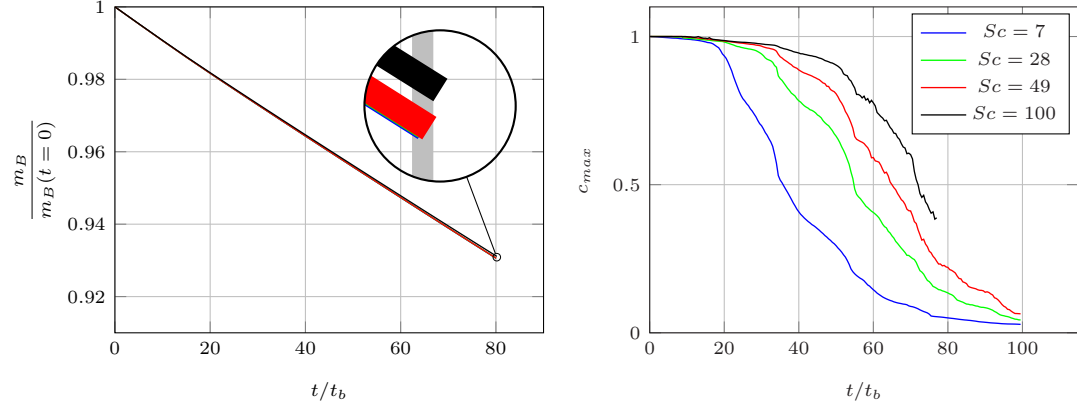
(a) Reduction of total bacterial mass over time for the different Sc cases. The total mass is normalized by the total initial mass. The zoomed circle magnifies 10 times the plot.

(b) Variation of maximum local concentration over time.

Figure 6.5: Results for the Schmidt number comparison. The simulations displayed are S01 ($Sc = 7$), S02 ($Sc = 28$), S03 ($Sc = 49$) and S04 ($Sc = 100$).

channel flow, it is necessary to evaluate further the influence of modelling the bacteria with different Schmidt numbers. To do so, four simulations (S01 to S04 in table 6.3) were performed, where the Schmidt number was varied between 7 and 100. In all simulations, the same initial flow field was used so that instantaneous one to one comparison could be done. As the results of the parameter sensitivity analysis (section 6.1) suggested, $\mathcal{R}_{nat}$ was dropped in the present simulations and the initial concentration of oxygen in the bulk of the channel was set to 0. Moreover, the pollutant initial condition was set to be a thin ($0.02H$ thick) layer at the surface, since the difference between the two tested conformations was found to be negligible. Because buoyancy alters the flow field, a Richardson number different than 0 would have hindered a one to one comparison between the bacteria modelled with different Schmidt numbers. A fifth simulation with a larger domain size was performed (S05), in order to determine the effect that spatial heterogeneities typical of turbulent flows have on pollutant distribution.

Figure 6.5a shows the decay of the total mass concentration for the different Schmidt numbers employed. The plot suggests that the Schmidt number variation has no significant effect upon the overall bacterial decay rate. When zooming-in very closely (figure 6.5a), however, there is an indication that the lower Sc cases decay faster compared to the higher Sc cases. One explanation might be the fact that UV-inactivation is the strongest near the surface. The scalar with higher diffusivity (low Schmidt numbers) will tend to spread faster in all direction and consequently cover a larger area near the surface in a shorter time, thus experiencing a stronger UV-inactivation effect than the higher Schmidt number cases. Still, one would conclude that the differences observed between these total mass concentration is too small to imply any important effect of the Schmidt number. On the other hand, evaluating and comparing instantaneous snapshots of the four cases highlight the influence of applying different Schmidt numbers to the bacterial concentration field, particularly during the initial transient regime. Figure 6.5b shows the variation of maximum concentration found in the domain over time. While the global average concentration remain similar for all the cases, the maximum concentration starts to deviate from one another. After a short period of time, the values for the higher Schmidt number cases remain large compared to the lowest Sc case (between 20% and 60% larger). This is also evident in Figure 6.6, where two top-plane snapshots of the bacteria modelled with $Sc = 7$ (left pane) and $Sc = 100$ (right pane), taken at the same time, are depicted. It can be
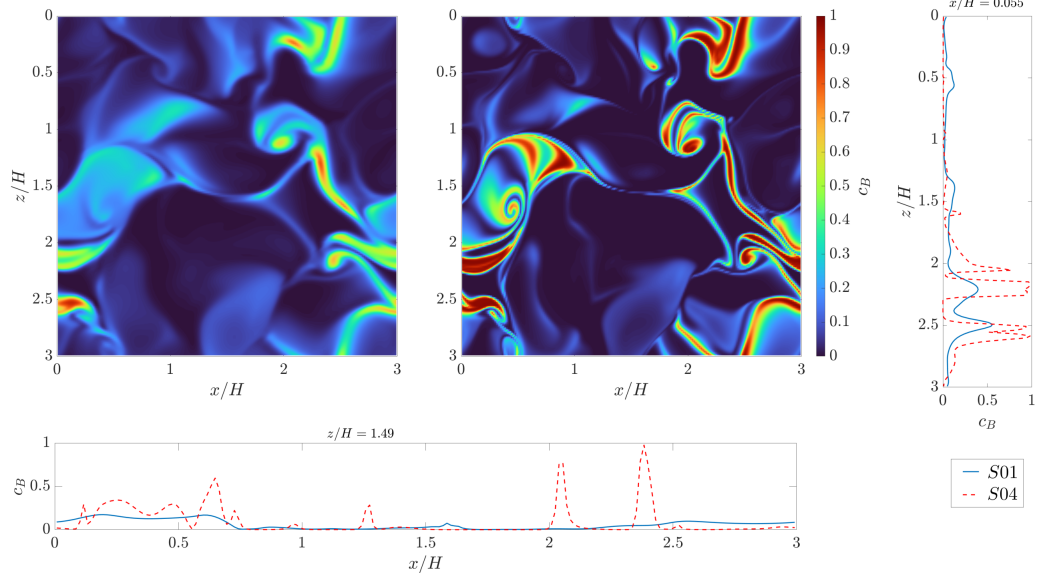
Figure 6.6: Comparison between the surface area covered by bacteria modelled with $Sc = 7$ and $Sc = 100$ at $t/t_b = 30$. The contour plots represent the concentration maps at $y/H = 0.998$. Also shown are the concentration profiles at $x/H = 0.55$ and $z/H = 1.49$. Data are from simulations S01 and S04 (cf. Table 6.3).
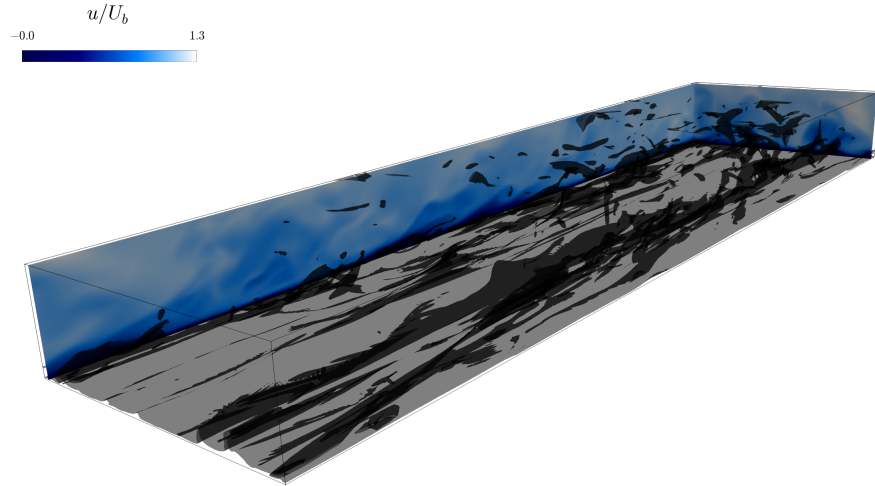

Figure 6.7: 3D snapshot of the concentration of bacteria (modelled with $Sc = 7$) at time $t/t_b = 59$ with iso-contour of the concentration $c_B = 0.02$. The simulation considered here is S05.

observed in the graphs that peaks of very high concentration are present in the high Schmidt number simulation, while completely absent when the diffusivity is high ($Sc = 7$ shown in the picture). This illustrates that globally averaged values can be much lower than the locally high (dangerous) concentration peaks occurring somewhere in the domain.

Figure 6.7 also shows that such occurrences of high pollutant concentration are affected by spatial heterogeneities of the turbulent flow. It was observed that after some period of time, the horizontally averaged pollutant concentration becomes higher nearer to the bottom, indicating an accumulation of the pollutant in that location. Evaluation of the instantaneous snapshots shows that very close to the bottom, regions with higher pollutant concentration correlate to regions where long elongated streaky structures are present. Scalo et al. [2012], who studied
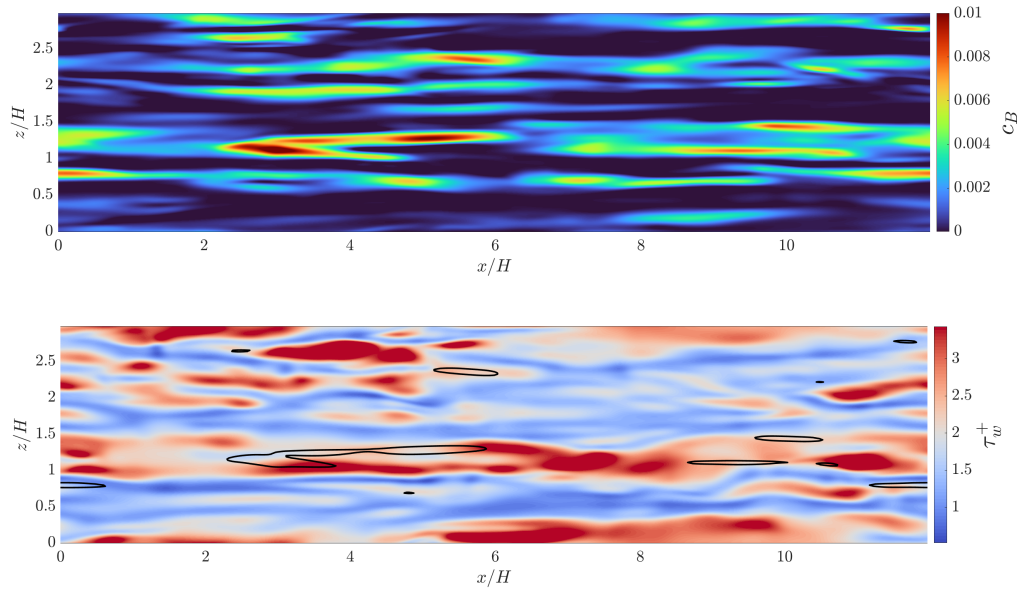
Figure 6.8: Comparison of two slices taken at $y/H = 0.004$ of concentration c_B (with $Sc = 7$) and the shear stress τ^+. The snapshots are taken at $t/t_b = 59$ of simulation S05. Black iso-lines represent $c_B = \langle c_B \rangle + \sigma_{c_B}$, where σ_{c_B} is the standard deviation of the instantaneous bacterial concentration in the plane considered.
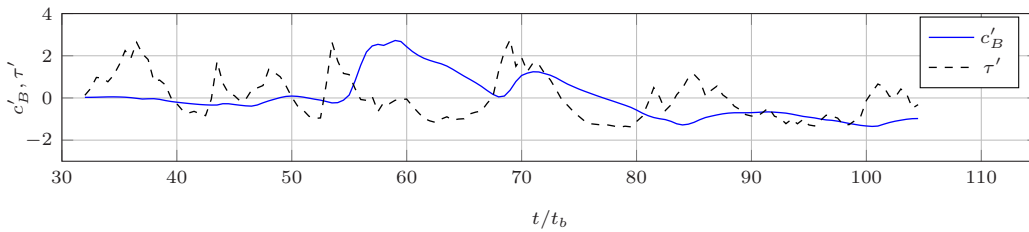
(a) $z/H = 0.75$
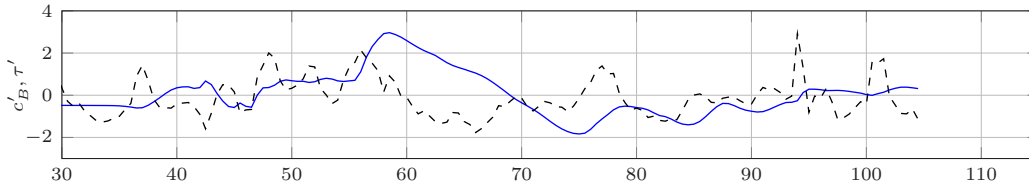
(b) $z/H = 1.7$

Figure 6.9: Fluctuations of concentration c_B and shear stress τ' in one point normalized with mean and standard deviation. Both the points are in $x/H = 2$ and $y/H = 0.004$. The points are taken from simulation S05.
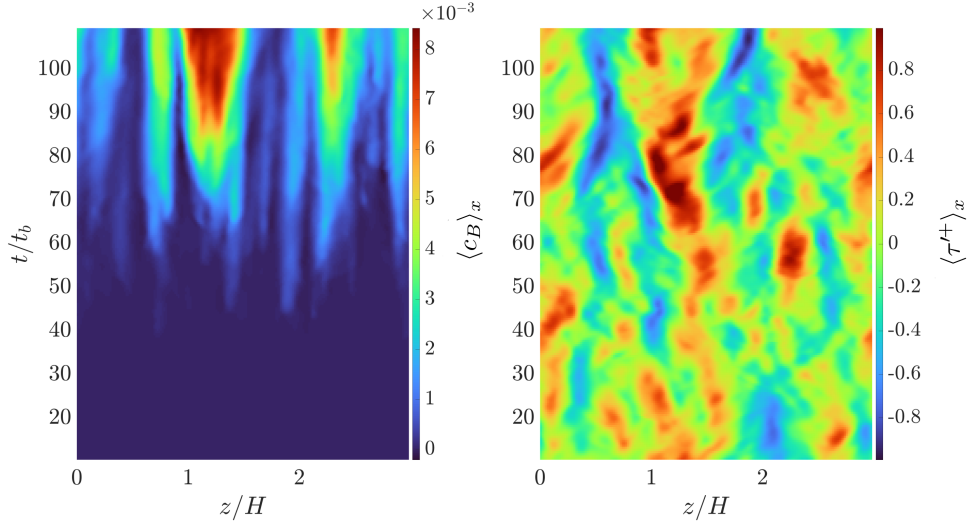
Figure 6.10: Evolution of the streamwise-averaged pollutant concentration (left pane) and streamwise-averaged wall shear stress fluctuation (right pane) near the bottom of the channel ($y/H = 0.0022$). The shown contours are from simulation S05.

mass transfer at the sediment-water interface, found a correlation between sweep (high shear stress near the wall) and high mass flux events at the bottom of the channel. Although, the boundary condition for the scalar at the bottom of the channel in the present simulations was different compared to the aforementioned research, a similar behavior between high shear stress events and peaks in bacterial concentration near the bottom of the channel was found, which can be seen in figure 6.8. The figure shows that peaks in bacterial concentration typically occur after high shear stress events. Figure 6.9 depicts the fluctuating signals of shear stress and c_B at two points very close to the wall. The plots show that a sharp increase in concentration comes after a peak in shear stress, confirming what assessed above. Moreover, the time lags between these two events seems to all have similar values. Figure 6.10 illustrates the effect of spatial heterogeneities of the turbulent flow on the transport of freely-suspended bacteria near the bottom. Shown here are the evolution in time of the streamwise-averaged concentration $\langle c_B \rangle_x$ and shear stress fluctuation $\langle \tau'^+ \rangle_x$ in the plane just above the wall. The figure confirms that events of local maxima in bacterial concentration occur after high shear stress events. In addition, it seems that once transported very close to the bottom of the channel, freely-suspended bacteria tend to accumulate forming streaks of high concentrations near the wall.

Time cross-correlation is defined as the correlation between two variables Ω_1 and Ω_2 in time:

$$R_{\Omega_1 \Omega_2}(y, \Delta t) = \frac{\langle \Omega_1(x,y,z,t) \Omega_2(x,y,z,t+\Delta t) \rangle}{|\langle \Omega_1(x,y,z,0) \Omega_2(x,y,z,0) \rangle|}. \tag{6.3}$$

A peak in time cross-correlation determines the time shift at which the correlation coefficient between the two quantities is maximum. The time lag is defined as the time difference between the highest positive peak position of the cross correlation and $t/t_b = 0$. The time cross-correlations between shear stress τ' and concentration c_B' shown in figure 6.11a allow to quantify the time lag between these two fluctuations for different Schmidt numbers. Figure 6.11b shows the dependence of the time lags in bulk time units on the Schmidt number (diffusivity). It can be seen that the time lag increases with increasing Schmidt number (lower diffusivity). This can be explained considering the slower response of low diffusivity scalars to flow modifications.

75

(a) Cross-correlation between concentration fluctuation $c_B{'}$ and shear stress fluctuation $\tau{'}$.

(b) Time lag as a function of Schmidt number.
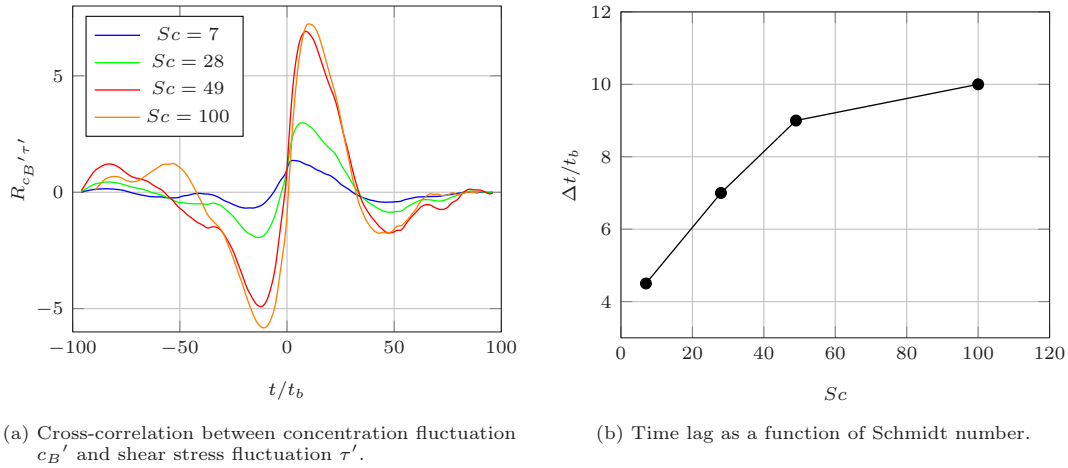
Figure 6.11: Cross-correlation and time lag between flow and bacterial motions for the simulations listed in table 6.3 (S01 to S04) close to the bottom of the channel ($y/H = 0.004$).

Even if the boundary condition at the wall and the numerical simulation employed were different in the present thesis and in Scalo et al. [2012], the results seem to confirm that high shear stress events predict peaks in mass flux/concentration and that a lower diffusivity increases the time lag between peaks in shear stress and in concentration.

7 Conclusion

The present thesis aimed to highlight the mechanisms behind interfacial mass transfer across the air-water interface of a turbulent open channel flow. The study was performed by means of several direct numerical simulations. Despite past research on this matter, most of the mechanisms playing a role in interfacial mass transfer are still unknown. Previous studies contradict each other to assess which eddy sizes are responsible for the phenomenon. The coefficients of the models described in chapter 2 were found to be dependent on flow variables that were different for every experiment. A deeper understanding of mass transfer across the air-water surface is necessary to develop more precise and universal models. In order to do so, fundamental research should reveal what is the interaction between flow and scalar structures.

The computational costs to perform reliable direct numerical simulations of low diffusivity scalars in turbulent open channel flow are very high. This limited the applicability of previous numerical studies conclusions to low Schmidt numbers and inadequate domain sizes. In the present thesis, the main drawbacks of previous numerical research were overcome through the use of an in-house code that employs a fifth-order WENO scheme for scalar convection and a fourth-order accurate central scheme for scalar diffusion. A dual mesh approach, in which the microscales typical of the flow field are resolved on a coarse mesh, while the smaller scales typical of low diffusivity scalars on a refined mesh, allowed to reach high Schmidt numbers (low diffusivities) in a very efficient manner.

In this chapter the main conclusions for the present thesis are drawn, followed by suggestions for future research.

7.1 Conclusions

Before performing interfacial mass transfer and pollutant transport simulations, the flow fields were developed and tested in order to assess their statistical stationarity. Three domain sizes were employed, $3H \times H \times 3H$, $12H \times H \times 3H$ and $24H \times H \times 6H$ with Reynolds numbers spanning from $Re_b = 2875$ to $Re_b = 12000$. The adequacy of the grid and domain sizes was confirmed through two-point correlation and energy spectra, respectively. Only the largest domain size chosen was found to be able to capture VLSM, showing de-correlation for the streamwise velocity component in x-direction at large separations. The data of all the simulations showed good agreement with the law of the wall, with constants for the log law equal to $k = 0.39$ and $B = 5$. The analysis of the velocity fluctuations underlined a correct trend for all the components and the expected scaling in wall units close the wall. The values of u_{rms} were found to be higher and v_{rms} and w_{rms} lower for the whole height of the channel, when a domain size smaller than $12H \times H \times 3H$ was employed. This is a known issue of small domain sizes, in which the lower energy fluxes hindered energy redistribution between the different directions. Higher values of u_{rms} for $y/H \geq 0.3$, typical indication of the presence of VLSM, were found for $Re_b \geq 6400$. The profiles of v_{rms} near the surface collapse on the same curve, when the vertical direction was scaled with the viscous scale l_v, in agreement with the findings of Bauer et al. [2020]. The values of the other two non-zero components at the surface were in good agreement with previous studies. The components of the turbulent kinetic energy budget showed weak

dependency on the Reynolds number in the inner layer, when normalized with viscous scales. The modification of the budget close to the surface was described and it underlined the effect that the boundary condition has on all the components. The presence of VLSM was proved through the analysis of pre-multiplied energy spectra and integral length scales. The former showed a double peak in streamwise and spanwise directions, which highlighted the presence of these motions for $Re_b \geq 6400$. The latter showed that L_{uu}^x reaches much higher values at $y/H \geq 0.3$ for $Re_b \geq 6400$. In the end, a schematic of the transport of small eddies from the bulk to the surface of the channel was drawn. It was found that high (low) velocity regions corresponds to downwelling (upwelling) motions. The high and low velocity regions organized in streaks that reach the whole domain length for $Re_b = 12000$. 3D snapshots showed that the rotation of large streamwise aligned vortical structures transport small eddies from the bulk of the channel to the surface. These small eddies near the surface either align or attache to the surface. The majority of the SPVS were found to lie in low velocity regions, where they enhance surface divergence at the surface, while the surface attached vortices lied mostly on high velocity regions.

Up to five scalars were added to the flow fields developed to study interfacial mass transfer in open channel flow. The diffusivities considered in the different simulations varied from $Sc = 4$ to 200. In order to resolve such low diffusivities, the grid resolution was chosen with the criteria described in Grötzbach [1983]. The diffusive boundary layer thickness was found to depend on $Re_b^{-0.67}$ and $Sc^{-0.5}$. Therefore, this quantity was employed to normalize the vertical direction in the mass transfer analysis. In this way, scalar statistics collapsed in one curve in the region close to the surface for all the different Re_b and Sc considered. The averaged turbulent mass fluxes normalized with j_s were found to collapse only for $(H-y)/\delta \leq 2$, while showing differences up to 15% already at $\delta/H = 10$. The mass transfer velocity was found to scale with $Re_b^{-0.33}$ and $Re_\tau^{-0.22}$, in agreement with previous experimental Moog and Jirka [1999] and numerical Nagaosa and Handler [2012] works. A turbulent Reynolds number was computed from the flow statistics, in order to assess the applicability of the two-regime model of Theofanous et al. [1976]. Since all the simulations were found to lie close or above the critical Reynolds number defined in the model $Re_T \simeq 500$, the data showed good agreement with the small eddy model, with a constant of proportionality close to the one used in Herlina and Wissink [2019]. Moreover, the SDM of McCready et al. [1986] could estimate with good precision the mass transfer velocity computed for each simulation. In opposition to previous studies of isotropic turbulence driven flow, the correlation between k_l and β slightly increased with the Reynolds number. This behavior was explained through conditional average that highlighted an increasing value for the correlation over high velocity regions for increasing Reynolds numbers. It was found that a rise in the turbulence level improves the mixing of small eddies close to the surface, which increases the impingement of upwelling motions in high velocity regions, enhancing the overall mass transfer. Large streamwise aligned vortical structures were found to be the mean for small eddies to reach the surface and actively improve the exchange of scalars at the surface. The agreement of K_L with the small eddy model should not mislead on thinking that only small structures enhance mass transfer. In fact, without the large streamwise-aligned vortices that actively transport turbulent eddies from the wall to the surface, mass transfer would be hindered.

To understand the main characteristics of water self-purification in open channel flow, a third group of simulations with domain sizes $3H \times H \times 3H$ and $12H \times H \times 3H$ and $Re_b = 2875, 3000$ were performed. In these simulations two scalars modelled the bacteria and the oxygen entering the flow from the surface of the channel. Different reaction terms in the advection-diffusion-

reaction equations link the two scalars. Particularly, in the present thesis, natural decay rate, UV-inactivation and higher metabolism due to the presence of oxygen were considered for the bacteria, while the oxygen consumption due to bacterial activity is the only decay rate that oxygen is subjected to. A first parameter sensitivity analysis underlined that UV-inactivation caused the strongest depletion of bacteria. The other terms were found to be negligible. Moreover, the effect of a different temperature between the pollutant and the ambient fluid was tested employing various Richardson numbers (buoyancy). This study underlined that the position of the pollutant causes different decay rates, with faster depletion when the temperature of the bacteria is higher than the temperature of the fluid. On the other hand, variations in the concentration of oxygen in the bulk showed negligible differences. In the parameter sensitivity analysis the Schmidt numbers used to model bacteria and oxygen were chosen to be 7 and 4, respectively. These low values (compared to the real values of bacteria and oxygen) are expected to highlight the effect of the different reaction terms, since the time scales of the scalars are closer to the flow ones. In the subsequent simulations that analyze the effect of spatial heterogeneities typical of turbulent channel flows, only UV-inactivation was considered. In these simulations, $Sc = 7, 28, 49$ and 100 were employed, in order to assess the role of diffusivity in mass transport. In this study, it was found that, even if the average values of concentration were low in the bulk of the channel, regions with dangerously high concentrations of pollutant could be found, especially when high Schmidt numbers were employed. 3D snapshots showed that bacteria tend to accumulate at the bottom of the channel, dragged down by the flow. It was found a link between peaks in shear stress at the wall, representing a symptom of downwelling motion, and concentration. The time scales between peaks in shear stress and concentration at the bottom were quantified through cross-correlation. The analysis underlined a larger delay between the peaks in the two quantities when higher Schmidt numbers were considered. Moreover, the pollutant at the bottom of the channel were found to be trapped in low speed regions and to accumulate in those positions for the rest of the simulation time.

7.2 Recommendations for future studies

Overall, the open questions listed in chapter 1 were answered successfully. I expect that some of the present findings can be readily applied to improve the existing mass transfer and pollutant transport models to approximate better the phenomena when an open channel flow is considered. However, some open questions remain for future studies.

The Reynolds and Schmidt numbers employed in the simulations are still far from the ones found in real rivers, where $Re_b = \mathcal{O}(10^6)$ and $Sc \simeq 500$ for oxygen and $Sc = \mathcal{O}(10^3)$ for bacteria. Future simulations should test the applicability of the interfacial mass transfer models to much higher values, in order to improve the approximation of real rivers. Moreover, the domain sizes employed demonstrated to be sufficient to capture the VLSM, but still inadequate to allow their meandering. In the present thesis, thanks to this limitation, a simple conditional average showed patterns for low mass transfer velocity coinciding with footprints of VLSM. Moreover, the pollutant transport simulations were performed only in the small and mid domain sizes, where VLSM are completely absent. Future numerical studies could check if the present results are still appreciable for larger domain sizes and could help on developing better experimental set ups.

The very general boundary conditions applied to the domain allowed the application of the present results to a variety of configurations, but at the same time excluded effects typical

of different geometries. For example, the absence of lateral walls that are always present in experiments and in real rivers in general hindered the study of the so-called secondary motions, which are similar in size to the VLSM, but are only due to the presence of the walls. Such motions are expected to enhance mass transfer, since they usually improve vertical mixing. Moreover, one of the main driving mechanisms in interfacial mass transfer is surface shear. Future simulations should test this feature to check if the mechanisms described in the present thesis are negligible compared to it. Waves were omitted in the present work, even though they are known to increase the mass transfer locally. In the future, with the increase of computational power, the application of the aforementioned conditions should become easier and easier. The availability of 3D snapshots and data from DNS could allow research to make a leap forward on understanding the mechanisms behind scalars transport in open channel flow.

Declaration of authorship

Declaration Michele Pinelli and Herlina Herlina carried out the simulations. Jan Wissink developed the code employed in all simulations. Michele Pinelli analyzed the data in constant cooperation with Herlina Herlina. The manuscript was prepared by Michele Pinelli and Herlina Herlina in consultation with Jan Wissink. Markus Uhlmann and Herlina Herlina devised and directed the project. All authors reviewed the complete article.

A Appendix

A.1 Danckwerts [1951]

Consider a liquid which is stirred at a steady rate, turbulent flow. The turbulent motion will keep replace the old surface areas (exposed for a limited period of time s), giving a uniform averaged rate of absorption at the surface. The chances of an element to be replaced by fresh fluid from the bulk is considered to be independent from its age: the fractional rate of replacement of the elements is equal to s.

Let us consider the elements having ages between θ and $\theta + d\theta$ to be $\phi(\theta)d\theta$. Since we are considering a steady state, we can assume that in a short time interval $d\theta$ the area entering the age group $\theta \div \theta + d\theta$ from the age group $\theta - d\theta \div \theta$ is $\phi(\theta)d\theta$), that is equal to the area in age group $\theta - d\theta \div \theta$ less the portion replaced by fresh surface in a time equal to $d\theta$:

$$\phi(\theta)d\theta = \phi(\theta - d\theta)d\theta(1 - sd\theta) \tag{A.1}$$

Therefore $\phi(\theta) = \phi\,\theta - \dfrac{d\phi}{d\theta}d\theta - s\phi$ with $\dfrac{d\phi}{d\theta} = -s\phi$. If we consider all the times, then we must have:

$$\int_0^\infty \phi\, d\theta = 1 \tag{A.2}$$

and then:

$$\phi = s\, e^{-s\,\theta}. \tag{A.3}$$

Considering the rate of absorption into those elements of surface having age θ and combined area $s\, e^{-s\,\theta}d\theta$:

$$\psi = (c_s - c_b)s\, e^{-s\,\theta}\sqrt{\frac{D}{\pi\theta}}d\theta, \tag{A.4}$$

we obtain the mean rate of absorption per unit area of turbulent surface:

$$R = (c_s - c_b)\sqrt{D}\int_0^\infty \frac{s\, e^{-s\,\theta}}{\sqrt{\pi\theta}}d\theta = (c_s - c_b)\sqrt{D\,s}. \tag{A.5}$$

It is easily found that the mass transfer is $\sqrt{D\,s}$.

A.2 Demonstration of $K_L \propto \sqrt{D}$

Considering a fluid particle close to the surface, which is dragged down to the bulk of the flow, the mass fluxes will be constant for the different flow regions, due to the steady state hypothesis, such that:

$$(\overline{\langle c \rangle} - c_s)\sqrt{D\,s} = (c_s - c_b)K_E = (\overline{\langle c \rangle} - \overline{\langle c_b \rangle})K_L \tag{A.6}$$

and then:

$$\frac{1}{K_L} = \frac{1}{K_E} + \frac{1}{\sqrt{D\,s}} \tag{A.7}$$

where K_E is the average mass transfer velocity due to eddy diffusion. Since s and K_E are only functions of the physical properties and flow conditions, $1/K_L$ must vary linearly with $1/\sqrt{D}$.

A.3 Determination of A in Fortescue and Pearson [1967]

Given the velocity defined in Equation 2.45, the kinetic energy associated to the roll cell will be:

$$K = \frac{1}{2\lambda^2} \int_0^\lambda \int_0^\lambda u^2 + v^2 + w^2 \, dx \, dy = \frac{1}{4}A^2. \tag{A.8}$$

Considering also that:

$$\lambda = \int_0^\infty \frac{1}{u_r^2(\mathbf{x})} \overline{u_r(\mathbf{x})u_r(\mathbf{x}+\mathbf{r})} dr, \tag{A.9}$$

they defined:

$$A = 2\sqrt{\frac{1}{2}u^2 + \frac{1}{2}v^2 + \frac{1}{2}w^2} \tag{A.10}$$

as an upper bound approximation.

A.4 Development of the surface divergence model

Considering the concentration variation and the non-linear terms in the flow direction negligible and $\frac{\partial^2 c}{\partial z^2} \ll \frac{\partial^2 c}{\partial y^2}$ (the concentration boundary layer is very thin), the authors obtained the following linear equation:

$$\frac{\partial c'}{\partial t} + \beta \, y \frac{\partial \overline{\langle c \rangle}}{\partial y} = \frac{1}{Sc} \frac{\partial^2 c'}{\partial y^2}. \tag{A.11}$$

McCready et al. [1986] found the solution of equation A.11 with an order-of magnitude analysis for high:

$$vc' \sim \frac{\beta^2 \delta}{\omega}, \tag{A.12}$$

and low frequency velocity fluctuations:

$$vc' \sim \beta^2 \delta^3 Sc. \tag{A.13}$$

In these equations, δ is the diffusive boundary layer thickness, defined as the position at which the concentration fluctuation c' reach its maximum. Merging the two solutions, vc' reads:

$$vc' = \int_0^{\omega_c} \delta^3 Sc \, W_\beta(\omega) d\omega + \int_{\omega_c}^\infty \delta \frac{W_\beta(\omega)}{\omega} d\omega, \tag{A.14}$$

where $\omega_c = 1/(\delta^2 Sc)$ and W_β is the spectral function for β:

$$\overline{\beta^2} = \int_0^\infty W_\beta(\omega) d\omega. \tag{A.15}$$

At the limit of the concentration boundary layer ($y = \delta$) the turbulent transport is approximately equal to the molecular transport:

$$vc' \sim \frac{1}{Sc} \frac{d\langle c \rangle}{dy}. \tag{A.16}$$

Imposing the spectral function to be:

$$W_\beta(\omega) = \frac{W_\beta(0)}{1 + \left(\dfrac{\omega\sigma}{\omega_m}\right)^2}, \tag{A.17}$$

where:

$$\omega_m = \frac{\int_0^\infty \omega W_\beta(\omega)d\omega}{\int_0^\infty W_\beta(\omega)d\omega} \tag{A.18}$$

$$\sigma = \omega_m \pi \frac{W_\beta(0)}{\beta^2}. \tag{A.19}$$

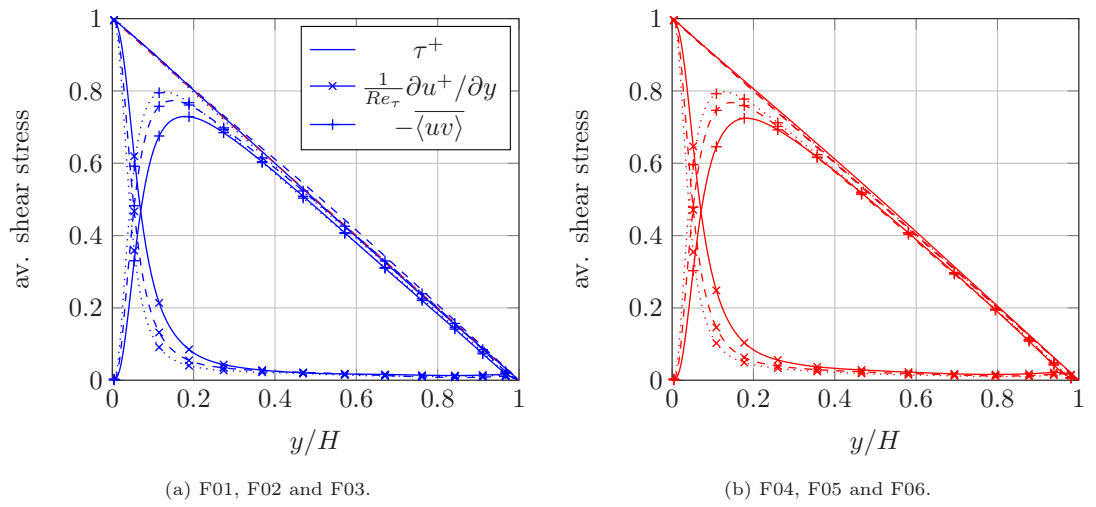## A.5 Shear-stress

(a) F01, F02 and F03.

(b) F04, F05 and F06.

Figure A.1: Total, laminar and turbulent shear-stress for simulations for all the simulations performed.

A.6 Integral length scales

(a) F01.

(b) F02.

(c) F03.
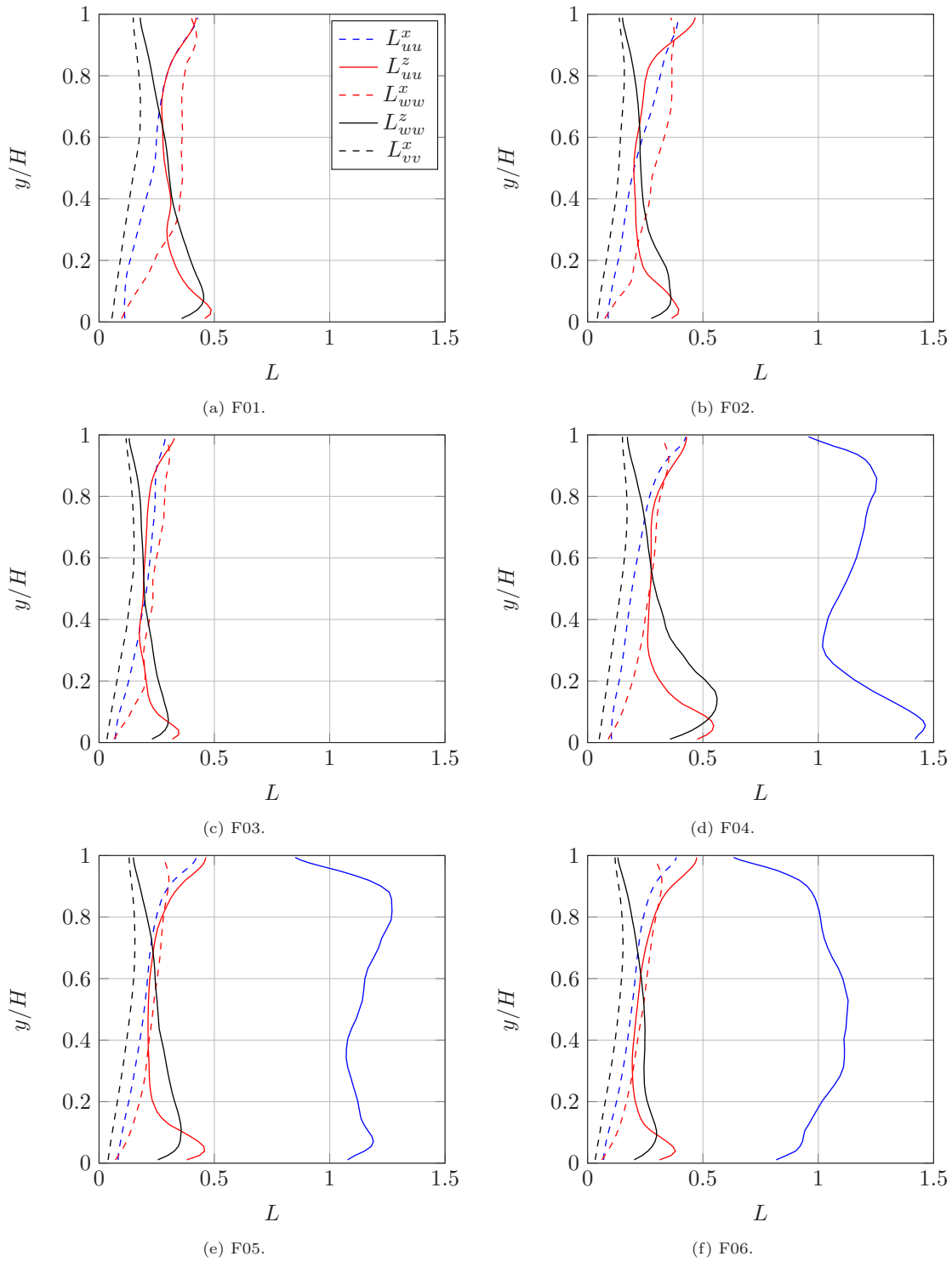
(d) F04.

(e) F05.

(f) F06.

Figure A.2: Integral length scales.

Bibliography

H. Abe, R. A. Antonia, and S. Toh. Large-scale structures in a turbulent channel flow with a minimal streamwise flow unit. *Journal of Fluid Mechanics*, 850(2):733–768, 2018.

J. C. Del Álamo, J. Jiménez, P. Zandonade, and R. D. Moser. Scaling of the energy spectra of turbulent channels. *Journal of Fluid Mechanics*, 500:135–144, 2004.

M. A. Atmane and J. George. Gas transfer across a zero-shear surface: a local approach. *Washington DC American Geophysical Union Geophysical Monograph Series*, 127:255–259, 2002.

B. J. Balakumar and R. J. Adrian. Large- and very-large-scale motions in channel and boundary-layer flows. *Philosophical Transactions of the Royal Society A: Mathematical, Physical and Engineering Sciences*, 365(1852):665–681, 2007.

S. Banerjee, D. Scott, and E. Rhodes. Mass transfer to falling wavy liquid films in turbulent flows. *Industrial Engineering Chemicals Fundamentals*, 7:22–27, 1968.

C. Bauer, Y. Sakai, and M. Uhlmann. DNS of plane open channel flow: Scaling near the free-slip boundary and evidence of very-large-scale motions. *(submitted)*, 2020.

V. Borue, S. A. Orszag, and I. Staroselsky. Interaction of surface waves with turbulence: direct numerical simulations of turbulent open-channel flow. *Journal of Fluid Mechanics*, 286:1–23, 1995.

I. Calmet and J. Magnaudet. Statistical structure of high-Reynolds-number turbulence close to the free surface of an open-channel flow. *Journal of Fluid Mechanics*, 474:355–378, 2003.

J. J. Cole and N. F. Caraco. Atmospheric exchange of carbon dioxide in a low wind oligotrophic lake measured by the addition of SF6. *Limnology and Oceanography*, 43:647–656, 1998.

G. T. Csanady. Mean circulation in shallow seas. *Journal of Geophysical Research*, 81(30):5389–5399, 1976.

P. V. Danckwerts. Significance of liquid-film coefficients in gas absorption. *Industrial and Engineering Chemistry*, 43:1460–1467, 1951.

J. C. Del Álamo and J. Jiménez. Spectra of the very large anisotropic scales in turbulent channels. *Physics of Fluids*, 15(6):L41–L44, 2003.

T. DeVries, M. Holzer, and F. Primeau. Recent increase in oceanic carbon uptake driven by weaker upper-ocean overturning. *Nature*, 542:215–218, 2017.

J. W. Elder. The dispersion of marked fluid in turbulent shear flow. *Journal of Fluid Mechanics*, 5(4):544–560, 1959.

D. Feldmann, C. Bauer, and C. Wagner. Computational domain length and Reynolds number effects on large-coherent motions in turbulent pipe flow. *Journal of Turbulence*, 19:274–295, 2018.

G. E. Fortescue and J. R. A. Pearson. On gas absorption into a turbulent liquid. *Chemical Engineering Science*, 22:1163–1176, 1967.

T. Garcia-Armisen and P. Servais. Partitioning and fate of particle-associated E. Coli in river waters. *Water Environ. Res.*, 81:21–28, 2009.

G. Grötzbach. Spatial resolution requirements for direct numerical simulation of the Rayleigh-Benard convection. *Journal of Computational Physics*, 49:241–264, 1983.

R. A. Handler, J. R. Saylor, R. I. Leighton, and A. L. Rovelstad. Transport of a passive scalar at a shear-free boundary in fully turbulent open channel flow. *Physics of Fluids*, 11(9): 2607–2625, 1999.

H. Herlina and G. H. Jirka. Experiments on gas transfer at air-water interface induced by oscillating grid turbulence. *Journal of Fluid Mechanics*, 594:183–208, 2008.

H. Herlina and J. G. Wissink. Direct numerical simulation of turbulent scalar transport across a flat surface. *Journal of Fluid Mechanics*, 744:217–249, 2014.

H. Herlina and J. G. Wissink. Simulation of air-water interfacial mass transfer driven by high-intensity isotropic turbulence. *Journal of Fluid Mechanics*, 860:419–440, 2019.

R. Higbie. The rate of absorption of a pure gas into a still liquid during short periods of exposure. *Transactions of the AIChE Journal*, 31:365–389, 1935.

S. Hoyas and J. Jiménez. Scaling of the velocity fluctuations in turbulent channels up to $Re_\tau = 2003$. *Physics of Fluids*, 18(1):011702, 2006.

J. Hunt, A. Wray, and P Moin. Eddies, streams, and convergence zones in turbulent flows. *Studying Turbulence Using Numerical Simulation Databases*, -1:193–208, 11 1988.

N. Hutchins and I. Marusic. Evidence of very long meandering features in the logarithmic region of turbulent boundary layers. *Journal of Fluid Mechanics*, 579:1, 2007.

Y. Hwang and C. Cossu. Self-sustained process at large scales in turbulent channel flow. *Physical Reviews Letters*, 105:044505, 2010.

B. Jähne. *Zum Parametrisierung des Gasaustausches mit Hilfe von Laborexperimenten*. PhD thesis, Ruprecht-Karl-Universität Heidelberg, 1980.

B. Jähne and H. Haußecker. Air-water gas exchange. *Annual Review of Fluid Mechanics*, 30: 443–468, 1998.

B. Jähne, W. Huber, A. Dutzi, T. Wais, and J. Ilmberger. *Wind/Wave-Tunnel Experiment on the Schmidt Number — and Wave Field Dependence of Air/Water Gas Exchange*, pages 303–309. Springer Netherlands, Dordrecht, 1984. ISBN 978-94-017-1660-4. doi: 10.1007/978-94-017-1660-4_28.

J. G. Janzen, H. Herlina, H. Jirka, H. E. Schulz, and J. S. Gulliver. Estimation of mass transfer velocity based on measured turbulence parameters. *AIChE Journal*, 56:2005–2017, 2010.

J. Jiménez. Cascades in wall-bounded turbulence. *Annual Review of Fluid Mechanics*, 44(1): 27–45, 2012.

A. Kermani, H. R. Khakpour, L. Shen, and T. Igusa. Statistics of surface renewal of passive scalar in free-surface turbulence. *Journal of Fluid Mechanics*, 19:159–174, 2011.

H. R. Khakpour, L. Shen, and D. K. P. Yue. Transport of passive scalar in turbulent shear flow under a clean or surfactant-contaminated free surface. *Journal of Fluid Mechanics*, 670: 527–557, 2011.

J. Kim, P. Moin, and R. D. Moser. Turbulence statistics in fully developed channel flow at low Reynolds number. *Journal of Fluid Mechanics*, 177:133–166, 1987.

K. C. Kim and R. J. Adrian. Very large-scale motion in the outer layer. *Physics of Fluids*, 11 (2):417–422, 1999.

A. N. Kolmogorov. The local structure of turbulence in incompressible viscous fluid for very large Reynolds numbers. *Doklady Akademiia Nauk SSSR*, 30:301–305, 1941.

S. Komori, H. Ueda, F. Ogino, and T. Mizushina. Turbulence structure and transport mechanism at the free surface of an open channel flow. *International Journal of Heat and Mass Transfer*, 25:513–521, 1982.

B. Kubrak, H. Herlina, F. Greve, and J. G. Wissink. Low-diffusivity scalar transport using a WENO scheme and dual meshing. *Journal of Computational Physics*, 240:158–173, 2013.

J. C. Lamont and D. S. Scott. An eddy cell model of mass transfer into surface of a turbulent liquid. *AIChE Journal*, 16:513–519, 1970.

Y. L. Lau and B. G. Krishnappan. Transverse dispersion in rectangular channels. *Journal of the Hydraulics Division*, 105(4):426–427, 1977.

J. J. Ledwell and G. H. Jirka. *The Variation of the Gas Transfer Coefficient with Molecular Diffusity*, pages 293–302. Springer Netherlands, 1984.

M. Lee and R. D. Moser. Direct numerical simulation of turbulent channel flow up to $Re_\tau \approx$ 5200. *Journal of Fluid Mechanics*, 774:395–415, 2015.

W. K. Lewis and W. G. Whitman. Principles of gas absorption. *68th Meeting of the American Chemical Society*, 16:1215–1220, 1924.

P. S. Liss. Processes of gas exchange across an air-water interface. *Deep Sea Research and Oceanographic Abstracts*, 20(3):221–238, 1973.

X. D. Liu, S. Osher, and T. Chan. Weighted essentially non-oscillatory schemes. *Journal of Computational Physics*, 115:200–212, 1994.

A. Lozano-Durán and J. Jiménez. Effect of the computational domain on direct simulations of turbulent channels up to $Re_\tau = 4200$. *Physics of Fluids*, 26:011702, 2014.

J. Magnaudet and I. Calmet. Turbulent mass transfer through a flat shear-free surface. *Journal of Fluid Mechanics*, 553:155–185, 2006.

M. J. McCready, E. Vassiliadou, and T. J. Hanratty. Computer simulation of turbulent mass transfer at a mobile interfac. *AIChE Journal*, 32:1108–1115, 1986.

A. C. Miller and E. V. Richardson. Diffusion and dispersion in open channel flow. *Journal of Hydraulic Division*, 100(hy1):159–172, 19.

D. B. Moog and G. H. Jirka. Air-water gas transfer in uniform channel flow. *Journal of Hydraulic Engineering*, 125(1):3–10, 1999.

R. D. Moser, J. Kim, and N. N. Mansour. Direct numerical simulation of turbulent channel flow up to $Re_\tau = 590$. *Physics of Fluids*, 11(4):943–945, 1999.

R. Nagaosa and R. A. Handler. Statistical analysis of coherent vortices near a free surface in a fully developed turbulence. *Physics of Fluids*, 15:375–394, 2003.

R. Nagaosa and R. A. Handler. Characteristic time scales for predicting the scalar flux at a free surface in turbulent open-channel flows. *AIChE journal*, 58:3867–3877, 2012.

I. Nezu and W. Rodi. Open channel flow measurements with a laser doppler anemometer. *Journal of Hydraulic Engineering*, 112:335–355, 1986.

Y. Pan and S. Banerjee. A numerical study of free-surface turbulence in channel flow. *Physics of Fluids*, 7:1649–1664, 1995.

A. E. Perry, S. Henbest, and M. S. Chong. A theoretical and experimental study of wall turbulence. *Journal of Fluid Mechanics*, 165:163–199, 1986.

C. Peruzzi, D. Poggi, L. Ridolfi, and C. Manes. On the scaling of large-scale structures in smooth-bed turbulent open-channel flows. *Journal of Fluid Mechanics*, 889:A1, 2020.

M. Pinelli, H. Herlina, J. G. Wissink, and M. Uhlmann. Interfacial mass transfer in turbulent open channel flow. *Journal of Fluid Mechanics*, 933:A49, 2022.

S. Pirozzoli, M. Bernardini, and P. Orlandi. Passive scalars in turbulent channel flow at high Reynolds number. *Journal of Fluid Mechanics*, 788:614–639, 2016.

S. B. Pope. *Turbulent flows.* Springer, 2000.

M. Rashidi and S. Banerjee. Streak characteristics and behavior near wall and interface in open channel flows. *Journal of Fluids Engineering-transactions of The Asme*, 112:164–170, 1990.

M. Rashidi, G. Hetsroni, and S. Banerjee. Mechanisms of heat and mass transport at gas-liquid interfaces. *International Journal of Heat and Mass Transfer*, 34(7):1799–1810, 1991.

L. F. Richardson. Weather prediction by numerical process. *Quarterly Journal of the Royal Meteorological Society*, 48(203):282–284, 1922.

K. Richter and Jähne B. A laboratory study of the Schmidt number dependency of air-water gas transfer. In *Gas Transfer at Water Surfaces.* Zenodo, 2011.

P. Roslev, L. A. Bjergbæk, and M. Hesselsoe. Effect of oxygen on survival of fecal pollution indicators in drinking water. *Journal of Applied Microbiology*, 96(5):938–945, 2004.

M. Sanjou, I. Nezu, and T. Okamoto. Surface velocity divergence model of air/water interfacial gas transfer in open-channel flows. *Physics of Fluids*, 29(4):045107, 2017.

C. Scalo, U. Piomelli, and L. Boegman. High-Schmidt-number mass transport mechanisms from a turbulent flow to absorbing sediments. *Physics of Fluids*, 24:085103, 2012.

C. Schultz-Fademrecht, M. Wichern, and H. Horn. The impact of sunlight on inactivation of indicator microorganisms both in river water and benthic biofilms. *Water Research*, 42: 4771–4779, 2008.

L. W. Sinton, C. H. Hall, P. A. Lynch, and R. J. Davies-Colley. Sunlight inactivation of fecal indicator bacteria and bacteriophages from waste stabilization pond effluent in fresh and saline waters. *Appl. Environ. Microbiol.*, 68:1122–1131, 2002.

A. Tamburrino and J. S. Gulliver. Free-surface turbulence and mass transfer in a channel flow. *AIChE Journal*, 48(12):2732–2743, 2002.

G. I. Taylor. Diffusion by continuous movements. *Proceedings of the London Mathematical Society*, s2-20(1):196–212, 1922.

G. Tchobanoglous, F. L. Burton, and H. D. Stensel. *Wastewater Engineering: Treatment and Reuse.* Metcalf and Eddy, Inc., McGraw-Hill Education, 2003.

T. G. Theofanous, R. N. Houze, and L. K. Brumfield. Turbulent mass transfer at free, gas-liquid interfaces, with applications to open-channel, bubble and jet flows. *Intl Journal of Heat and Mass Transfer*, 19:613–624, 1976.

R. V. Thomann and J.A. Mueller. *Principles of surface water quality modeling and control.* Harper and Row, 1987.

D. E. Tourney and S. Banerjee. Air-water gas transfer and near-surface motions. *Journal of Fluid Mechanics*, 733:588–622, 2013.

J. Tschiersch and B. Jähne. Gas exchange through a rough water surface in a circular wind-tunnel; wave characteristics under limited and unlimited fetch. *Berichte aus dem Sonderforschungsbereich 94 Meeresforschung - Symposium on Capillary Waves and Gas Exchange, Trier July 2–6, 1979*, 17:63–70, 1980.

D. E. Turney and S. Banerjee. Air-water gas transfer and near-surface motions. *Journal of Fluid Mechanics*, 733:588–624, 2013.

T. von Karman. Mechanische änlichkeit und turbulenz. *Nachricthen von der Gesellschaft der Wissenschaften zu Göttingen, Mathematisch-Physikalische Klasse*, 58, 1930.

E. Walters. Fate and transport of fecal indicator bacteria in flume systems mimicking an oligotrophic river. *Ph.D. thesis, TU München*, 2013.

G. Wang and D. H. Richter. Two mechanisms of modulation of very-large-scale motions by inertial particles in open channel flow. *Journal of Fluid Mechanics*, 868:538–559, 2019.

G. Wang, H. J. Park, and D. H. Richter. Effect of computational domain size on inertial particle one-point statistics in open channel flow. *International Journal of Multiphase Flow*, 125:103195, 2020.

R. Wanninkhof, W. E. Asher, D. T. Ho, C. Sweeney, and W. R. McGillis. Advances in quantifying air-sea gas exchange and environmental forcing. *Annual Review of Marine Science*, 1: 213–244, 2009.

J. G. Wissink. On unconditional conservation of kinetic energy by finite-difference discretizations of the linear and non-linear convection equation. *Computers & Fluids*, 33(2):315–343, 2004.

J. G. Wissink and H. Herlina. Direct numerical simulation of gas transfer across the air-water interface driven by buoyant convection. *Journal of Fluid Mechanics*, 787:508–540, 2016.

J. G. Wissink, H. Herlina, Y. Akar, and M. Uhlmann. Effect of surface contamination on interfacial mass transfer rate. *Journal of Fluid Mechanics*, 830:5–34, 2017.

Q. Zhong, Q. Chen, H. Wang, D. Li, and X. Wang. Statistical analysis of turbulent super-streamwise vortices based on observations of streaky structures near the surface in the smooth open channel flow. *Water Resources Research*, 52:3563–3578, 2016.